University of Bergen
Department of Physics

Master thesis for Ocean technology Marine Measurement systems and Acoustics

Defect detection and acoustic penetration of grout in offshore structures

Mats Johan Fjellheim

August, 2023

Abstract

Recently, integrity inspections of grouted connections in offshore wind turbines have become more important due to the increased signs of wear, with multiple reports of sliding damage in the grouted connection [1, 2]. This study delves into an ultrasonic non-destructive testing (NDT) approach for evaluating grout penetration and identifying defects within the grout and grouted connection. A pulse with a frequency range of 60 to 140 kHz was applied to the grout with and without defects, with the reflection and reverberation studied to determine the detectability and penetration of the grout. The same frequency range is employed for numerical simulations of grout, grout with a steel plate in front and grouted connections, with and without defects.

The results reveal good penetration of the grout with a visible pulse from the back interface of the grout both in the experiments and simulations. Changes in the frequency spectrum for simulations of grout with defects over half a wavelength were detected, with notable differences between the simulations where the grout had defects and those without defects. However, the experimental results were inconclusive, with the differences between the grout samples with the same defects or lack thereof being as large as those between the samples with or without defects.

The simulations of the grout with a steel plate covering and grouted connection showed minimal penetration of the grout with no discernible pulse from the back interface of the structure. The grout with a steel plate covering showed minimal differences between the simulations with or without defects. However, simulations of the grouted connection show discernible differences for the largest defect, indicating some level of grout penetration.

Acknowledgment

With these words, I aim to convey my profound appreciation to all those who have played a role in the successful completion of my Master's thesis in Ocean Technology. First and foremost, I wish to express my gratitude to my supervisor, Prof. Per Lunde, from the Department of Physics and Technology, as well as my co-supervisors Jan Kocbach from NORCE, Sverre Finstad from TSC Subsea, and my former co-supervisor, Renate Grindheim from TSC Subsea. Your decision to accept me as a master's student and your consistent guidance throughout this journey are deeply appreciated.

I would like to extend my heartfelt thanks to Henrik Duerud, whose contributions were vital in establishing the measurement system and enhancing my comprehension of it.

Acknowledgments are also due to my fellow classmates for their companionship and the cherished memories we've created together. Your inspiration, enjoyable company, and invaluable fount of knowledge and discussions over the past five years have been invaluable.

Lastly, my family and friends merit my utmost gratitude for being my pillars of strength throughout this entire endeavor. Your unwavering support, motivation, and care have been a cornerstone in my journey. I would like to offer a special note of thanks to my grandparents for their assistance in completing my master's journey as I transitioned to Oslo and embarked on my career path.

Mats Johan Fjellheim, Oslo, 31.August.2023

Contents

Chapter 1

Introduction

1.1 Background and motivation

Grouted connections have been extensively employed in diverse offshore structural applications, including the gas and oil industry, for the last decades [3]. More recently, their applications have been extended to the offshore wind industry [3]. These connections involve joining structural elements through a cementitious grout material, facilitating load transfer and maintaining structural continuity. The plain-pipe grouted connection studied in this report is a sandwich-like structure of steel–grout–steel, which supports the transition piece, as shown in Fig.1.1. The presence of defects in the grout, such as voids, cracks and debonding, can severely undermine the structural integrity and performance of the entire system [4]. Therefore, addressing these potential issues is critical to achieving longevity and reliability of structures utilising grouted connections [4, 1, 5].

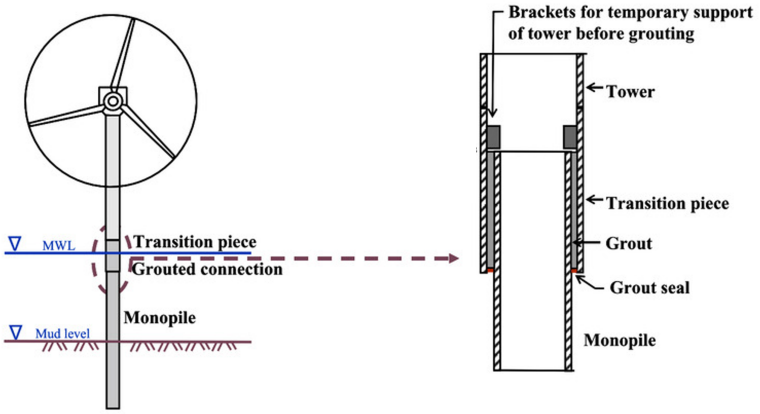

Figure 1.1: Depiction of grouted connection in a monopile wind turbine. [6]

The design of a plain-pipe grouted connection on an offshore jacket design before 2013 was based only on transferring axial and torsional loads from the jacket to the pile, according to standards such as NORSOK N004 [7] and DNV-OS-J101 [8]. As stated in Klose [9] and Tziavos [1], since 2009, sliding damage has been reported at several offshore wind farms with plain cylindrical grouted joints. As a result, existing guidelines, such as DNV-OS-J101 [8] and NORSOK N004 [7], have been reviewed, and design approaches and calculation tools have been modified.

The Norsok standard [7] requires grouted connections to be inspected yearly. The uncertainties introduced by the new requirements, re-calculations and slippage in the existing wind turbines increase the focus on the available methods for inspecting and monitoring the condition of the grouted connection and their ability to detect defects and predict failure.

Visual inspection is the most common method for inspecting grouted connections, performed by divers or remotely operated vehicles [4]. However, visual inspections are limited in that the inspections can only be performed on the exposed grout at the top or bottom of the grouted connection, as shown in Fig. 1.1. By the time the defects are visible, the grouted connection is thoroughly degraded and requires extensive maintenance activities [1]. As discussed by Tziavos [1], the lack of early warning results in operational solutions on a case-by-case basis. Garcia [10] and Shafiee [11] explained that the accessibility to offshore wind turbines is affected by weather conditions, and maintenance tasks require complete generator shutdowns, leading to significant expenditures.

In other research, Tziavos [1] and Martinez [2] stated that minimising unnecessary maintenance expenditure to reduce high costs and enhancing the reliability of offshore wind turbine substructures are some major challenges for the offshore wind sector. To address these challenges, a transition to condition- and predictive-based maintenance is necessary, compared to corrective and preventive maintenance, which are commonly employed [1].

Condition-based maintenance is based on the detection, identification and monitoring of damage evolution with time [2]. However, the lack of expert knowledge and experience on the long-term behaviour of grouts makes effective monitoring tools for grouted connections essential [1]. Furthermore, the integrity issues relevant for determining the condition of the grouted connection make it desirable with an inspection method in which the grout can be inspected outside and detect initial degradation [4].

In [4, 1, 10, 9], multiple non-destructive testing (NTD) inspection techniques in development are discussed, but a reliable, widespread, comprehensive and practical inspection technique is yet to be available. Tuset [4] suggested that the inspection method is instrumental in determining the actual state of the grouted connection. Furthermore, Iliopoulos [12] explored multiple NDT techniques where the attenuation of ultrasound matched the strength of the grout very well. Similarly, Brett [13] found promising results using an ultrasonic-based inspection method.

TSC Subsea is working on a comprehensive NDT method for plain-pipe grouted connections [14]. Their approach is based on acoustics resonance technology (ART) deployed in their ARTIMIS product line, developed for inspecting the internal condition of pipelines and risers [14]. ART has shown great potential in detecting the state of the grouted connection [14]. However, because of the frequency range from the mid 100s kHz, the attenuation is profound in the grout, and insufficient penetration of the grout occurs [14]. As a result, the grout's front layer is inspected, but not the deeper layers [14]. TSC subsea's ART method is more effective than the visual inspection method, but it still requires improvement [14].

1.2 Previous work

In 1941, working independently, Sproule [15] and Firestone [16] pioneered the technology to detect flaws in metal for industrial purposes, but because of the second world war, their results were not published until 1946 [17]. The release of Sproule's and Firestone's findings did not only advance the field of Ultrasonic NDT but also closely related fields such as medical ultrasonic imaging. [17, 15].

The first commercial instrument for determining the thickness of metal was patented by Rassweiler and Erwin of General Motors in 1947 [18]. The principles of operation for the instrument called the *Sonigage* was published by Erwin in 1945 [19]. The *Sonigage* differed itself from other ultrasonic instruments by not measuring the time intervals directly, but rather the resonant frequency in the plates [19].

The first ultrasonic instruments that measured the thickness of metal with frequency response often used single-frequency excitation, in the form of a tone burst [20]. This technique is relatively time consuming since, in order to define the resonant frequencies of the test structure, it is necessary to vary the frequency across the frequency range of interest, which, particularly if fine frequency resolution is required, can be a lengthy process [20].

By the 1980s the focus of industrial ultrasonic thickness measurements shifted to pulse excitation followed by a high speed analog-to-digital conversion followed by a digital Fourier analysis, which produced the complete spectrum [20]. This allowed the complete spectrum to be obtained rapidly from the response of the system to a single pulse [20]. This technique was used in the 1980s by de Billy [21] and Numrich [22], and is the foundation for the measurement system used in this study.

Over the last few decades, ultrasonic pulse-echo has established itself as a common non-destructive inspection method [4, 23]. As discussed in [23], the advancements in signal processing and transducer technology made inspecting multilayered structures possible.

1.3 Objective

This master's thesis aims to investigate if acoustic signals in a lower frequency range can provide information on deeper defects in the grout to lay the foundation for further development of the ART inspection method utilised by TSC Subsea. To accomplish the objective, this report investigates the frequency response of the reverberation and reflected signal from the grout and grouted connection for an incident wave with a frequency range from the late 10s kHz to the early 100s kHz. This approach is anticipated to yield deeper penetration and reduced attenuation within the grout.

This study conducts both simulated and experimental investigations of the acoustic response within the frequency range. The results are subsequently compared with the aim of developing a simulation model that accurately corresponds to the experimental outcomes. The successful alignment of the simulation and experimental results will provide greater confidence in the accuracy of the simulation model. This, in turn, will enable effective further study with modifications to the frequency range and other parameters.

1.4 Thesis outline

This thesis comprises six chapters and several appendices. The first chapter presents the project's motivation and objective. Chapter 2 is devoted to the theoretical foundations of the thesis, with particular emphasis on the reflection coefficient, material characteristics and transducer characteristics. The experimental setup and measurement methods employed are described in Chapter 3, along with the frequency range, signal processing and specifications of the transducer. Chapter 4 details the finite element simulation setup, including the simulation tool, structures, meshing and time resolution. Finally, Chapter 5 offers the results with a comprehensive discussion of the research findings, while Chapter 6 draws conclusions and provides recommendations for further research. The appendices contain MATLAB scripts, detailed calculations and various figures.

Chapter 2

Theory

This chapter presents the theoretical foundation required to conduct the experiments and simulations of this study. Section 2.1 delves into the fundamental theory of acoustic wave propagation, encompassing aspects like sound velocity and material density. In Section 2.2, the reflection coefficients for fluid–fluid and fluid–solid interfaces are presented. Section 2.2.1 presents the reflection coefficient for fluid–fluid interfaces for multilayered structures, and Subsection 2.2.2 explains the reflection coefficient for a fluid–solid interface, which modifies the solid–solid reflection coefficient discussed in [24].

Section 2.3, presents the definitions of the near and far fields, with the acoustic pressure from a baffled circular plane piston is covered in Section 2.4. The characteristics of transducers, including source- and receiver sensitivity and electrical impedance, are addressed in Section 2.5. Furthermore, Section 2.6 explains the finite element method, highlighting the distinction between time-implicit and time-explicit approaches.

The conception of a defect is outlined in Section 2.7, while the theoretical resonant frequencies and attenuation are discussed in Sections 2.8 and 2.9, respectively. Finally, Section 2.10 presents the theoretical framework for the various signal processing tools employed throughout this study.

2.1 Acoustic wave propagation

Acoustic wave propagation refers to the transmission of mechanical energy through a medium via elastic waves [25]. For fluids, mechanical energy is transmitted in the form of compres-

sional waves, and for solids, the transmission is in compressional- and shear waves [25]. In this study, acoustic waves are utilised to investigate the presence of defects in grout and grouted connections. When an acoustic wave encounters a new material, in this case, a defect, its propagation characteristics, such as amplitude, phase and wavelength, are altered because of the change in material characteristics, such as density and sound velocity [26]. This change in material characteristics also causes a reflection within the medium, with a different, complex amplitude [25]. By analysing the reflected signal, the existence of a defect can be determined [27]. The time dependence $e^{-\omega t}$ is used in this study, where ω and t are the angular frequency and time, respectively.

2.1.1 Density

Density plays a crucial role in the field of acoustics, owing to its significant impact on the propagation of sound waves [26]. Density ρ refers to a material's mass m per unit volume V:

$$\rho = \frac{m}{V} \qquad [28] \tag{2.1}$$

Density is a fundamental property that affects the speed and behaviour of sound [26]. In acoustics, the density of a medium influences its specific acoustic impedance. The specific acoustic impedance is a measure of the ratio of acoustic pressure to the associated particle speed in a medium [26]. For a plane wave the specific acoustic impedance is the product of sound velocity and density and often has a greater acoustical significance than it's components, therefore it is often called characteristic acoustic impedance [26]. Higher densities generally result in higher characteristic acoustic impedance, which can affect the reflection and transmission of sound waves at interfaces of different materials [26]. Moreover, density is a key factor in determining the speed of sound in a medium [26].

2.1.2 Sound velocity

Acoustic waves are a form of elastic waves that can traverse through various media, including gases, fluids and solids [25]. As discussed in Kinsler [26] and Boonyatee [29], certain media possess the property of dispersion, where waves with higher frequencies propagate faster than those with lower frequencies, causing a sound wave to alter its original shape during transmission. As a result, three distinctive sound velocities can be identified. First, the phase velocity pertains to the velocity of a mono-frequency wave in which all points exhibit an

equivalent phase [26, 29]. Second, the group velocity refers to the speed at which waves with slightly different frequencies travel [26, 29]. Finally, the signal velocity can be determined by evaluating the initial onset of the signal [29]. If the medium is frequency-independent, i.e. nondispersive, the signal, phase and group velocities are equal [29]. In this study the effect of dispersion is not studied and it is therefore assumed that the signals phase and group velocities are equal.

The sound velocity in solids can be subdivided into two categories, compressional and shear waves, as noted in Brekhovskikh [30]. Compressional waves display particle displacement parallel to the wavefront, while particle displacement in shear waves is perpendicular to the wavefront [31]. The relationship between compressional and shear waves in solid materials is represented by Poisson's ratio ν, which can be expressed as [32]

$$\nu = \frac{1}{2} \cdot \frac{(\frac{c_p}{c_s})^2 - 2}{(\frac{c_p}{c_s})^2 - 1}, \tag{2.2}$$

where c_p and c_s are the compressional and shear sound velocities, respectively.

Sound velocity in water

As stated in Lurton [30], the sound velocity in water is influenced by temperature, hydrostatic pressure and salinity. However, the experiments and simulations conducted in this master's thesis are performed using freshwater, which is non-saline. Hence, the sound velocity only depends on the temperature T_c (°C) and gauge pressure P_G (bar). This study will adopt a simplified expression for calculating sound velocity in distilled water, c_w as presented by Kinsler [26],

$$c_w = 1402.7 + 488\frac{T_c}{100} - 482\Big(\frac{T_c}{100}\Big)^2 + 135\Big(\frac{T_c}{100}\Big)^3 + \Big(15.9 + 2.8\frac{T_c}{100} + 2.4\Big(\frac{T_c}{100}\Big)^2\Big) \cdot \frac{P_G}{100}, \tag{2.3}$$

The gauge pressure can be calculated with

$$P_G = \frac{\rho_w g d_w}{1 \cdot 10^5}, \tag{2.4}$$

where ρ_w, g and d_w are the density of water, gravitational acceleration and depth [26], respectively. Equation (2.3) has an uncertainty of 0.05% for $0 < T < 100$ °C and $0 < P_G < 200$ bar [23]. The confidence level is not provided, but 95% is assumed. Equation (2.3) is subject to higher uncertainty because of particles in freshwater that may affect the speed of sound.

2.2 Reflection coefficient

When an acoustic wave propagating through a medium reaches the boundary of a second medium, it generates reflected and transmitted waves [26]. The wave properties are determined by the angle of incidence and the characteristics of the media [26].

The critical angle $\theta_{c_{p_1 j}}$ is defined:

$$\theta_{c_{p_1 j}} = \sin^{-1}\left(\frac{c_{p_1}}{c_j}\right) \qquad j = p_2, s_1, s_2 \tag{2.5}$$

where $\theta_{c_{p_1 p_2}}$, $\theta_{c_{p_1 s1}}$ and $\theta_{c_{p_1 s_2}}$ are the critical angles for the transmitted compressional wave and the reflected and transmitted shear waves, respectively; c_{p_1} and c_{p_2} are the compressional waves in media one and two, respectively; and c_{s_1} and c_{s_2} are the shear waves in media one and two, respectively. If the incidence angle exceeds the critical angle, the corresponding wave contains no energy and is evanescent, which results in total reflection [26]. The shear and compressional waves have different critical angles because of the difference in sound velocities [33].

A smaller reflection coefficient leads to more energy being transmitted into the next medium [34]. As a result, the reflection coefficient can be studied to find a suitable frequency range for the transducer. To determine the validity of the equivalent input impedance method, introduced in Section 2.2.1, on a fluid–solid interface with a normal incidence angle (0°), the method is compared to the fluid–solid equation presented in Section 2.2.2. The fluid–solid interface is compared to the simulations in Section 4.2 to determine the simulation's accuracy.

Fig. 2.1 illustrates an incident compressional wave on a solid–solid interface for an incidence angle θ_I less than the critical angles $\theta_{c_{p_1 p_2}}$, $\theta_{c_{p_1 s1}}$ and $\theta_{c_{p_1 s_2}}$. The angle for the reflected wave for the compressional wave is equal to the angle of incidence [26]. However, Snell's law determines the angles for the reflected shear wave and the transmitted shear and compressional waves [26]. Snell's law is given by the following formula [24]:

$$\eta = \frac{\omega}{c_{p1}}\sin(\theta_I) = \frac{\omega}{c_{s1}}\sin(\theta_{R_S}) = \frac{\omega}{c_{p2}}\sin(\theta_{T_P}) = \frac{\omega}{c_{s2}}\sin(\theta_{T_S}), \tag{2.6}$$

where θ_{R_S}, θ_{T_S}, θ_{R_P} and θ_{T_P} are the angles for the reflected and transmitted shear waves (Sv) and reflected and transmitted compressional waves (P), respectively, shown in Fig. 2.1.

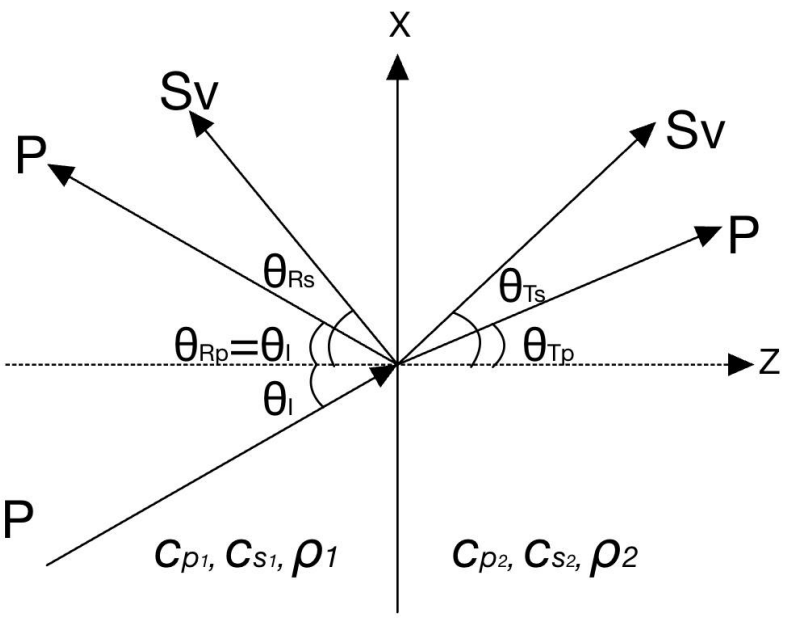

Figure 2.1: Reflection and transmission on solid–solid interface with an incidence compressional wave (P) between two semi-infinite layers. Sv is the shear wave

2.2.1 Reflection coefficient for a fluid–fluid interface

In the context of a fluid–fluid interface, only compressional waves need to be considered [26]. The problem is simplified by assuming a vertical interface between the media and plane waves. The reflection coefficient R_{12} for the compressional wave amplitude between two semi-infinite layers at a fluid–fluid interface can be determined using the following formula [30]:

$$R_{12} = \frac{\frac{Z_2}{\cos(\theta_T)} - \frac{Z_1}{\cos(\theta_{I_I})}}{\frac{Z_2}{\cos(\theta_T)} + \frac{Z_1}{\cos(\theta_I)}}. \tag{2.7}$$

where θ_T is the transmitted angle, shown in Fig. 2.2. The characteristic acoustic impedance for layer n, Z_n, is defined [30]:

$$Z_n = \rho_n c_{p_n} \qquad n = 1, 2 \tag{2.8}$$

where ρ_n and c_{p_n} are the layer's density and compressional sound velocity, respectively, as depicted in Fig. 2.2. The relationship between the transmission coefficient T_{12} and reflection coefficient between two semi-infinite layers at a fluid–fluid interface is

$$T_{12} = R_{12} + 1. \tag{2.9}$$

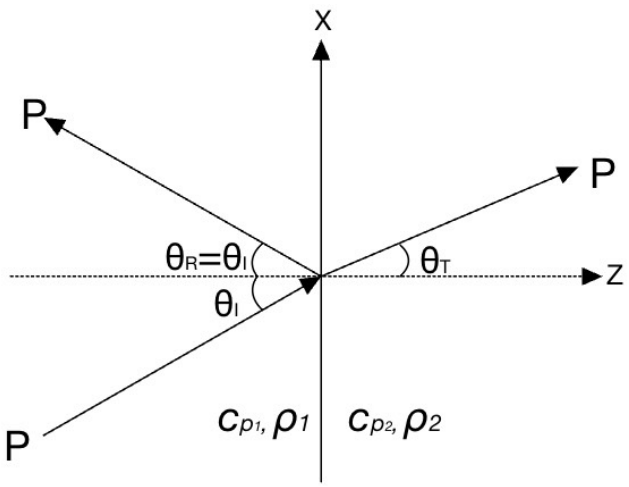

Figure 2.2: Reflection and transmission on a fluid–fluid interface between two semi-infinite layers

The equivalent input impedance method, as outlined in Brekhovskikh [30], is a valuable technique for incorporating additional fluid layers into an acoustic system. This method involves the determination of the input impedance, which is the equivalent of the characteristic acoustic impedance of layers n to one, denoted as $Z_{in}^{(n)}$ [30]. The input impedance for each layer interface can be calculated using the formula [30]

$$Z_{in}^{(n)} = \frac{Z_{in}^{(n-1)} - iZ_n \tan(k_n \cos(\theta_n) d_n \cos(\theta_n)}{Z_n - iZ_{in}^{(n-1)} \tan(k_n \cos(\theta_n) d_n \cos(\theta_n))} Z_n \tag{2.10}$$

where Z_n is the characteristic acoustic impedance of the nth layer, k_n is the wavenumber in the nth layer $k_n = \frac{\omega}{c_n}$ and d_n is the thickness of the nth layer. Each subsequent layer is dependent on the layer after it, with the first and last layers defined as $Z_{in}^{(1)} = Z_1$ and Z_{n+1}, respectively. The resulting reflection coefficient for the compressional wave of the multilayered structure, $R_{(n+1)1}$, can be obtained using the formula

$$R_{(n+1)1} = \frac{Z_{in}^{(n)} - Z_{n+1}}{Z_{in}^{(n)} + Z_{n+1}} \tag{2.11}$$

where $n+1$ is the number of layers, as depicted in Fig. 2.3. Of note, the incidence wave in the equivalent input impedance method is on the last layer of the multilayered structure, $n+1$.

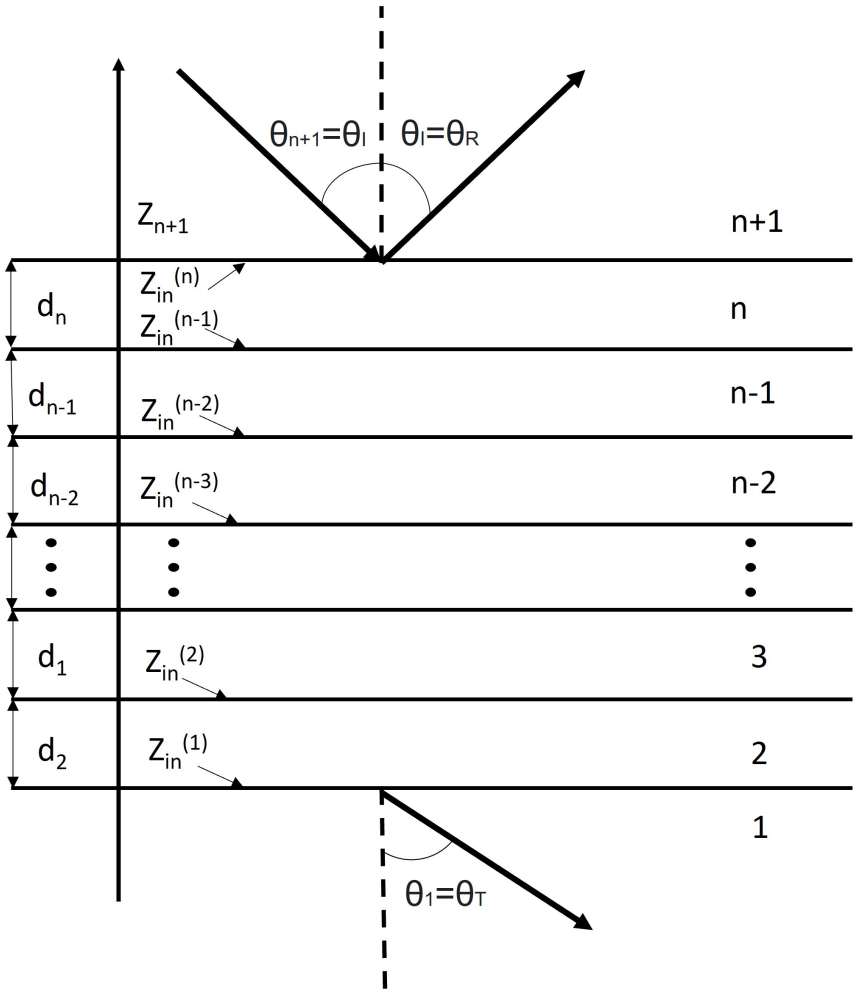

Figure 2.3: Depiction of the equivalent input impedance method, where Z_{in} is equivalent to the characteristic acoustic impedance for layers n to one

2.2.2 Reflection coefficient of fluid–solid interfaces

As shown in Lunde [24], the reflection coefficient between two solids depends on the shear and compressional waves. In this report, where there is a vertical fluid–solid interface along the x-axis, the reflection coefficients for a solid–solid interface are given by the following formulas [24]:

$$R_{Tzz}^{PP} = \frac{A_1^-}{A_1^+} \qquad R_{Tzz}^{PS} = \frac{2\eta k_{z1} B_1^-}{(2\eta^2 - k_1^2)A_1^+} \qquad R_{Tzz}^{SP} = \frac{(2\eta^2 - k_1^2)A_1^-}{2\eta k_{z1} B_1^+} \qquad R_{Tzz}^{SS} = \frac{-B_1^-}{B_1^+} \quad (2.12)$$

which have to be altered by removing the shear waves in the first medium, as shown in Fig. 2.4, where $R^{PP}_{T_{ZZ}}$ and $R^{PS}_{T_{ZZ}}$ are the reflection coefficients for normal stress T_{ZZ} with an incident compressional wave and reflected compressional and shear waves, respectively; $R^{SP}_{T_{ZZ}}$ and $R^{SS}_{T_{ZZ}}$ have an incident shear wave instead of a compressional wave; η is the horizontal part of the wave numbers $\eta = k_{x1} = h_{x1} = h_{x2} = k_{x2}$; h is the wavenumber for the shear wave; k_z is the vertical part of h; and A^+ and A^- are the complex amplitudes for the displacement potential for compressional waves propagating in the positive and negative z-directions, respectively, while B^+ and B^- are those for the shear waves. Subscripts 1 and 2 are for the first and second media, respectively.

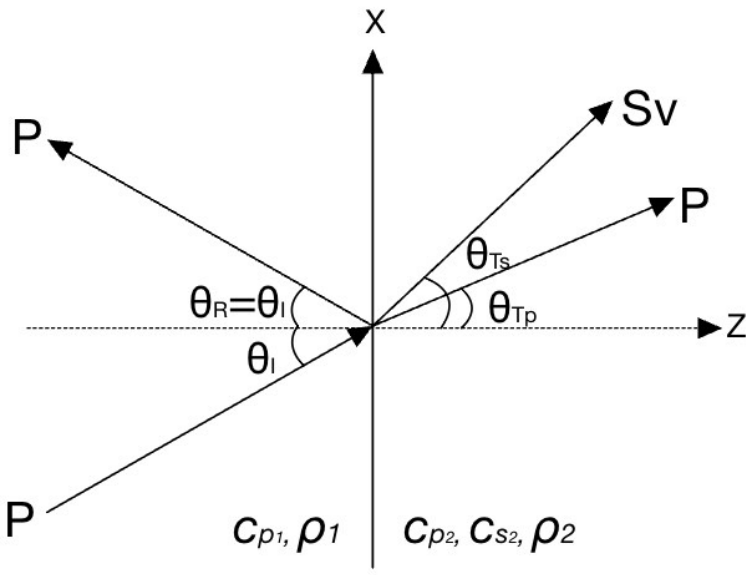

Figure 2.4: Reflection and transmission on fluid–solid interface with an incidence plane pressure wave between two semi-infinite layers

The boundary conditions for a solid–solid horizontal interface along the x-axis at the interface at $z = 0$, [24]

$$u_{x,1} = u_{x,2} \qquad u_{z,1} = u_{z,2} \qquad T_{zz,1} = T_{zz,2} \qquad T_{xz,1} = T_{xz,2}, \tag{2.13}$$

where u_x is the displacement in the x-direction. The boundary conditions are used to find the following governing equations [24]:

$$\eta(A_1^+ + A_1^-) - k_{z1}(B_1^+ - B_1^-) = \eta A_2^+ - k_{z2} B_2^+, \tag{2.14}$$

$$h_{z1}(A_1^+ - A_1^-) + \eta(B_1^+ + B_1^-) = h_{z2}A_2^+ \eta B_2^+, \tag{2.15}$$

$$\mu_1(2\eta^2 - k_1^2)(A_1^+ + A_1^-) - \mu_1 2\eta k_{z1}(B_1^+ - B_1^-) = \mu_2(2\eta^2 - k_z^2)A_2^+ - \mu_2 2\eta k_{z2}B_2^+ \tag{2.16}$$

$$\mu_1 2\eta h_{z1}(A_1^+ + A_1^-) - \mu_1(2\eta^2 - k_1^2)(B_1^+ - B_1^-) = \mu_2 2\eta h_{z2}A_2^+ + \mu_2(2\eta^2 - k_z^2)B_2^+, \tag{2.17}$$

which describe the relations between the incident and reflected waves for a solid–solid interface, where μ is the shear modulus, h_z is the vertical component of h.

The reflection coefficient for a fluid–solid interface is derived from the reflection coefficient for a solid–solid (2.12) by altering the left side of the governing Equations (2.14),(2.15)(2.16) and (2.17) to correspond to a fluid material. The shear modulus for medium one is set to zero, resulting in zero B^+ and B^- in the medium [24]. To avoid an overdetermined system, the boundary condition $u_{x,1} = u_{x,2}$ is omitted, which allows for slippage between the fluid and solid in the x-direction [24]. As shown in Lunde [24], $\rho_1\omega^2$ is the result of applying $\mu_1 = 0$ to $\mu_1(2\eta^2 - k_1^2)$. The resulting equations

$$h_{z1}(A_1^+ - A_1^-) = h_{z2}A_2^+ \eta B_2^+, \tag{2.18}$$

$$\rho_1\omega^2(A_1^+ + A_1^-) = \mu_2(2\eta^2 - k_z^2)A_2^+ - \mu_2 2\eta k_{z2}B_2^+ \tag{2.19}$$

$$\mu_2 2\eta h_{z2}A_2^+ + \mu_2(2\eta^2 - k_z^2)B_2^+ = 0, \tag{2.20}$$

describe the relationship between the incident and reflected waves for a fluid-solid interface, where ρ_1 is the material density for the first medium.

Since no shear waves exist in the fluid material, the reflection coefficients that include shear waves $R_{T_{ZZ}}^{PS}$,$R_{T_{ZZ}}^{SP}$ and $R_{T_{ZZ}}^{SS}$ are of no interest. The compressional wave reflection coefficient for a fluid–solid interface is

$$R_{T_{ZZ}}^{PP} = \frac{A_1^-}{A_1^+}. \tag{2.21}$$

The solution for the complex amplitude A_1^- with an incident amplitude of $A_1^+ = 1$ is derived

from the governing Equations (2.18), (2.19) and (2.20),

$$A_1^- = \frac{-h_{z1} + h_{z2}G - \frac{2\eta^2 h_{z2}}{H}G}{-h_{z1} + h_{z2}G + \frac{2\eta^2 h_{z2}}{H}G}, \tag{2.22}$$

where the procedure is shown in Appendix A and G and H are given by the following equations:

$$G = \frac{\rho_{0,1}\omega^2}{-\mu_2(2\eta^2 - k_2^2) - \frac{4\mu_2\eta^2 k_{z2}h_{z2}}{2\eta^2 - k_2^2}} \tag{2.23}$$

$$H = \eta^2 - k_2^2. \tag{2.24}$$

To test the formula's validity, the shear modulus μ_2 in the solid medium is gradually reduced, and the result is compared to the fluid–fluid equation model (Equation (2.7)) described in Section 2.2.1. The fluid–solid model converges towards the fluid–fluid model, as shown in Appendix D.

2.3 Near and far fields

The concepts of near and far fields are fundamental in the field of acoustics, providing a framework for understanding the propagation characteristics of acoustic waves emitted from a source [26]. In the near-field, the contributions from different points on the source have comparatively large differences in traveling distance, and as a results are strongly out of phase and interact constructively and destructively [33, 35]. The resulting pressure field is complex, oscillating with distance [33, 35]. However, its average intensity decreases by $1/r^2$ for spherical spreading [33], where r is the distance from the source. As the distance from the source increases, the acoustic wave transitions into the far-field region. In this region, the path difference between the signals coming from the different points of the transducer is comparatively small, resulting in a minor variation in phase [33, 35], which means all the interference between the signals is constructive [33]. As a result, the far-field pressure decreases monotonously with distance and converges at large distances toward spherical spreading [33]. An example of this is shown in Fig. 2.5, where the pressure from a baffled circular piston in water with a radius $a = 0.05$, velocity amplitude $U_0 = 1$ and a frequency $f = 100$ kHz; the pressure amplitude on the axis converges towards spherical spreading.

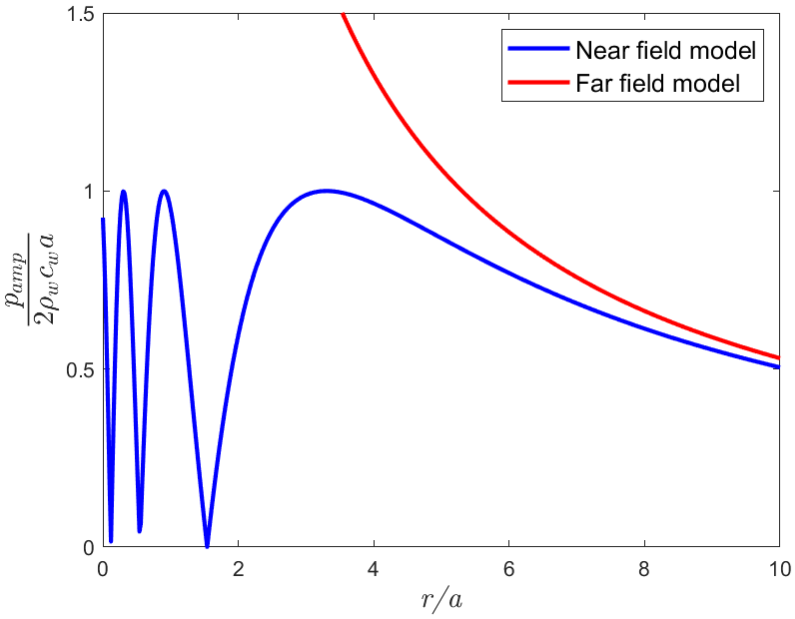

Figure 2.5: Near and Far field pressure amplitude p_{amp} models for a baffled circular piston radiating into water. Plotted against the distance from the piston r divided by the radius of the piston $a = 0.05$ m. Properties of water: sound velocity $c_{p_w} = 1481$ m/s and density $\rho_w = 1000$ kg/m^3. Equations from Kinsler [26] for time t=0 and frequency f=100kHz.

The validity of the far-field model for a baffled piston model can be estimated with the Rayleigh length [26]. The Rayleigh length Z_R is a parameter that characterises the spatial extent of the near field and depends on the radius of the transducer a and the wavelength λ [26]:

$$Z_R = \frac{\pi a^2}{\lambda} \tag{2.25}$$

2.4 Acoustic pressure, beam pattern and beam width for a baffled circular plane piston

The baffled circular plane piston model consists of a rigid circular uniform piston, where the hole piston moves with the same displacement, placed in a fluid with a rigid infinite wall behind it, shown in Fig. 2.6. The result is the compressional wave able to radiate within only 180 degrees in front of the piston. The models in this section are compared to the simulations in Chapter 4 to determine the simulation's accuracy.

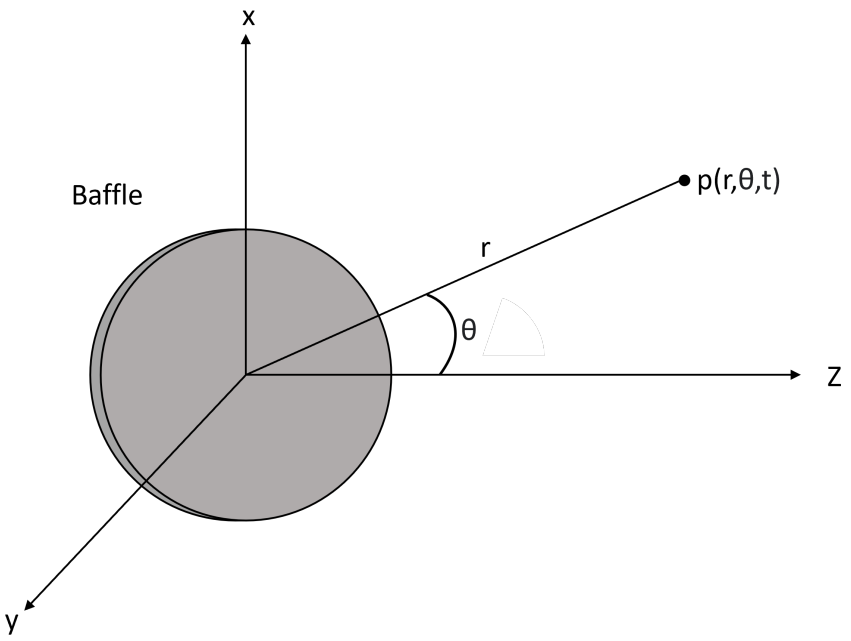

Figure 2.6: Circular plane piston mounted on a flat and rigid baffle of infinite extent

As discussed in Kinsler [26], the acoustic response in the far field and along the acoustic axis, the z-axis, from a baffled circular plane piston radiating into a uniform medium can be determined by the following formulas:

$$p(r,\theta,t) = \frac{j}{2}\rho c_p U_0 \frac{a}{r} ka \frac{2J_1(kasin(\theta)}{kasin(\theta))} e^{j(\omega t - kr)} \tag{2.26}$$

$$p(r,0,t) = \rho c_p U_0 \left(1 - e^{-jk(\sqrt{r^2+a^2}-r)}\right) e^{j(\omega t - kr)}, \tag{2.27}$$

respectively, where J_1 is the first order Bessel function of the first kind and U_0 and θ are the velocity amplitude and angle from the sound axis ($z - axis$), respectively. The baffled circular plane piston is depicted in Fig. 2.6. The far-field acoustic pressure can be expressed as a product of axial pressure,

$$P_{ax}(r,t) = \frac{j}{2}\rho_0 c_0 U_0 \frac{a}{r} ka e^{j(\omega t - kr)}, \tag{2.28}$$

and a directional factor,

$$H(\theta) = \frac{2J_1(ka\sin(\theta)}{ka\sin(\theta)}, \tag{2.29}$$

$$p(r, \theta, t) = P_{ax}(r)H(\theta) \qquad [26]. \tag{2.30}$$

The directional factor can determine the beam pattern $b(\theta)$ [26]:

$$b(\theta) = 20\log_{10}(H(\theta)). \tag{2.31}$$

The beam width is a measure of the angular extent over which the intensity of a signal has decreased by a certain threshold value from the sound axis [26]. To define the effective width of the major lobe, the values of $20\log_{10}\frac{p(r,\theta,t)}{P_{ax}(r,t)}$ are examined. No definition is universally accepted for the specific value of $20\log_{10}\frac{p(r,\theta,t)}{P_{ax}(r,t)}$ that delineates the beam width [26]. However, in this report, the beam width refers to the angle corresponding to half amplitude, specifically -6 dB for the pressure amplitude $20\log_{10}\frac{p(r,\theta,t)}{P_{ax}(r,t)}$ unless otherwise specified. This corresponds to the angle for -3 dB for the intensity I, given by formula $10\log_{10}\frac{I(r,\theta,t)}{I_{ax}(r,t)}$. An illustration of the beam width given by Equation (2.31) for a baffled circular uniform piston in water with a radius of 0.05 m and a frequency of 100 kHz is depicted in Fig. 2.7.

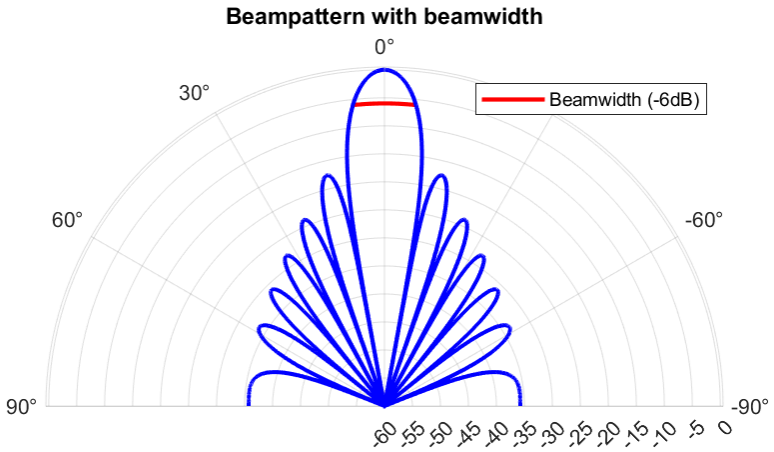

Figure 2.7: Beam pattern for Equation (2.31) for a baffled circular uniform piston in water with a radius 0.05 m, a frequency of 100 kHz and a -6dB beam width marked in red. The water has a density of 1000kg/m^3 and sound velocity of 1481 m/s

2.5 Transducer characteristics

Electro-acoustic transducers play a crucial role in the transmission and reception of underwater acoustic signals [33]. These devices convert acoustic energy (mechanical energy) to electrical energy, and vice versa [33]. The performance and suitability of electro-acoustic transducers for particular applications depend on their electrical and acoustical characteristics [33]. This section covers important transducer characteristics, including source and receiver sensitivity, electrical impedance, Q-factor and bandwidth. Section 2.4 addresses the definition of beam width and beam pattern.

2.5.1 Source and receiver sensitivity

In the field of transducers, the receiver- and source sensitivity play a crucial role in determining the performance and effectiveness of the transducer system [36]. Source sensitivity relates to the transducer's ability to convert electrical signals into pressure waves measured at reference distance $r = 1$ m [36]. The sound pressure is measured in the far field and, if necessary, extrapolated to the reference distance [36]. The source sensitivity can be defined with the current I or the voltage V [36]:

$$S_I = \frac{p(r = 1 \text{ m}), \theta = 0}{I} \tag{2.32}$$

and

$$S_V = \frac{p(r = 1 \text{ m}), \theta = 0}{V}, \tag{2.33}$$

respectively. The receiver sensitivity refers to the ability of a transducer to convert incoming acoustic signals into electrical signals [36]. It is defined as the relationship between the voltage V from the receiver with an open circuit and the free field acoustic pressure p [36]

$$M = \frac{V}{p}. \tag{2.34}$$

RVR and TVR represent the logarithmic source and receiver sensitivity values, respectively, with FOM being the sum of RVR and TVR [37, 38]. RVR is determined using the following formula [37]:

$$RVR = 20\log_{10}\left(\frac{M}{\frac{1V}{1\mu Pa}}\right), \tag{2.35}$$

while TVR is calculated using the following formula [37]:

$$TVR = 20\log_{10}\left(\frac{S_V}{\frac{1\mu Pa}{1V}}\right). \tag{2.36}$$

AIRMAR's approach to measuring RVR and TVR is detailed in Appendix G.

2.5.2 Transducers electrical impedance and admittance

The electrical impedance and admittance of an acoustical transducer provide valuable information about its electrical characteristics and behaviour [39]. They reflect the complex relationship between the voltage and current responses of the transducer when an electrical signal is applied [39]. Analysing the electrical impedance and admittance can gain insights into the transducer's electrical performance, such as its efficiency [36]. The electrical impedance and admittance can be measured as functions of frequency using an impedance analyser [39].

At a series resonance frequency f_s, the transducer exhibits a maximum conductance, which is the real part of admittance, indicating the most dissipated effect and highest sound intensity [36]. The bandwidth in this study is defined as the frequency range over which the electrical impedance is within -3 dB [39]. The bandwidth corresponds to the range where the transducer's response is considered acceptable and functional for the desired application.

The Q-factor of an acoustical transducer can be estimated by analysing its electrical conductance or impedance [39]. It is a measure of the selectivity or sharpness of the resonance of the transducer, providing information about its bandwidth and energy dissipation [39, 36].

The electrical impedance curve around the maximum frequency top (resonant frequency f_n) is examined to determine the Q-factor [39]. The Q-factor is related to the width of the electrical impedance curve at its -3 dB points (half-amplitude points) on either side of the resonance [39]. By measuring the distance between the -3 dB points on the electrical impedance curve and dividing it by the resonant frequency, the Q-factor can be calculated. Mathematically, the Q-factor can be expressed as [39]

$$Q = f_n/\Delta f, \tag{2.37}$$

where Δf is the bandwidth of the electrical impedance curve at the -3 dB points.

A higher Q-factor indicates a more narrow band response with a sharper resonance peak, while a lower Q-factor signifies a broader bandwidth and a less pronounced resonance [36, 39]. The lower the Q-factor, the less ringing in the ceramic element and the better the performance of AIRMAR transducers [38]. Ringing refers to the amount of time the ceramic elements vibrate after the input signal [38].

2.6 Finite element method

The description of the laws of physics for space- and time-dependent problems are usually expressed in terms of partial differential equations (PDEs) [40]. For most geometries and problems, these PDEs cannot be solved with analytical methods [40]. Instead, the equation can be approximated, typically based upon different types of discretisations [40]. These discretisation methods approximate the PDEs with numerical model equations, which can be solved using numerical methods [40]. The solution to the numerical model equations is, in turn, an approximation of the real solution to the PDEs [40]. The finite element method (FEM) is used to compute such approximations [40].

In this master thesis, the finite element (FE) program COMSOL is chosen for the simulations. The problems in this study have to be discretised in time and space. Space discretisation involves creating a mesh by dividing the area of interest into smaller pieces called elements, which is comprised of nodes [40]. The nodes are where the calculations take place [40]. Solutions for the points between these nodes are interpolated from neighbouring nodes, providing a continuous solution [40, 41]. Time discretisation is the time increment between each calculation [41].

2.6.1 Time-explicit and -implicit

This study explores the use of both time-implicit and -explicit solvers. The time-explicit and -implicit solvers address dynamic problems by calculating a series of time increments [41]. The difference between these methods is in how they increment time [23].

The time-implicit solver calculates each increment by first establishing the model's global equilibrium, meaning that each increment has to converge [23]. After verifying the global

equilibrium, the solver calculates the variables [23]. The variables for the time-implicit solver are pressure for the *Pressure Acoustics, Transient* module (fluid physics) and displacement for the *Solid Mechanics* module (solid physics) [42]. The equations for the time-implicit fluid physics is [42]

$$\frac{1}{\rho c_p^2}\frac{\partial^2 p_t}{\partial t^2} + \nabla \cdot \left(\frac{-1}{p}(\nabla p_t - q_d)\right) = Q_m, \tag{2.38}$$

where p_t, q_d, $\nabla\cdot$, ∇ and Q_m are the total acoustic pressure, fluid density, dipole domain source (representing a domain volumetric force), divergence, gradient and a mono-pole domain source (source with a uniform strength in all directions), respectively. The equation for the time-implicit solid physics is [42]

$$\rho\frac{\partial u}{\partial t^2} = \nabla \cdot S + F_v, \tag{2.39}$$

where F_v is the volume force vector for the undeformed volume and S is the strain.

The time-explicit solver assumes that the global equilibrium is verified and does not have to converge each increment [23]. Therefore, the time-explicit solver only calculates the variables. To assume that the global equilibrium exists, the time increments have to be extremely small [23]. Otherwise, equilibrium cannot be maintained. The variables for the time-explicit solver are pressure and displacement for the *Pressure Acoustics, Time Explicit* (fluid physics) and structural velocity v for the *Elastic Waves, Time Explicit* (solid physics). The equations for the time-explicit fluid physics is [42]

$$\frac{1}{\rho c^2}\frac{\partial p_t}{\partial t} + \nabla \cdot u_t = Q_m, \tag{2.40}$$

$$\rho\frac{\partial u_t}{\partial t} + \nabla \cdot (p_t I_t) q_d, \tag{2.41}$$

where u_t is the total acoustic velocity and I_t is the unit matrix. The equations for the time-explicit solid physics is [42]

$$\rho\frac{\partial v}{\partial t} - \nabla \cdot S = F_v, \tag{2.42}$$

$$\frac{\partial \epsilon}{\partial t} - \frac{1}{2}(\nabla v + (\nabla v)^T) = 0, \tag{2.43}$$

where ϵ is the strain tensor.

The time-explicit solver does not iterate for the global equilibrium and, thus, calculates the time increments faster than the time-implicit solver [23]. However, the time-implicit solver allows for larger time increments, resulting in fewer calculations. As a result, the time-implicit solver is better in situations where high time resolution is unnecessary [23]. Conversely, the time-explicit solver is better when high time resolution is needed. Therefore, in this study, where ultrasound is simulated, the time-explicit solver is expected to be more efficient [23].

2.7 Defects

Several defects are of interest in offshore structures. The most common are debonding and slippage between the grout and steel, as well as cracks and voids in the grout [3]. This study focuses on voids in the grout, particularly the deeper layers of the grout; therefore, slippage and debonding, which occur in the boundary of the steel and grout, are not considered. Voids in the grout are of concern because they are larger and easier to spot than cracks, and confirm the penetration of the grout if discovered. For the effective detection of defects in grout, a general rule of thumb is that the size of the defect should be at least half the wavelength [43].

2.8 Resonance frequencies

Acoustic resonance refers to the phenomenon that occurs when an object or cavity vibrates at its natural frequency in response to an external sound stimulus [26, 44]. It is a fundamental principle in the acoustics field, significantly impacting the scattering cross-section, which maximises during resonance [26]. When a sound wave aligns with the natural frequency of an object or resonant cavity, the energy of the sound efficiently transfers to the vibrating system, resulting in a substantial increase in vibration amplitude [26, 44]. This amplification of vibrations can manifest as audible sounds or even structural oscillations [44]. The comprehensive understanding and effective control of acoustic resonance phenomena are crucial for optimising the performance of acoustic measurements [44]. Therefore, the study of acoustic resonance is vital in theoretical research and practical applications concerning sound and vibration [44].

In this study, the focus revolves around four significant resonance frequencies: a gas-filled spherical cavity in a solid material, a gas-filled cylindrical cavity in a solid material, a cube-shaped solid and a solid plate with infinite width. In this case, the gas-filled cylindrical cavity and cube-shaped solid have multiple close resonances. When resonant frequencies are closely situated, the vibrational modes associated with these frequencies can interact and influence each other [45]. This interaction, known as modal coupling, leads to modifications in the resonant frequency, making it challenging to determine [45]. To address this, FEM is employed to determine the resonance frequency for the coupled modes. FEM analysis is utilised to estimate the resonance frequency for the gas-filled cylindrical cavity by modelling a gas-filled cylinder with rigid boundary conditions. Similarly, the resonance frequency for the cube-shaped solid is estimated using FEM analysis on a cube-shaped solid placed in a vacuum environment.

The resonance frequency f_0 for the gas-filled spherical cavity in a solid is found with the equation

$$f_0 = \frac{1}{2\pi a_b}\left(\frac{3\gamma P_0}{A\rho_s} + \frac{4G}{\rho_s}\right)^{\frac{1}{2}}, \tag{2.44}$$

where a_b, γ, P_0, ρ_s and G are the bubble radius, ratio of specific heats of the gas, ambient hydrostatic pressure of the gas, density of the solid and shear modulus of the solid, respectively [46], and A is the gas polytropic coefficient given by the following equation:

$$A = (1 + B^2)\left[1 + \frac{3(\gamma - 1)}{X}\left(\frac{\sinh(X) - \sin(X)}{\cosh(X) - \cos(X)}\right)\right], \tag{2.45}$$

where X and B are given by equations

$$B = 3(\gamma - 1)\left(\frac{X(\sinh(X) + \sin(X)) - 2(\cosh(X) - \cos(X))}{X^2(\cosh(X) - \cos(X)) + 3(\gamma - 1)(\sinh(X) - \sin(X))}\right), \tag{2.46}$$

$$X = \frac{r\omega\rho_g s_p}{C_p} \tag{2.47}$$

respectively [44], where ρ_g, s_p and C_p are the density of the gas, specific heat at a constant pressure of the gas and thermal conductivity of the gas, respectively.

The resonant frequency for a solid plate width infinite width is the thickness resonance

frequency, which can be determined with formula [47]:

$$f_0 = \frac{c_0}{2d}, \tag{2.48}$$

where d is the thickness of the plate. This thickness resonance is calculated both for the compressional- and shear waves.

2.8.1 Scattering cross section

The scattering cross section σ_s is a measure of how much energy is radiated away by scatters [48]. The acoustical scattering cross section of gas spheres is significant because of the compressible nature of the gases, which can result in a significantly larger scattering cross section compared to the geometric cross section [48]. The scattering cross section of the gas-filled spherical defect can be calculated with formula [49]:

$$\sigma_s = \frac{4\pi a_b^2}{((f_0/f)^2 - 1)^2 + \delta}, \tag{2.49}$$

where δ is the dampening constant taken from [49]. Formula 2.49 is from Medwin [49], which is for a fluid sphere within a fluid medium. In this study the scattering from a fluid sphere within a solid medium is of interest, but this formula was not located [50].

2.9 Attenuation

Attenuation in acoustics refers to the decrease in the intensity or energy of sound waves as they travel through a medium [26]. This reduction is due to various factors, including absorption, scattering and reflection, leading to a decrease in the amplitude and energy of the sound wave over distance or as it interacts with the medium and surrounding objects.

In the case of concrete, the primary contributors to energy loss are absorption within the material and scattering from the aggregates and air bubbles present in the concrete [51]. Absorption is a common attenuation mechanism in acoustics, where the material absorbs sound energy. The absorbed energy is then converted into other forms, such as heat, reducing the sound's intensity [26]. Scattering, on the other hand, takes place when sound waves encounter minor irregularities or objects in their path. As a result, the waves are scattered

in various directions, leading to an overall decrease in the intensity of the sound field [26].

This study adopts the Rayleigh damping model because of its compatibility with the simulation program COMSOL. Rayleigh damping has gained wide acceptance in dynamic analysis, owing to its advantageous feature of being proportional to the stiffness and mass of the structure, allowing for a convenient decoupling of dynamic equations [52]. Moreover, the structural damping ratio derived from Rayleigh damping is frequency-dependent, making it more suitable for accurately reflecting the dynamic properties of the structures [52]. The Rayleigh damping coefficient, R_α, is related to mass and stiffness s through the equation

$$R_\alpha = \alpha m + \beta s, \tag{2.50}$$

where α and β are the mass and stiffness damping coefficients, respectively [52]. These damping coefficients can also be employed to compute the damping in decibels per meter (dB/m) using the equation

$$\alpha_{dB} = \frac{\alpha}{2c_p} + \frac{\beta}{2c_p}\omega \qquad [52] \tag{2.51}$$

.

2.10 Signal processing

Signal processing plays a vital role in acoustics by analysing, manipulating and improving sound signals [53]. Its primary objective is to enhance signal components in the presence of noise or to transform measured datasets to reveal new features [53]. Acoustic signals are inherently complex, containing valuable information about the surrounding environment [53]. Signal processing techniques enable us to extract and interpret this information effectively [53]. In the field of acoustics, signal processing finds application in measurement systems where tasks like noise reduction, equalisation, spatial imaging and reverberation control are crucial [53]. Researchers and engineers can derive meaningful insights from sound signals and conduct accurate measurements and analyses by employing signal processing in acoustics [53].

2.10.1 Filters

Filters are crucial when modifying the frequency content of signals [53, 54]. Three commonly used filters are low-, high-, and band-pass filters, each designed to pass or attenuate specific

frequency ranges selectively.

A low-pass filter allows frequencies below a specific cutoff value to pass through while attenuating higher frequencies [53, 54]. It effectively removes or reduces high-frequency components, allowing for the retention of a signal's lower-frequency components. Conversely, a high-pass filter allows frequencies above a specified cutoff value to pass through while attenuating lower frequencies [53, 54]. As the name suggests, a band-pass filter allows a specific range or 'band' of frequencies to pass through while attenuating frequencies outside this range [53, 54]. It effectively combines a low- and high-pass filter, isolating signals within a desired frequency range.

These filter types can be implemented using various techniques, including analogue circuits, digital filters and software algorithms [53, 54]. In this study, digital filters are implemented. The choice of filter type depends on the application's specific requirements, such as desired frequency range, cutoff steepness and the attenuation needed for out-of-band frequencies [53, 54]. By appropriately selecting and applying these filters, the signal's shape and frequency content can be manipulated to meet their desired objectives [53, 54].

2.10.2 Fast Fourier transform

The fast Fourier transform (FFT) is an efficient algorithm widely used in digital signal processing and applied mathematics to compute the discrete Fourier transform (DFT) and its inverse (IDFT) [55]. The DFT is a mathematical transformation that allows us to analyse signals in the frequency domain. The DFT decomposes a time-domain signal or sequence of data points into its frequency components, revealing the presence of various frequencies and their corresponding magnitudes. By converting signals from the time domain to the frequency domain, the DFT enables applications such as spectral analysis, filtering, compression and audio processing. The IDFT can be applied to reconstruct the original time-domain signal from its frequency representation [55].

The FFT revolutionised signal processing by significantly reducing the computational complexity of Fourier analysis, making Fourier transforms practical to compute for large datasets [55]. Its speed and versatility make it an indispensable tool in numerous disciplines, including acoustics [55]. The FFT and inverse FFT (IFFT) uesed in this study are given by equations [56]

$$Y = \sum_{j=1}^{n} X(j) W_n^{(j-1)}, \tag{2.52}$$

$$X = \frac{1}{n} \sum_{j=1}^{n} Y(j) W_n^{-(j-1)}, \tag{2.53}$$

where Y and X are the frequency- and time-domain signals, respectively, and W_n is given by [56]

$$W_n = e^{\frac{-2\pi i}{n}}. \tag{2.54}$$

Zero padding is utilised to increase the frequency resolution by adding zeroes at the end of the time-domain signal to increase the number of samples in the frequency spectrum [55]. The zeroes at the end of the time-domain signal can ensure that the signal length is in the sequence of the power of two, increasing computational speed [55].

Windowing

Window functions, also known as tapering functions, play a crucial role in signal processing, particularly in the context of the Fourier transform [57, 55]. These functions are applied to a signal segment before performing analysis, such as the FFT, to reduce spectral leakage and minimise the impact of signal truncation [57, 55]. The windows considered in this study are the Hamming and Hanning functions, some of the most commonly used window functions, which balance amplitude accuracy, spectral leakage and main lobe width well [57, 55].

The Hamming window tapers the signal smoothly towards the edges, reducing abrupt transitions and spectral artefacts [57]. The Hamming window provides a balance between good beam width and moderate side lobe attenuation [57, 55]. The Hamming window is especially effective on the first side lobe [57]. Hamming window is defined as [58]

$$w_{Hann}(n) = 0.54 - 0.46 cos\left(2\pi \frac{n}{N}\right) \qquad 0 \leq n \leq N, \tag{2.55}$$

which assigns weight values to each sample in the segment n for the length of the signal N, creating a smooth transition from the centre to the edges [57, 55]. The Hanning window is similar to the Hamming window but with slightly different weight values given by [59]

$$w_{Hamm}(n) = \frac{1}{2}\left(1 - cos\left(2\pi\frac{n}{N}\right)\right) \qquad 0 \leq n \leq N. \tag{2.56}$$

The Hanning window provides improved side lobe suppression at the expense of slightly wider main lobes [57, 55]. The rectangular window does not apply tapering and is equivalent to no windowing. The rectangular window has the narrowest main lobe but suffers from significant side lobe leakage [57, 55].

2.10.3 Averaging

In signal processing, averaging is a commonly used technique to reduce noise and enhance the quality of signals [53, 54]. It involves taking multiple measurements or samples of a signal and calculating the average value at each point [53, 54]. The purpose of averaging in signal processing is to attenuate random variations or unwanted noise present in the signal [53, 54]. However, averaging does not help remove systematic noise [53]. Averaging can be particularly useful when dealing with noisy signals, such as sensor measurements [54]. By reducing random fluctuations and emphasising the underlying signal, averaging helps improve the accuracy and reliability of subsequent signal analysis [54].

Several conditions for the use of averaging are listed [53]:

- Signal and noise are uncorrelated.
- The timing of the signal is known.
- A consistent signal component exists when performing repeated measurements.
- The noise is truly random with zero mean.

In practice, all these assumptions are violated to some degree, but the averaging technique has been proven remarkably robust for minor violations [53].

Different averaging techniques are used depending on the specific application [53]. The method used in this study is called arithmetic averaging, where multiple samples of the signal are added together and divided by the number of samples. This technique helps to smooth out high-frequency noise and improve the signal-to-noise ratio [53].

Chapter 3

Experimental setup and methods

This chapter encompasses the systematic design, implementation, and execution of the experiments, employing appropriate methodologies, equipment, and measurement techniques. The conducted experiments included both electric and acoustic measurements, in addition to assessments of dimensions and mass. An overview of the employed equipment is provided in Section 3.1. Section 3.2 explain the measurement setup, including details of the samples' dimensions and the standoff distance.

The characteristics of the transducer are presented in Section 3.3, encompassing factors such as the frequency range and electrical- and acoustical properties. The electronic components within the measurement system are addressed in Section 3.4. Material characteristics relevant to the grout and water are discussed in Section 3.5. The creation of defects is detailed in Section 3.6, while the signal processing procedures applied to the signals are explained in Section 3.7.

3.1 Equipment

An overview of the equipment used is given in Table 3.1.

Table 3.1: List of equipment

Type of equipment	Brand	Serial number/article number
Physical measurements		
Digital caliper	Cocraft	40-8747
Digital scale	Duxa	7090016047093,00
Digital scale	Clas Ohlson	44-2591-1
Water tank	Fig. 3.5	
Electrical measurements		
Impedance analyzer	Bode 100	RK151K
Acoustical measurements – Instruments		
Transducer	AIRMAR	B175M
Amplifier	TSC subsea	PA12
Receiver	TSC subsea	ADM 16.6761.14.10.16
Oscilloscope	Tenma 72-31555	2170004070
Thermometer	Termometerfabriken viking AB	36-1613
Signal generator	Aim-TTi CPX400S	435690
Acoustical measurements – Positioning		
Small levelling tool		
Standard levelling tool		
3-Axis Scanning System	LG Motion Fig. 3.1	
Ruler	Kellen	7025180622883
Concrete		
Ordinary Portland cement (OPC) (42,5R)	Infra	7025180654921,00
Bucket 20L		
Tub 90L		
Mortar stirrers	Biltema	17-391
Stand for grout	Fig. 3.2	
Concrete vibrator	Meec Tolls	271001
Heavy-duty fishing thread	Campelen	

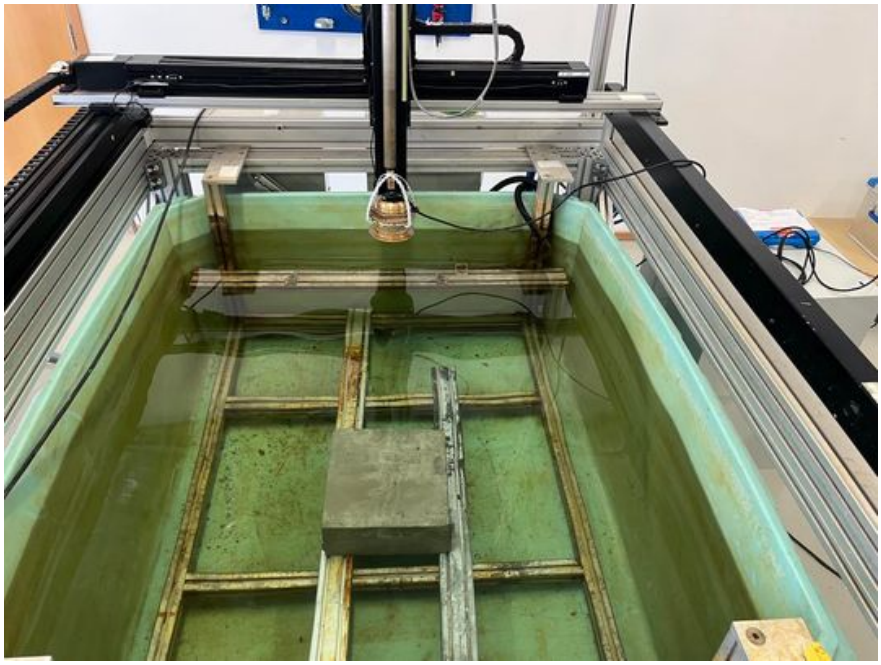

Figure 3.1: Picture of measurement setup

Figure 3.2: Gout mould with cylindrical defect

3.2 Measurement setup

The primary objective of this study is to investigate the penetration depth of the grout. Therefore, the steel plates were removed from the grout, allowing for a more thorough examination of the grout without any interference. However, because of mould limitations, the dimensions of the grout were constrained to 30 cm wide, 30 cm long and 15 cm deep, Fig. 3.3, with a 2D depiction of the model in Fig. 3.4.

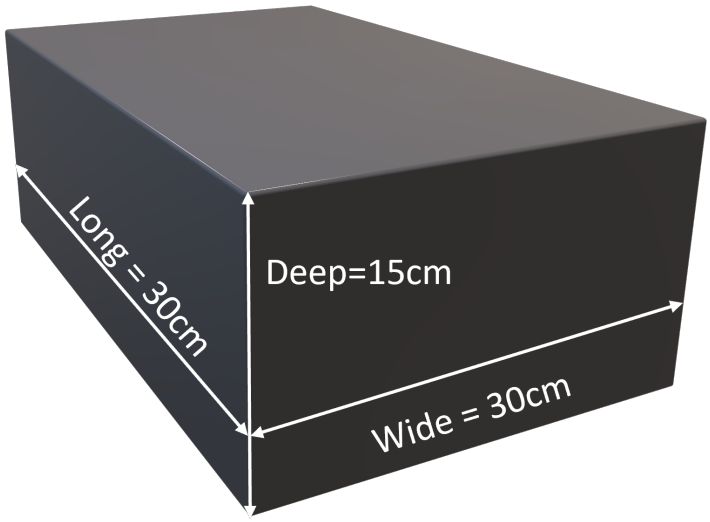

Figure 3.3: Dimensions of grout

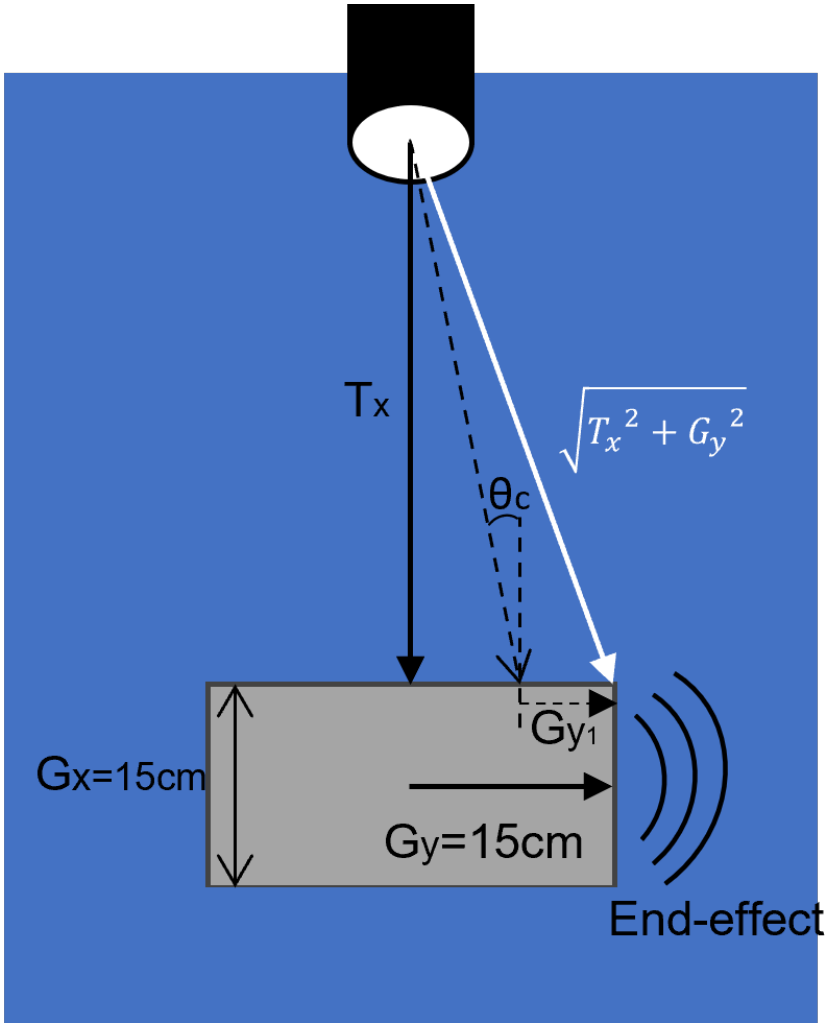

Figure 3.4: Depiction of the measurement setup

In the experimental setup, a water tank was utilised with dimensions of $1 \times 1.3 \times 1.8$ m, with the grout sample placed in the middle of the tank 10 cm from the bottom, as illustrated in Fig. 3.5. The maximum distance between the transducer and the grout sample, known as the standoff distance, was limited to 60 cm.

Several factors must be considered when choosing the standoff distance, the distance between the transducer and the grout sample. The dimension limitation of the grout made end-effects a concern. Another limiting factor is the reflection from the transducer and the side of the water tank. Fig. 3.6 shows a plot of the arrival time of the signal of interest, end-effects and reflections from the transducer and water tank against the standoff distance.

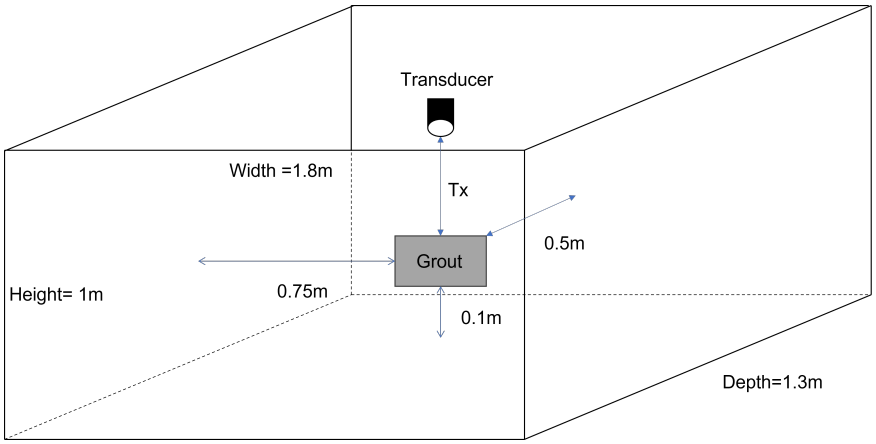

Figure 3.5: Water tank dimensions

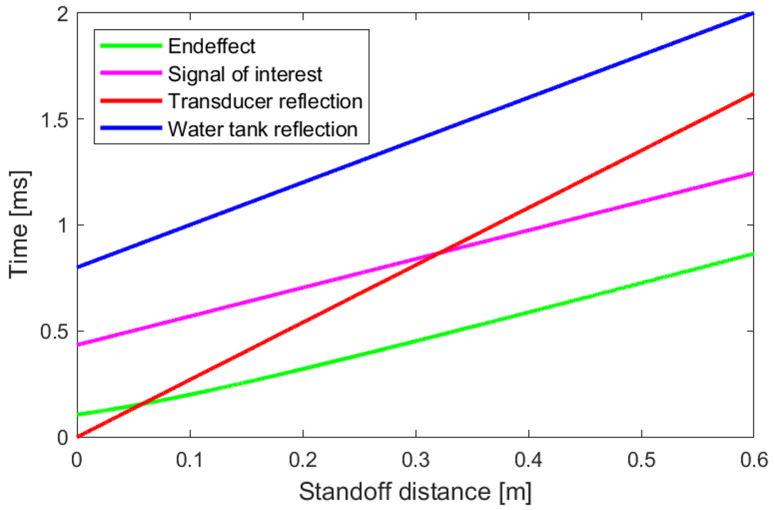

Figure 3.6: Transit time for the signal of interest, end-effects and reflections from the transducer and water tank

The signal of interest (T_i) is the time it takes for the reflected signal from the front and back interfaces of the grout, including three reverberation periods, to reach the transducer, calculated with the formula

$$T_i = \frac{2T_x}{c_w} + 4\left(2\frac{G_x}{c_{p_g}}\right) + \frac{S_L}{c_w}, \tag{3.1}$$

where T_x, G_x, c_{p_g} and S_L are the standoff distance, grout width, compressional sound ve-

locity in grout and signal length, respectively. End-effects are the pressure waves from the material's edges, as depicted in Fig. 3.4. The end-effect in focus results from the incident wave with the critical angle because it has the least transit time, as shown in Appendix E. The end-effect (T_e) is determined using the formula

$$T_e = \frac{\sqrt{T_x^2 + G_{y_1}^2}}{c_w} + \frac{\sqrt{T_x^2 + G_y^2}}{c_w} + \frac{G_{y_1}}{c_{p_g,}}, \tag{3.2}$$

where G_{y_1} is the distance from the incidence of the acoustic wave on the grout–water interface and grout edge and G_y is half the width of the grout, shown in Fig. 3.4. Furthermore, the reflection from the transducer and water tank is calculated by dividing the distance travelled by the sound velocity in the water.

Fig. 3.6 illustrates that the end-effect arrives before the signal of interest, irrespective of the standoff distance, implying that the end-effects influence the signal. To prevent reflections from the transducer and water tank from affecting the measurements, a standoff distance of 0.4 m is selected.

3.3 Transducer

The transducer used in this study was an AIRMAR B175 with a 10 m long AIRMAR C335 cable. An overview of some of the important transducer specifications is given in Table 3.2, with additional information in the datasheet in Appendix G

Table 3.2: Transducer specifications for AIRMAR B175

Transducer specifications	Value
Beamwidth (105 kHz)	13°
RVR (105 kHz)	−182 dB
TVR (105 kHz)	169 dB
FOM (105 kHz)	-13 dB
Q-factor	2

3.3.1 Frequency range

The suitability of the transducer's frequency range was assessed by examining the reflection coefficient for the grout with and without steel plates, which was calculated using the equivalent input impedance method discussed in Section 2.2.1. The analysis of the transducer's

suitability included steel plates to have a suitable transducer for further research. The analysis involved a configuration with a 0.15 m thick grout sample sandwiched between two 0.03 m thick steel plates, all immersed in an infinitely thick water layer, with each layer assumed to be infinite in length and depth, as depicted in 2D in Fig. 3.7. Fig. 3.8 presents the reflection coefficient for normal incidence (zero-degree incidence angle). The figure displays an even distribution of nodes, and within the frequency spectrum of 85 to 135 kHz, multiple nodes are evident. These nodes correspond to frequencies where the most energy is transferred into the steel and grout layers [34].

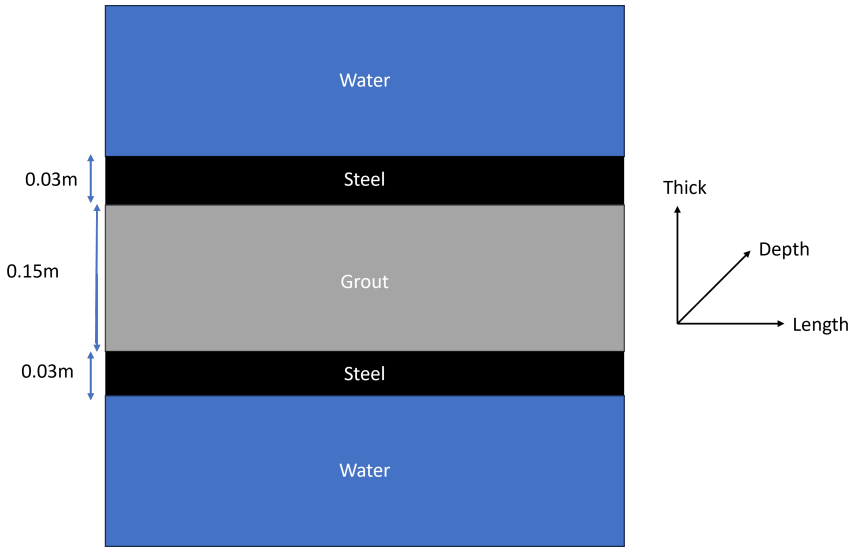

Figure 3.7: Depiction of layers used to calculate the reflection coefficient with the equivalent input impedance method

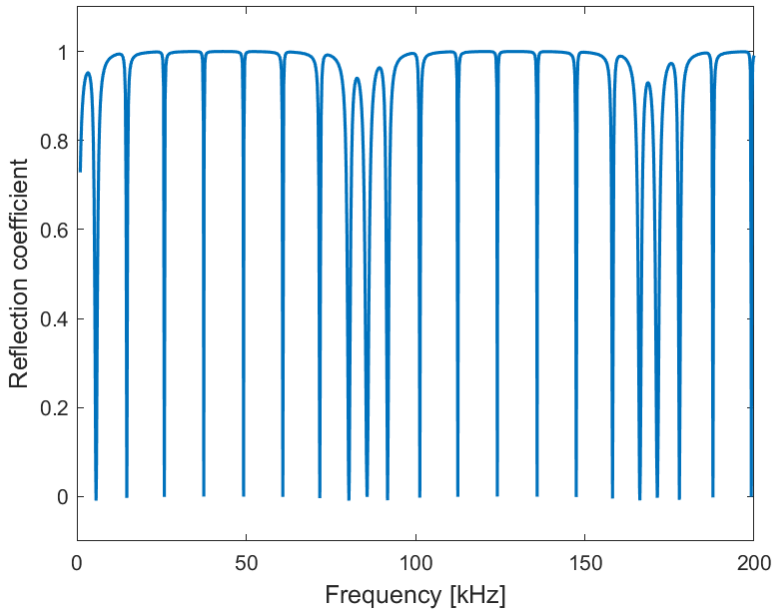

Figure 3.8: Reflection coefficient of a 0.15 m thick grout sample sandwiched between two 0.03 m thick steel plates, all immersed in an infinitely thick water layer, with each layer assumed to be infinite in length and depth. The characteristics of the grout are found in Section 3.5, and the steel's characteristics are density of 7850kg/m^3, c_p=5856m/s and c_s=3130m/s

Furthermore, the reflection coefficient was also examined for a 0.15 m thick grout sample in an infinitely thick water layer, where each layer was considered infinite in length and depth, as in Fig 3.7 without the steel plates. Fig. 3.9 illustrates the reflection coefficient for normal incidence, and similarly to the steel-covered grout scenario, the frequency spectrum of 85 to 135 kHz shows several nodes.

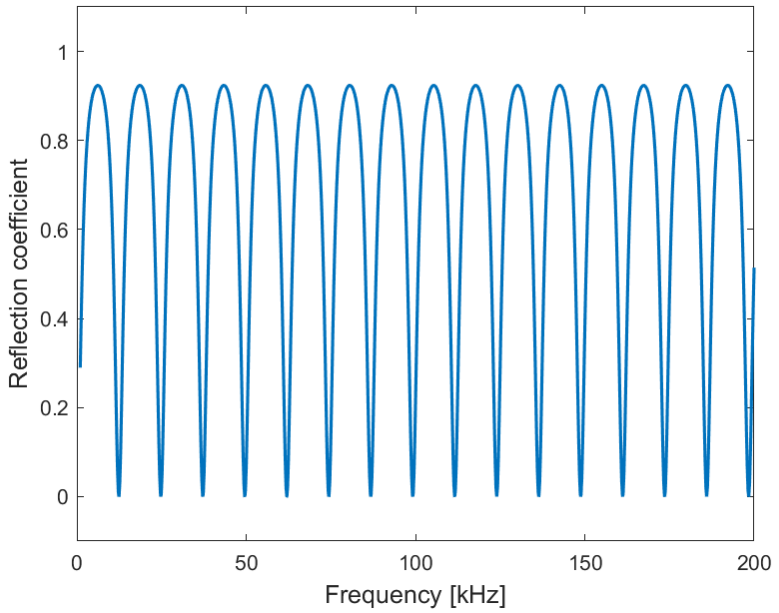

Figure 3.9: Reflection coefficient for a 0.15 m thick grout sample in an infinitely thick water layer, where each layer was considered infinite in length and depth. The characteristics of the grout are found in Section 3.5

Based on these observations, the frequency range of 85 to 135 kHz provided an acceptable bandwidth for the transducer's operation, achieving energy transfer into both the steel and grout layers.

3.3.2 Electrical impedance

The electrical impedance measurements were conducted using an OMICRON LAB Bode100 vector network analyser, as depicted in Fig. 3.10. Prior to the impedance measurements, the Bode100 was calibrated using an open, shorted and loaded circuit, as detailed in [60]. The impedance measurements were performed on the transducer with a 10 m cable attached while the transducer was placed in the water tank. The frequency resolution on the impedance measurements was 36.6 Hz.

Figure 3.10: OMICRON LAB Bode100 vector network analyser [61]

3.3.3 Beam pattern

The beam pattern of a transducer is known to exhibit frequency dependence since it relies on the wave number, which in turn is dependent on the frequency [26, 62]. The beam pattern is also influenced by the transmitting radius [62]. The transducer's dimensions are given in Appendix G, where the radius of the vibrating surface of the transducer is 95 mm and a total surface of 135 mm. The specific beam patterns for frequencies of 85, 105 and 135 kHz are provided in the transducer's datasheet, as referenced in Appendix G. The corresponding beam widths, denoted as θ_{AR}, are reported as 16°, 13° and 11° for the respective frequencies.

To calculate the footprint of the transducer, Pythagoras was employed. The beam diameter D_b at a standoff distance $z = 0.4$ m is determined using

$$D_b = z * \tan(\theta_{AR}/2) * 2. \tag{3.3}$$

Substituting the given beam width values, the beam diameters for frequencies of 85, 105 and 135 kHz are calculated as 0.1124, 0.0911 and 0.0770 m, respectively. Consequently, the corresponding beam areas are estimated to be 0.0993, 0.0065 and 0.0047 m^2, respectively.

3.4 Electronics

The electronics in the measurement setup consisted of a signal generator, amplifier, oscilloscope, transducer and receiver with cables connecting them, as shown in Fig. 3.11.

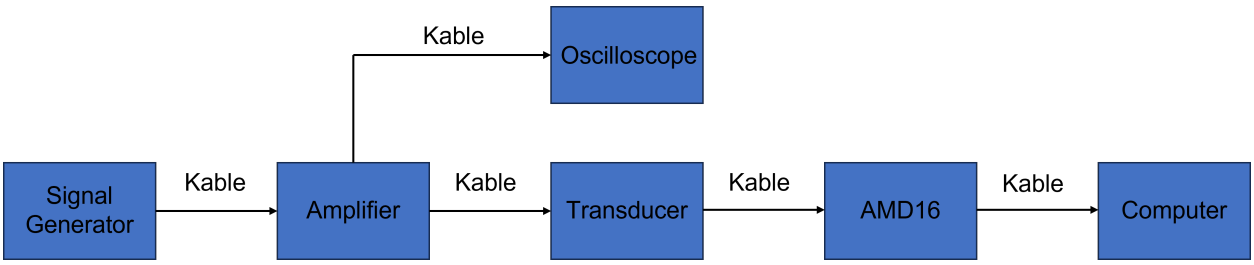

Figure 3.11: Diagram of the electronics in the measurements setup

3.4.1 Receiver and amplifier

The ADM16 receiver and PA12 amplifier were designed to handle higher frequencies than those used in this study. The ADM16 has a bandwidth ranging from 300 kHz to 3 MHz, as depicted in Fig. 3.12, showing its frequency response. The transducer's bandwidth is 85 to 135 kHz, which falls outside of the receiver's bandwidth, and no data were available in this frequency range. Operating outside the receiver's bandwidth could significantly impact the signal's frequency components, making it challenging to compare with simulated cases.

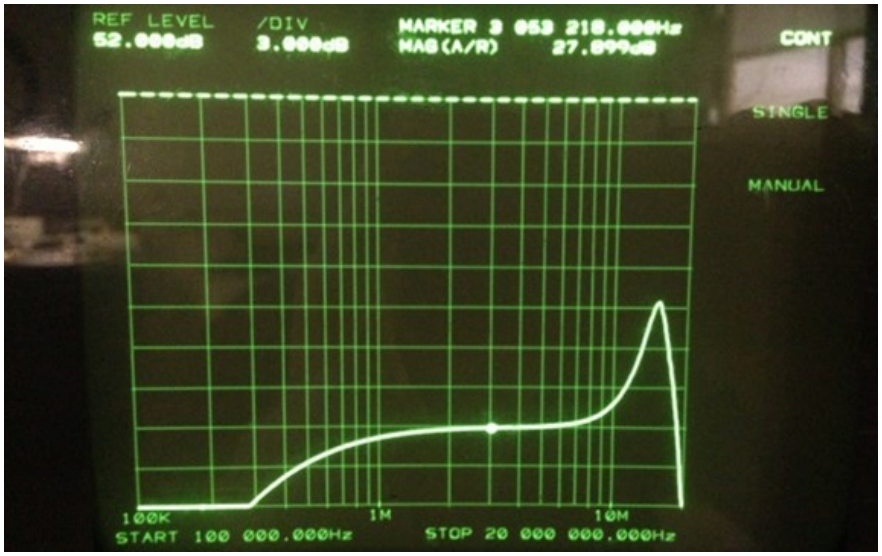

Figure 3.12: ADM16 receiver frequency response

Similarly, the PA12 amplifier is intended for the same bandwidth as the receiver, but unfortunately, no data were available regarding its frequency response. The amplifier was connected to a signal generator generating a linear chirp ranging from 60 to 140 kHz, with the amplifiers impact on the signal measured with an Oscilloscope. The effect of the amplifier on the signal's normalised amplitude is presented in Fig. 3.13 (right), while Fig. 3.13 (left) displays the frequency response. The amplifier introduces high-frequency components and distorts the signal.

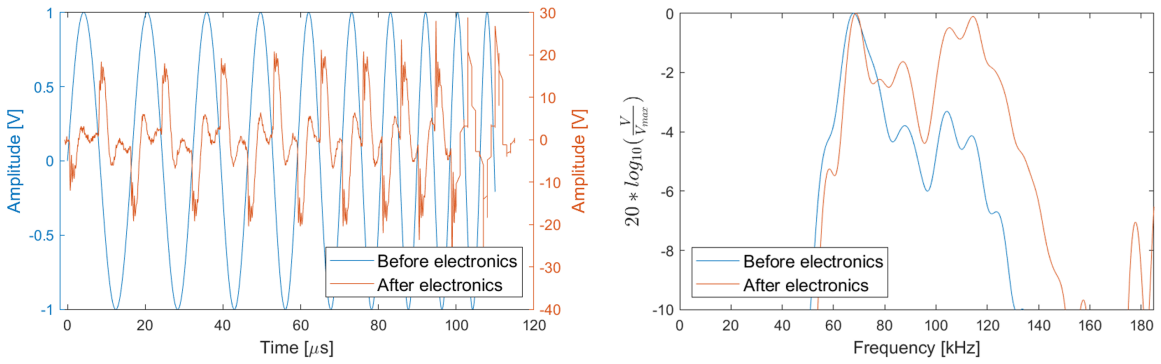

Figure 3.13: Normalised amplitude before and after electronics (signal generator–amplifier–oscilloscope) (left) and frequency response before and after electronics (signal generator–amplifier–oscilloscope) (right)

3.5 Material characteristics

The propagation of sound within a medium is greatly influenced by its material characteristics. The speed of sound in the medium plays a critical role in determining the expected travel time of a signal. Knowing the signal's travel time allows for calculating the impact of end-effects and reflections from the transducer and water tank, as demonstrated in Section 3.2. The material's density and sound velocity are vital parameters for the simulations conducted in Chapter 4 of the thesis.

3.5.1 Grout

The grout used in this study was a mix of ordinary Portland cement (OPC) and water. A pure cement and water mixture results in weak grout, which is very uncommon. In the literature, the studies used grout and cement containing sand, chemicals or gravel [63, 64, 65].

Density

The density of the grout was determined experimentally because of the unusual gout mixture, 2007 g/dm^3 in this study, which is lower than reported in studies in which the grout contained sand, gravel or chemicals. Weight and length measurements of the grout are presented in Appendix F

Size

The dimensions of the grout sample were determined based on the materials at hand for creating a mould, as well as the steel plates intended to cover the front and back of the grout specimen. The mould utilised in this investigation was crafted from a wooden frame, covered by steel panels at its front and rear, while its sides were covered by plexiglass, as illustrated in Figure 3.2. Owing to the necessity of disassembling and reassembling the mould for each sample, the sizes of the samples exhibited variations, as detailed in Appendix F.

Sound velocity

As discussed in [66, 67], the sound velocity in grout is affected by the water-to-cement ratio and the curing time of the grout. The experiments in this master's thesis were conducted with a water-to-cement ratio of 0.28. The grout's curing time significantly impacts the sound velocity but stabilises around 40 hours [66, 67]. Therefore, the grout used in the experiments had a curing time of at least two days. The pressure wave velocity used in this study was estimated to be 3700 m/s based on sources [66, 67].

The shear wave speed was determined using Poisson's ratio (2.2) [13] and was estimated based on previous research [68]. The specific dataset under examination involved cement mixtures possessing a cement–water ratio of 0.3, with varying quantities of aggregates. Of note, Poisson's ratio is influenced by the aggregate content within the mixture, where reduced amounts of aggregates lead to higher Poisson's ratios. Additionally, the hydration process of concrete also contributes to an increase in Poisson's ratio [68]. In the present study, the concrete samples utilised were devoid of aggregates and were completely hydrated, resulting in a comparatively high Poisson's ratio, estimated at 0.26 [68]. This resulted in a shear wave speed of 2331 m/s.

3.5.2 Water

Density

The density of water is influenced by temperature. For the specific testing case, the water temperature was recorded as 21°C. The density of water is determined to be 998 kg/m^3 [69]. Minor deviations from this figure are anticipated, owing to the presence of slight quantities of steel rust and grout within the water employed in the experiment.

Sound velocity

The speed of sound in water can be calculated using Equation (2.3). Equation (2.3) was subject to higher uncertainty than if applied to distilled water because of the presence of particles. The number of particles in the water was unknown, but to limit the amount of uncertainty, the tank was cleaned, and the water was changed three days before testing. The water was then left to warm to room temperature (21°C) and let the gas content reduce. The hydrostatic pressure at a depth of 0.5 m can be determined utilising Equation (2.4), yielding a hydrostatic pressure of 0.04889 Bar. The speed of sound in water at a temperature of 21°C is established to be 1485.2 m/s.

3.6 Defect

This study introduced two distinct types of void defects, namely spherical and cylindrical, with the center placed at a depth of 5 cm. The spherical defect had a radius of 2 cm, while the cylindrical defect had a radius of 3.5 cm and a height of 2.4 cm. The wavelength in the grout for 85 and 135 kHz were 0.0435 and 0.0274 m, respectively. The defects were larger than half the wavelength and were, therefore, large enough to be detected with the frequency bandwidth chosen. The voids were created using solid plastic objects filled with air. Specifically, a ping pong ball was used to form the spherical void, while a snuff box was used to create the cylindrical void. To achieve accurate positioning, the objects were securely attached using a fishing string, as illustrated in Figure 3.14.

Figure 3.14: How the cylindrical defect was made with a snuff box fastened inside the grout mould at a depth of 5 cm

3.7 Signal processing

In the experimental part, the signal underwent a series of processing steps. Initially, it was averaged over 20 samples to reduce random noise. Subsequently, a digital band-pass filter was employed, with a low cutoff frequency set at 50 kHz and a high cutoff frequency at 150 kHz, which is slightly outside of the transducer bandwidth. After this filtering operation, the reverberation portion of the signal was extracted. Then, a point close to zero was found in the start and end of the signal, which were utilised as the start and the end of the signal to avoid aliasing. After the start and end point of the reverberation was found a Hamming, Hanning or rectangular window functions was applied. These window functions shaped the signal segments before the FFT calculation, with each window providing a distinct trade-off between main lobe width and side lobe attenuation. The use of these window functions enables the frequency content of the reverberation signal to be analysed. Window functions Hamming and Hanning are plotted in Fig. 3.15 (right) together with a general signal, the effect from applying the filters are shown in Fig. 3.15 (left). After the window functions were applied, an FFT of the signal was carried out. The MATLAB code used is presented in Appendix H.

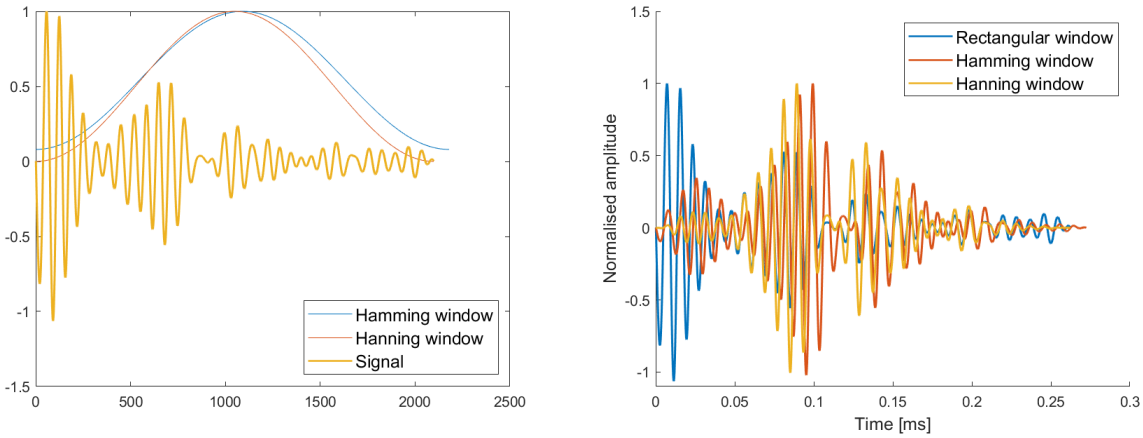

Figure 3.15: Right:Hamming and Hanning windows plotted with a general signal
Left:Result of Hamming and Hamming window applied to the signal (rectangular window)

Chapter 4

Finite Element Simulations

In this chapter, the FE method is used to simulate the reflected signal from the multilayered structure depicted in Fig. 4.1. In this chapter, the experimental setup is simulated in addition to a setup that does not include end-effects and a deformed pulse. The chosen approach involves gradually building the model and comparing the FE solution to analytical formulas from Chapter 2 at each stage. This approach was chosen to check the right implementation of the FE model as the model becomes increasingly more complex.

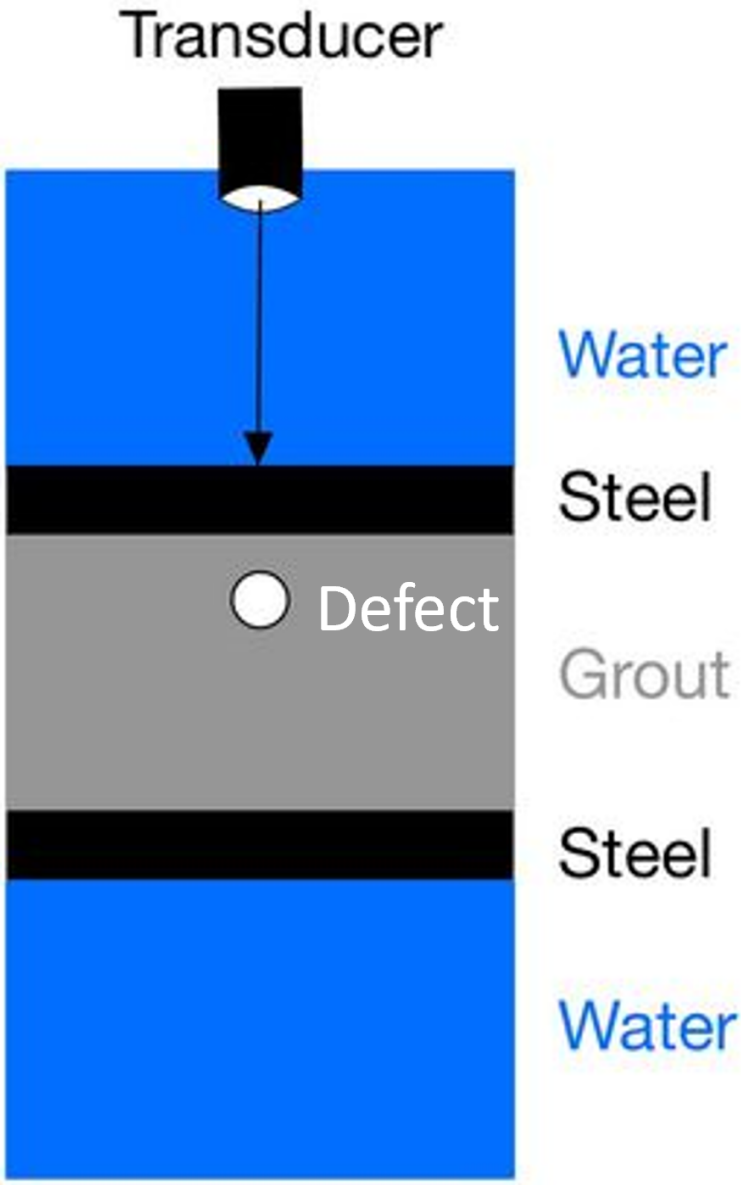

Figure 4.1: Illustration of the complete multilayered structure consisting of a transducer radiating into water, which contains steel, grout with a spherical defect and steel structure with water on the other side

The simulation tool COMSOL was chosen for the FE simulation based on the experience with the tool in the acoustics group at the University of Bergen as a capable physical acoustics simulation tool in the time domain. A baffled piston source is utilised instead of a transducer for a simpler simulation and interpretation of the signal. In this study, the construction of the multilayered structure involves several sequential steps. Firstly, a baffled piston model is created in water, as described in Section 4.1. This step analyses the incident wave and

determines the optimal meshing element size. Subsequently, a solid material is introduced into the model to examine the reflection coefficient. This was accomplished by incorporating a semi-infinite solid steel plate into the simulation, as detailed in Section 4.2. The complete multilayered model is simulated, as outlined in Section 4.3, with the experimental simulation in Section 4.4. Lastly, the simulation to determine the resonance frequencies are covered in Section 4.5

The FE models are set up utilising the 2D axisymmetric spatial dimension, where the model is axisymmetric around the z-axis [70]. Section 2.6.1 explains two ways to simulate physics in the time domain. In COMSOL, the time-implicit and -explicit physics modules are *Pressure Acoustics, Transient* and *Pressure Acoustics, Time Explicit* modules, respectively [42]. In Section 4.1.2, the *Pressure Acoustics, Time Explicit* module and *Pressure Acoustics, Transient* module with different meshing are utilised, and their solutions are compared to analytical axial pressure from Section 2.4.

4.1 Piston radiating into infinite water medium

This section covers the initial model, which consists of a baffled circular plane piston that transmits into an infinite water medium, as described in Section 2.4. The geometry of the model consists of one-fourth of a circle with a two-wavelength–thick layer, as depicted in Fig. 4.2. The parameters utilised in the model are presented in Table 4.1.

The piston is modelled using a normal velocity boundary condition for a line at $z = 0$ from $r = 0$ to $r = a$, where a is the radius of the piston. A *Sound Hard Boundary* condition is applied to the boundary along the r-axis, except for the piston segment, to simulate the presence of a baffle. Additionally, to minimise reflections at the outer boundary of the circular shape, an impedance condition is applied. No boundary is applied to the z-axis as the model is axisymmetric around the z-axis. The material water is implemented into the model, where the parameters of the water is changed to match with the material characteristics in Section 3.5.

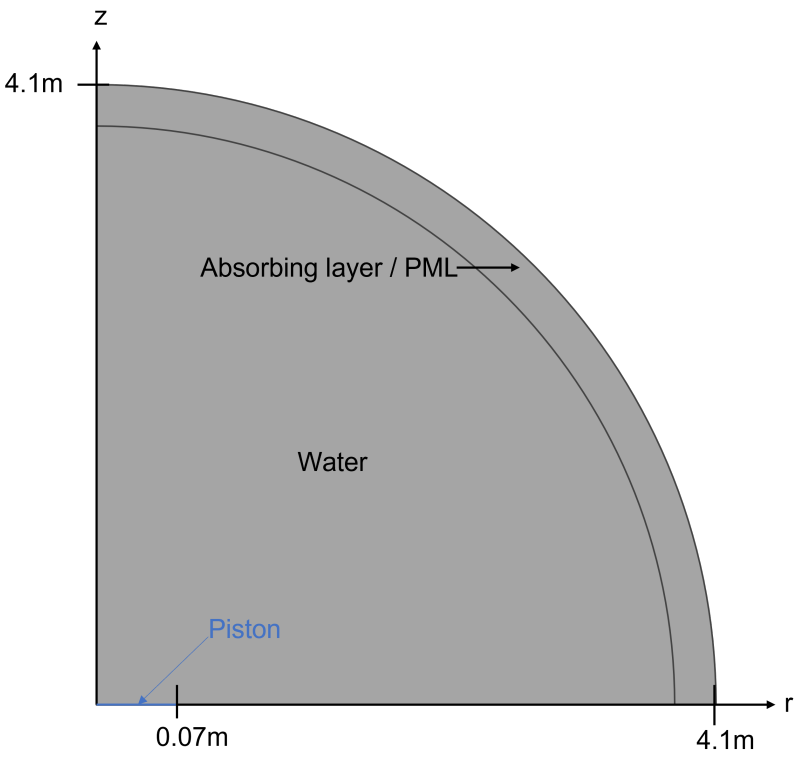

Figure 4.2: Overall configuration of the baffled piston model. The market part in the lower left corner is the piston. The outer layer is an *Absorption Layer*.

Table 4.1: Input parameters

U_0	1 m/s	Piston velocity amplitude
c_0	1481 m/s	Sound velocity in water
f_0	50 kHz	The piston's frequency
λ_0	0.02962 m	Wavelength at f_0
a	0.07 m	Piston radius

4.1.1 Creating an infinite medium

To enable the simulation of an infinite medium, an *Absorbing Layer* or *Perfectly Matched Layer* (PML) can be applied to the outer layer of the circular shape, as depicted in Figure 4.2 [42]. However, a PML is not implemented in the time-explicit solid model, while the *Absorbing Layer* is not implemented in the time-implicit model.

The *PML*, a widely used technique for creating an infinite medium, sets up a perfectly

absorbing domain [42]. To minimise reflections, the geometrical thickness of the layer must be adequate. Since *PML* lacks a real stretching component in the time domain, the layer's thickness should have at least eight meshing elements for the lowest frequency component [42].

The *Absorbing Layer* slows down the propagating wave in a highly attenuating layer, resulting in a non-reflecting layer [42]. The thickness of the *Absorbing Layer* has to be equal to or greater than three meshing elements or one wavelength for the lowest frequency component to ensure a non-reflecting boundary [42].

The *Absorbing Layer* and *PML* have the same purpose of producing a simulated infinite medium [42]. The time-implicit and -explicit models use the *PML* and *Absorption Layer*, respectively [42].

4.1.2 Meshing

The element size and degree of the mesh substantially impact computational cost and the accuracy of the simulation [71]. Therefore, determining the largest possible element size with the lowest degree that does not significantly hinder simulation accuracy is essential. This study evaluated linear, quadratic and quartic meshing elements for the *Pressure Acoustics Transient* module. In addition, the *Pressure Acoustics Time, Explicit* module was assessed with quartic meshing elements.

In the *Pressure Acoustics, Time Explicit* module, the triangular elements and for the *Pressure Acoustics Transient* module are implemented, except in the PML, where mapping elements are utilised [72]. Parameters other than element size are also considered when building a mesh. However, in the baffled piston model, *maximum element growth rate*, *curvature factor* and *resolution of narrow regions* are irrelevant because the baffled piston has uniform meshing in the model [72].

The magnitude of the acoustic pressure on the sound axis in the far field is analysed using Equation 2.28 and simulated to determine an adequate physics module, element meshing size and the degree of the elements. The maximum percentage deviation between the analytical and simulated acoustic pressure on the sound axis was determined by dividing the deviation by the maximum magnitude obtained from the analytical Equation 2.28. The

simulated sound pressure was interpolated within COMSOL with a resolution of 1/3 mm.

Table 4.2 provides the maximum percentage deviation. Linear elements have a high computational cost compared to the accuracy, so testing was limited to 20 elements per wavelength before determining its inadequacy. The quadratic and quartic elements within the *Pressure Acoustics, Transient* and *Pressure Acoustics, Time Explicit* modules are promising alternatives. However, the *Pressure Acoustics, Time Explicit* module has the highest accuracy with the lowest computational cost and is, therefore, utilised in all compatible simulations. The far-field magnitude of the acoustic pressure for the analytical Equation 2.28 and *Pressure Acoustics Time, Explicit* module is shown in Fig. 4.3

Table 4.2: Deviation between the analytical and simulated baffled piston model for different physics modules and meshing element order

Physics module	Meshing element order	Elements per wavelength	Deviation
Pressure Acoustics, Transient	Linear	18	9.6%
Pressure Acoustics, Transient	Linear	20	7.2%
Pressure Acoustics, Transient	Quadratic	8	2%
Pressure Acoustics, Transient	Quadratic	10	2%
Pressure Acoustics, Transient	Quartic	2	2.3%
Pressure Acoustics, Transient	Quartic	4	2.1%
Pressure Acoustics, Time Explicit	Quartic	2	4.4%
Pressure Acoustics, Time Explicit	Quartic	4	1.4%

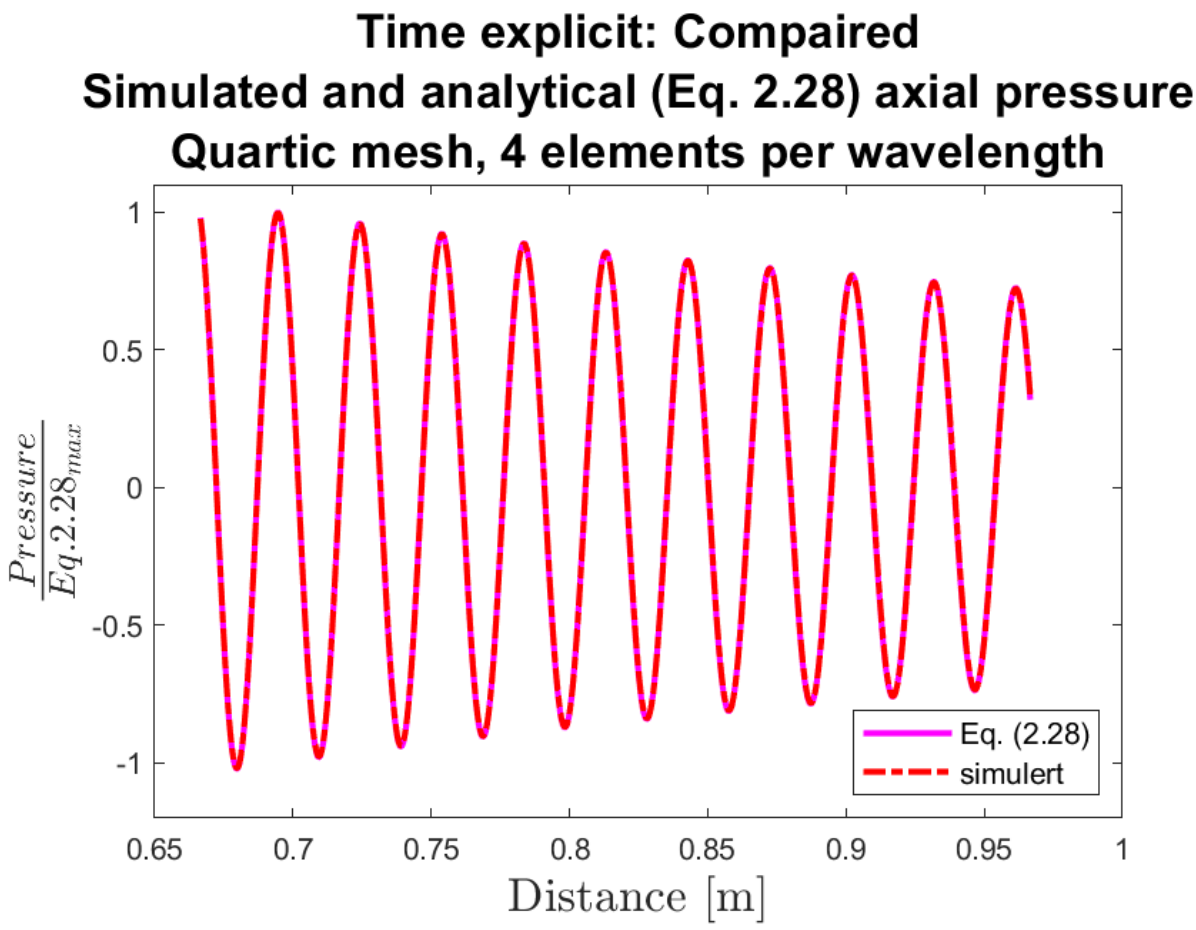

Figure 4.3: Compared simulated and analytical (Equation 2.28) acoustic pressure on the sound axis divided by the maximum value of Equation 2.28. *Pressure acoustics, time explicit* module with a mesh of four quartic elements per wavelength ($\lambda/4$) is simulated.

4.1.3 Time resolution

Another essential parameter determining the simulation's accuracy is the time resolution. One method for determining the time resolution uses the Courant number [73], a measure of the propagation of information, in this case, a pressure wave, over a given time interval [73]. The formula for the Courant number is given in the following formula [73]:

$$C = c\frac{\Delta t}{h}, \tag{4.1}$$

where c is the sound velocity, Δt is the time step, h is the element size of the mesh and C is the Courant number. A Courant number below 0.7 indicates an acceptable time resolution

for utilising all the meshing element nodes [73]. If the Courant number exceeds one, some meshing elements will be unused, implying that the finer mesh results in higher computational costs but not higher accuracy [73]. The time step used is $3.03 \cdot 10^{-7}$ s with an element size of 0.0029 m, resulting in an acceptable Courant number for materials with a sound velocity of less than 7000 m/s.

4.1.4 Input signal

The inward velocity [42], an input for the piston, should include a transient component with a start amplitude of zero that gradually ramps up to a constant amplitude rather than abruptly shifting from still to maximum amplitude. Otherwise, unintended changes to the pulse occur, as discussed with COMSOL support in Appendix I.

A notable effect becomes apparent upon plotting the acoustic pressure at the centre of the piston and comparing it to the inward velocity, as shown on the left in Fig. 4.4. The transient part of the pulse appears to be extended. The effect on the pulse changes with the piston's radius and the pulse's frequency. It also dissipates with distance to the piston, as shown on the right in Fig. 4.4. Therefore, this is caused by the end-effects of the piston and does not influence the results in this report, as the simulations are performed in the far field.

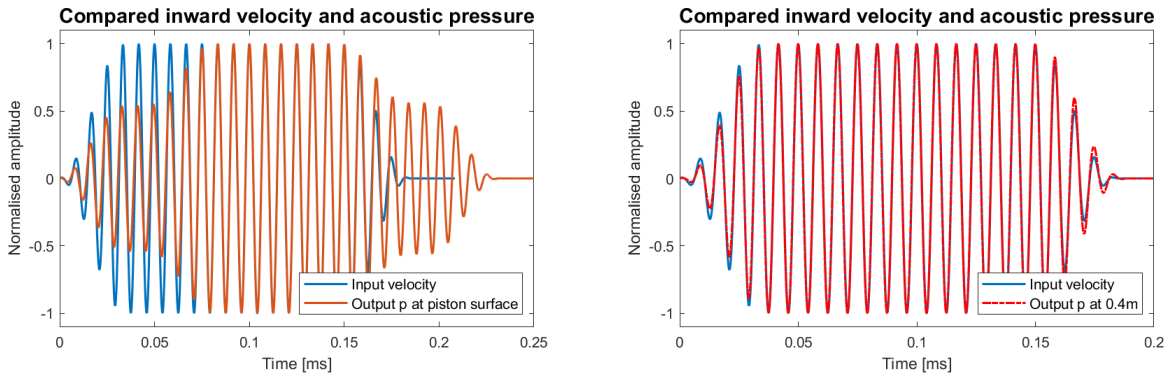

Figure 4.4: Normalised amplitude input piston inward velocity and acoustic pressure on-piston (left) and far-field (right)

4.1.5 Implementation check

To confirm the correct implementation of the simulated baffled piston model, it is compared to the analytical models in Section 2.4. Equations 2.27 and 2.31 determine the axial pressure and beam pattern in the far field, respectively.

The methodology for determining the far-field beam pattern involves an analysis of the data obtained at various distances from the centre of the piston, with an angular resolution of 0.0045°. The data is processed to find a 30 period–long stationary signal at each point. Subsequently, a fast Fourier transform (FFT) is applied to convert the signals to the frequency domain. The focus in the frequency domain is the magnitude of the input frequency component for different angles, which is the relevant value when characterising the far-field beam pattern. The results of the analysis are presented in a polar plot format, with the magnitude plotted as a function of the angle, as depicted in Fig. 4.5. The MATLAB code utilised for the signal processing and plotting is provided in Appendix B.

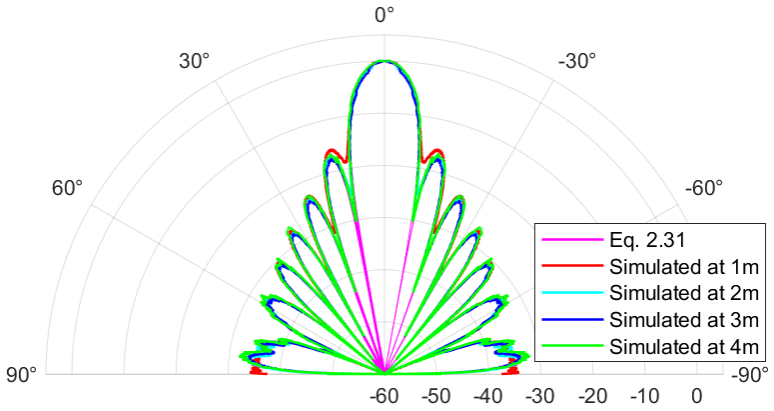

Figure 4.5: Beam pattern for different radii compared to analytical model

The simulated beam pattern converges towards the analytical beam pattern when the distance from the piston increases, as depicted in Fig. 4.5. In addition, Fig. 4.3 shows a high

degree of correspondence between the simulated and analytical (Equation 2.28) axial pressure. These factors confirm the correct implementation of the COMSOL model for a baffled piston.

4.2 Implementing a semi-infinite solid material

From this point, cylindrical models are employed instead of spherical ones, as the investigation into the beam pattern and sound pressure for higher angles relative to the sound axis is complete. This alteration does not impact the simulation outcomes since the absorbing layer emulates an infinite medium. The only difference is that the simulated area is reduced. To design a cylindrical model in a 2D axisymmetric model, rectangles are utilised.

The design of the baffled piston model featuring a semi-infinite steel plate consists of a piston and two rectangles with layers two wavelengths wide on the outer edges, as depicted in Fig. 4.6. The material for the first rectangle is water, while the second material is steel, both surrounded by absorbing layers to simulate a semi-infinite medium. The simulated model is compared to the analytical reflection coefficient explained in Section 2.2 to confirm the model's implementation.

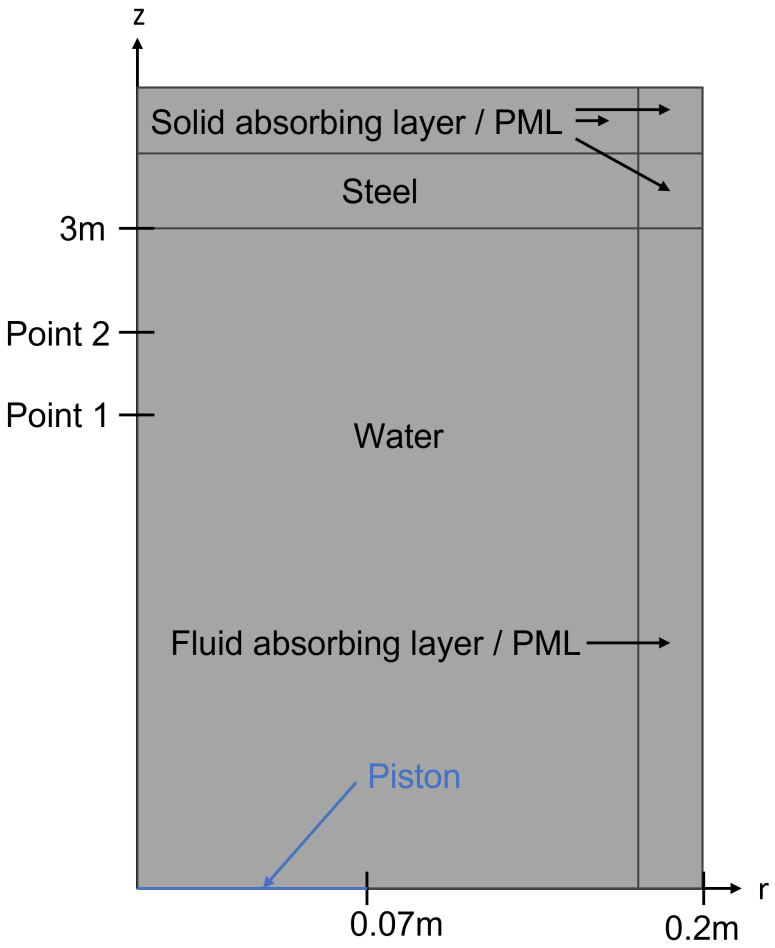

Figure 4.6: Overall configuration of the baffled piston model with a semi-infinite steel boundary.

4.2.1 Model setup

Building the baffled piston model featuring the semi-infinite steel plate is primarily covered in Section 4.1, modified from a circular to a rectangular shape, with the size parameters presented in table 4.3. This subsection discusses the corresponding differences and additions.

Table 4.3: Parameters for the size of baffled simple piston model with steel plate

Model length	3.2 m
Model width	0.2 m
Steel length	0.2 m
Water length	3 m

The guidelines outlined in Section 4.1 are initially applied during the model's creation, albeit with a rectangular outline instead of circular. Upon completing the steps in Section 4.1, an additional rectangle is implemented onto the initial structure, as illustrated in Fig. 4.6. Both rectangles should feature an outer layer two wavelengths thick, corresponding to the material with the longest wavelength, specifically for steel in this context. An *Absorption layer* is applied to the outer layer of the rectangles. The recently incorporated rectangle's material should be steel and subject to the *Elastic Waves Time Explicit* physics module. The steel's characteristics should be a density of 7850 kg/m^3, compressional sound velocity of 5856 m/s and shear velocity of 3130 m/s. The steel and water domains are marked as different *Unions*, with a *Form Assembly* with automatic creation of pairs between the unions. To couple the physics, the *Multiphysics, Pair Acoustics-Structure Boundary* coupling is added to the automatically created pairs.

Regarding mesh creation, triangular elements, similar to those outlined in Section 4.1.2, are adopted. The meshing for both the steel and water domains mirrors the procedure explained in Section 4.1.2. However, distinct element sizes are utilised, based on the respective wavelengths. Triangular elements of varying proportions are assigned to the steel and water regions, resulting in a discontinuous mesh configuration, producing optimal results [74], as depicted in Fig. 4.7.

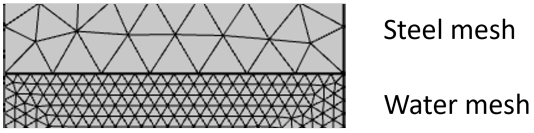

Figure 4.7: Transition between water mesh and steel mesh

4.2.2 Implementation check

To verify the correct implementation of the model, the simulated reflection coefficient is compared to the equivalent input impedance method covered in Subsection 2.2.1. The incident and reflected pressure waves are measured at a distance from the water–steel interface, depicted as point 2 (P2), in Fig. 4.6. The pulse length is 21 periods, corresponding to 0.32 m, to obtain a stationary part of the pulse. As a result, the measurements have to be taken at a distance of at least 0.16 m from the source to avoid interference between the incident and reflected waves. The pressure waves are corrected to correspond to the acoustic pressure

at the interface using the formula:

$$p(P2) = \frac{p(P1)}{r \cdot e^{i(-kr)}}, \tag{4.2}$$

which is only valid in the far field, and therefore, the steel plate has to be placed in the far field of the piston.

To confirm the validity of the geometric correction of the incident and reflected signals, the stationary part of the acoustic pressure waves is corrected to a point with measured amplitude. The incidence wave acoustic pressure in point one (P1) is corrected with geometric spreading to P2. Fig. 4.8 show the magnitude of the pressure wave at P1 and the pressure wave at P1 with geometric correction to P2 compared to the simulated pressure at P2. The MATLAB code is showed in Appendix C.

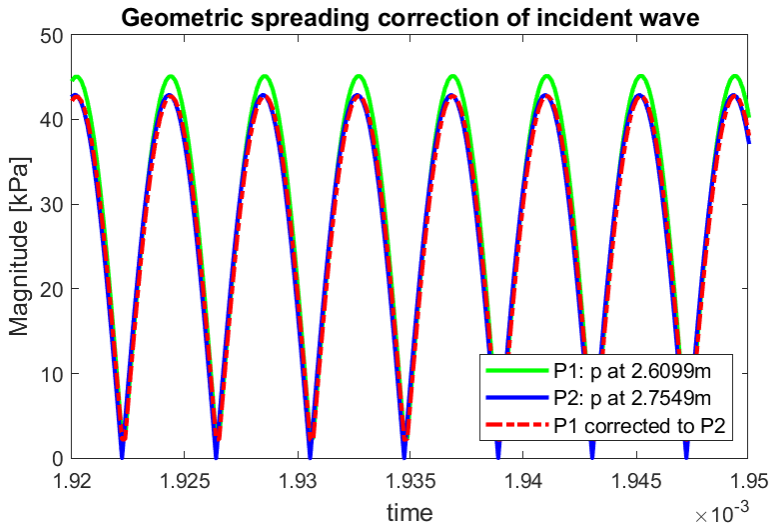

Figure 4.8: Comparing the simulated pressure wave at P1 corrected with geometric spreading to P2 and the simulated pressure wave at P2

The simulated reflection coefficient is found using an FFT on the stationary part of the incident and reflected pulses and applying the input frequency component f_0 from Table 4.1. The analytical (Equation 2.11) and simulated reflection coefficients are 0.9366 and 0.9430, respectively, which correspond well, with a difference of 0.0064, confirming the correct implementation of the model.

4.3 Building the full model

The complete model consists of a semi-infinite 15 cm wide grout sample with and without defects placed between semi-infinite water. The model comprises of three rectangles, with layers two wavelengths wide on the outer edges, as illustrated in Fig. 4.9. The first and last rectangles represent water, while the middle rectangle is the grout. The grouts characteristics are the same as in Section 3.5. The defect is added to the grout by creating a shape with the defect subtracted from the grout rectangle, as shown in Fig. 4.10 (left). The defect is then added as a separate geometry representing air, as shown in Fig. 4.10 (right). The air's characteristics is a density of 1.2 kg/m^3 and a sound velocity of 343 m/s.

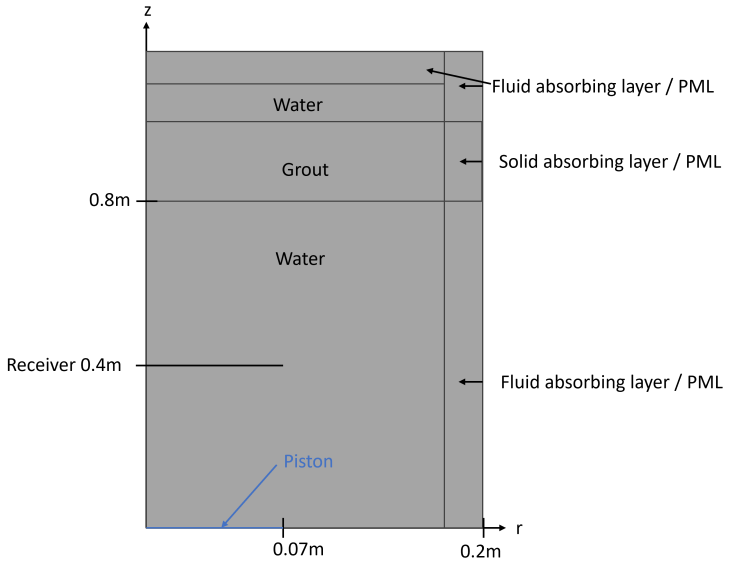

Figure 4.9: Complete model of semi-infinite grout without a defect placed in semi-infinite water.

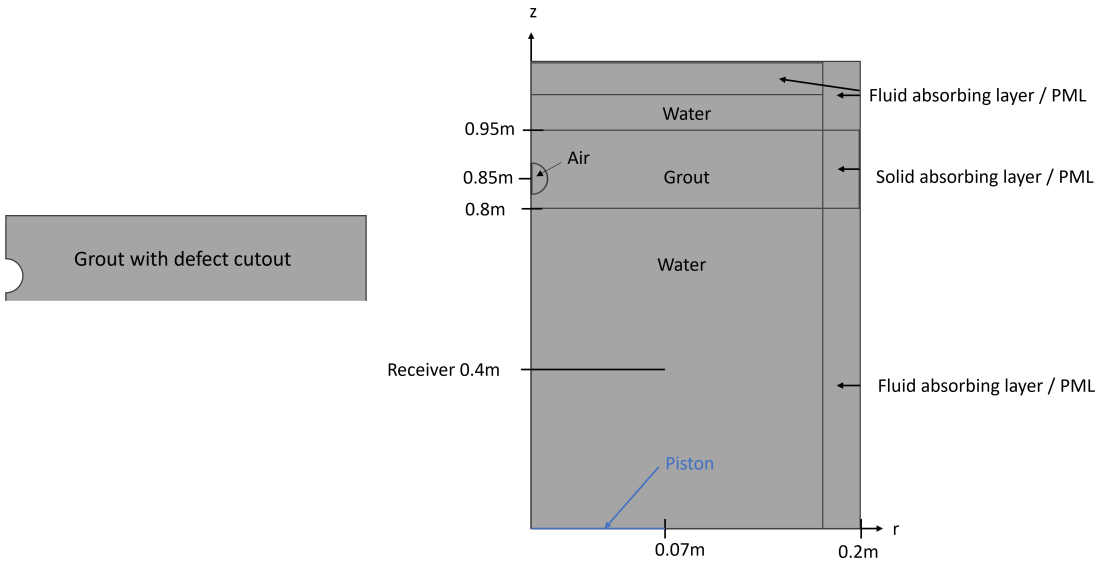

Figure 4.10: Grout with the cylindrical defect subtracted (left) and the complete model of semi-infinite grout with a cylindrical defect placed in semi-infinite water (right)

To create the model, the steps detailed in Sections 4.1 and 4.2 are followed, albeit with the replacement of steel with grout and the omission of the *Absorption Layer* on the top of the second rectangle. The size parameters of the model is presented in Table 4.4. The second rectangle can be with or without a defect, as depicted in Figures 4.10 and 4.9. Once the preceding steps have been carried out, the final rectangle is integrated onto the initial structure. This rectangle represents water and is implemented in a manner similar to that in Section 4.1, except with an *Absorption Layer* not only on the side but also on the top.

Table 4.4: Size parameters for the full simulated model

Model length	3.2 m
Model width	0.2 m
Grout length	0.15 m
First water length	0.8 m
Second water length	0.1 m

The initial inward velocity input is replaced with a chirp spanning from 60kHz to 140kHz, as illustrated in Figure 4.11. This adjustment aims to incorporate multiple frequency components within the pulse, aligning with the approach applied to the pulse before the electronic stage discussed in Section 3.4.

As previously, a *Union* operation is applied to the different materials. The only difference from Section 4.2 is that the water is divided into two distinct *Unions*, positioned in front of

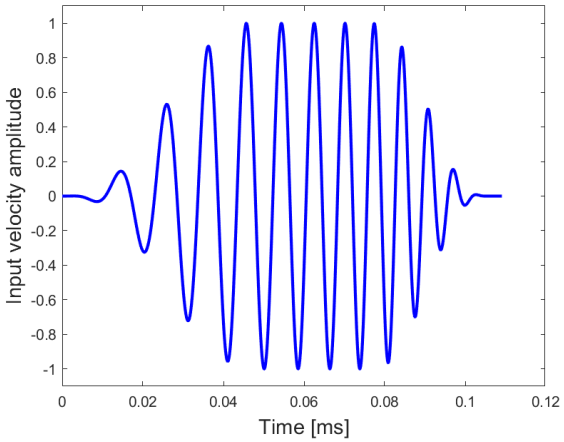

Figure 4.11: Input inward velocity pulse for the simulations

and behind the grout. The process of coupling physics and meshing remains consistent with the description in Section 4.2.

The time-explicit model employed so far need to be substituted with a time-implicit model. The time-explicit model proved unstable and yielded unrealistic results upon the introduction of damping. Instances of unstable simulations are more common in time-explicit modules within COMSOL than in time-implicit models. The response from COMSOL support is documented in Appendix I.

The time-implicit model closely resembles the time-explicit model, with the implementation of *Pressure Acoustics Transient* and *Solid Mechanics* physics modules instead of *Pressure Acoustics Time, Explicit* and *Elastic Wave, Time Explicit*, respectively. The absorbing layer is replaced with a PML. The primary distinction between the time-implicit and explicit modules lies in the meshing and the physics coupling.

The most efficient meshing is achieved with quadratic elements for the time-implicit module. A size of nine elements per wavelength synchronises the meshing resolution, resulting in equal distances between nodes. The *Form Assembly* is replaced with *Form Union*, which does not have automatic pair creation. Therefore, the physics is coupled using the *Multiphysics, Acoustics-Structure Boundary*, where the coupling is applied manually to the solid–fluid and fluid–solid interfaces.

The time-implicit and -explicit models are compared for a compressed version of the exper-

iment, as shown in Fig. 4.12 (left). Fig. 4.12 (right). The figure compares the time-explicit and -implicit sound pressure at 0.05 m, demonstrating satisfactory agreement between the two. As a result, the time-implicit module is employed for the remainder of the study.

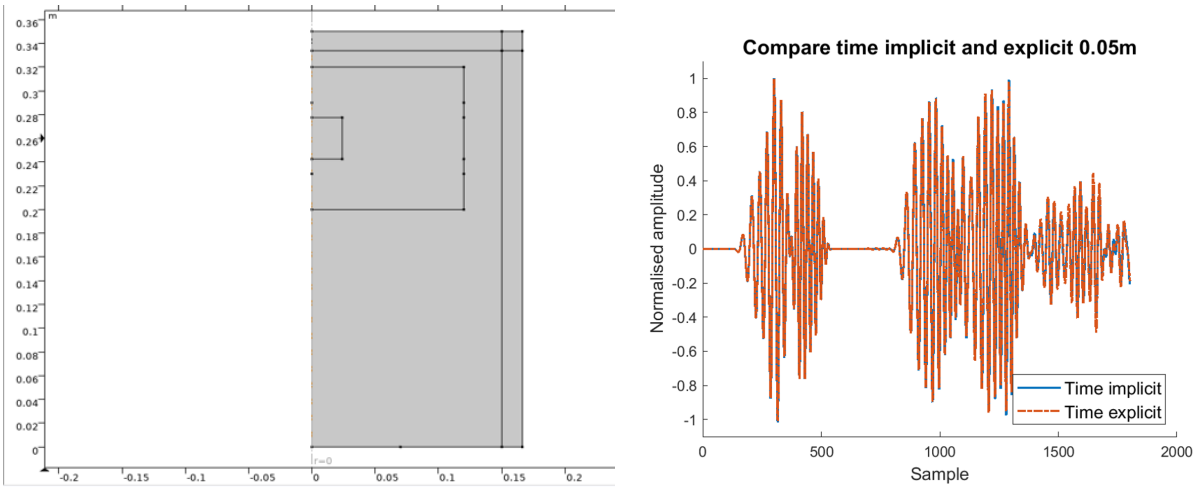

Figure 4.12: Compressed simulation model (left) and a comparison of time implicit and time explicit physics modules at 0.05 m (right)

4.3.1 Damping

In this study, we assume that the damping in the water and air has minimal impact on the results, and thus, it is only applied to the grout. The Rayleigh damping model is utilised for this purpose, as discussed in Section 2.9. To prevent the model's damping from inadvertently affecting the results, minimal damping is implemented and compared to the undamped model. The dampening parameters α and β are set to 2.120 and $1.787 \cdot 10^{-10}$, respectively, equivalent to approximately 0.1 dB/m. The undamped and damped versions are compared in Fig. 4.13.

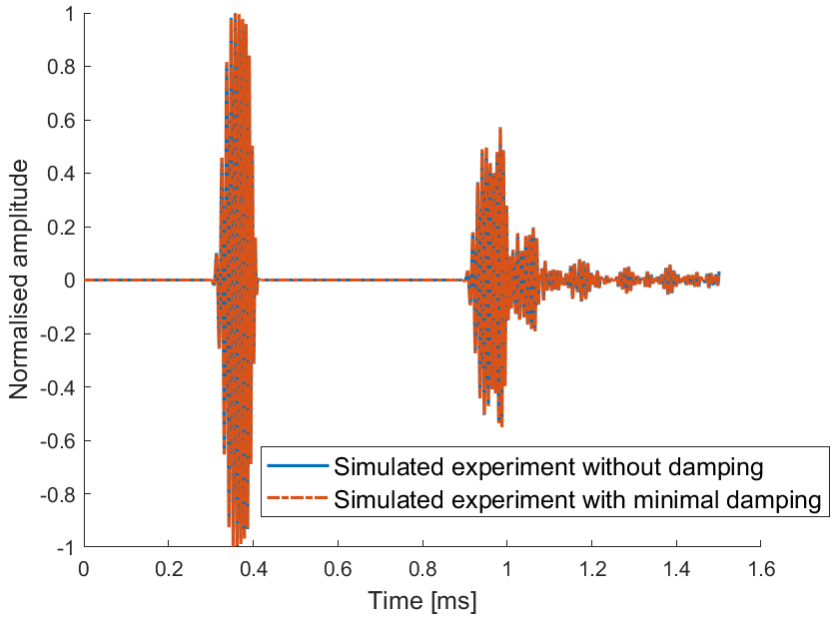

Figure 4.13: Simulation of the experiment without dampening and with minimal dampening of approximately 0.1 dB/m ($\alpha = 2.120$ and $\beta = 1.787 \cdot 10^{-10}$)

The damping in cement products is influenced by the water-to-cement ratio and aggregates [51, 52, 75]. The existing literature [51, 52, 75] indicates that the damping typically ranges from 100 to 200 dB/m, leading to minimal reverberation, as demonstrated in Fig. 4.14, which deviates from the experimental results. Notably, the damping in the literature corresponds to cement products with added aggregates, which enhances the damping effect. Therefore, the amount of damping is determined by comparing the reverberation observed in the experiment with a simulation.

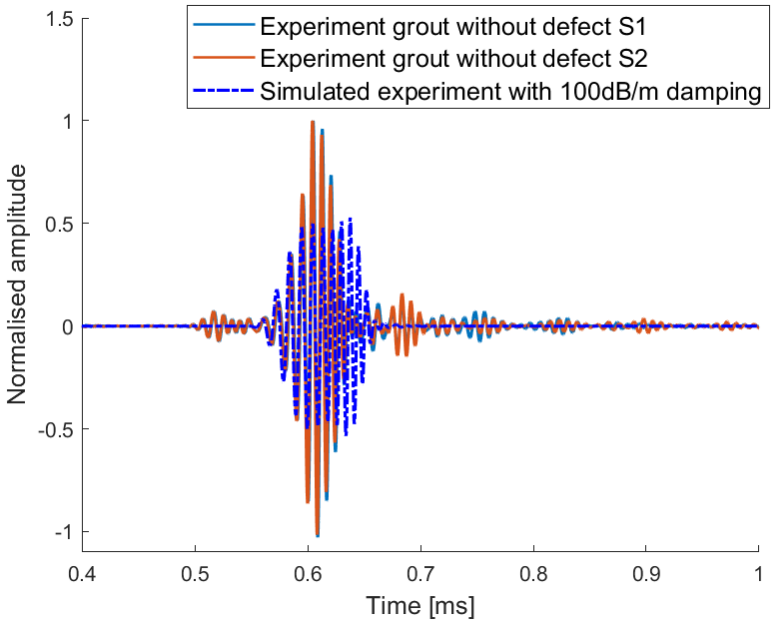

Figure 4.14: Reverberation of the experiment and a simulation of the experiment with Rayleigh dampening coefficients $\alpha = 2120$ and $\beta = 1.787 \cdot 10^{-7}$, which corresponds to a dampening of around 100 dB/m

The Rayleigh damping coefficients $\alpha = 212.004$ and $\beta = 1.787e^{-8}$ yield a comparative reverberation between the experimental and simulated results, as shown in Fig. 4.15 (left). The corresponding damping coefficient in dB/m is calculated using Equation (2.51), as illustrated in Fig. 4.15 (right).

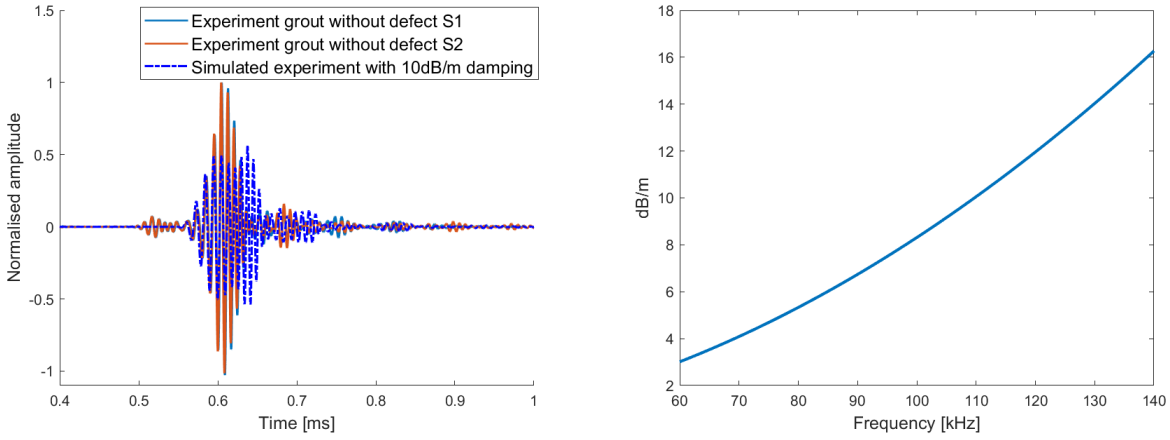

Figure 4.15: Experimental and simulated reverberation with Rayleigh dampening coefficients $\alpha = 212.004$ and $\beta = 1.787e^{-8}$ (left) and corresponding dB/m for Rayleigh dampening coefficient α=xx and β=xx (right)

4.3.2 Building the full model with steel plates

The incorporation of steel plates into the model involves introducing a rectangle either in front of or in front of and behind the second rectangle symbolising the grout. The material assigned to these additional rectangles is steel, possessing the same characteristics as detailed in Section 4.2. The process of meshing and coupling physics follows the methodology established in previous sections.

4.4 Simulation of the experiment

Building the baffled piston model resembling the experiment is primarily covered in Section 4.3, albeit with a grout rectangle of final length and width. Since the 2D-asymmetric model is utilised, the grout takes on a cylindrical form rather than a rectangular one as in the actual experiment. The decision not to transition to a 3D simulation model for simulating a rectangular grout was taken due to the significant increase in computational cost.

During the construction of the baffled piston model to match the experimental setup, the steps outlined in Section 4.3 are followed. Once the tasks in Section 4.3 are completed, the second rectangle symbolising the grout is shortened to a length of 0.15m in the r-direction, and the *Absorption Layer* is removed, as illustrated in Figure 4.16. As before, the *Multiphysics, Acoustic-Structure Boundary* feature is employed at the new solid-fluid interface.

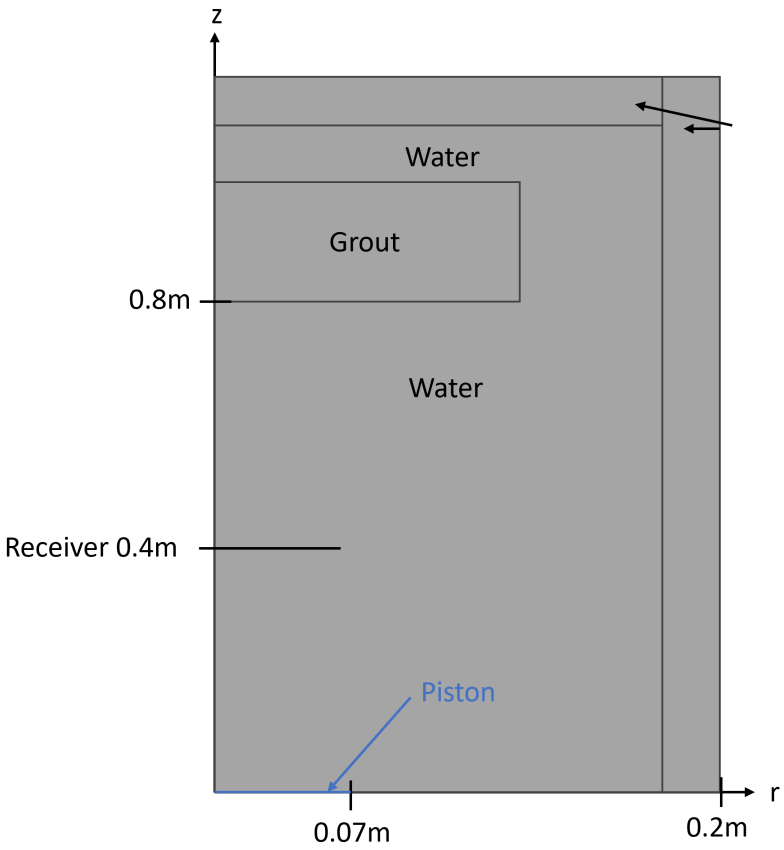

Figure 4.16: The complete baffled piston model resembling the experiment without defects in the grout.

Subsequent to the modifications to the second rectangle, a fourth rectangle is introduced adjacent to the second one. This fourth rectangle occupies the vacant space left by the shortened second rectangle. The *Absorption Layer* is reinstated along the right edge of the fourth rectangle, with *Ignore Edges* being applied to the internal edges within the water.

4.5 Resonance frequencies

To determine the coupled resonances explained in Section 2.8, simulations of the rectangular grout, cylindrical grout, and cylindrical defect are carried out. The resonant frequency simulations are performed in a 3D environment, allowing for the representation of various geometries. The study of resonant frequencies takes place within the frequency domain, with the fluid governed by *Pressure Acoustics, Frequency domain*, and the solids by *Solid Mechanics, Frequency domain*, utilising the *Eigenfrequency* study.

Resonant frequencies for the rectangular and cylindrical grout are investigated under vacuum conditions. The geometry of a cube or cylinder is chosen to represent the rectangular or cylindrical grout, using concrete material with the same characteristics as described in Section 3.5. The grout cube or cylinder is then enveloped by a larger cube, where the properties of a perfect vacuum are applied. Meshing is conducted following the same approach as in previous sections.

The analysis of resonant frequencies for the cylindrical defect is carried out with rigid walls. The cylinder geometry is equipped with a *Sound Hard Boundary* applied along its edges. The material used for the cylinder is air, possessing the same characteristics as outlined in Section 4.3. Meshing is performed following the same methodology as in preceding sections.

The Eigenfrequency study for the rectangular and cylindrical grout and cylindrical defect resulted in resonant frequencies every 10-100 Hz, which is not useful unless the most important resonant frequencies can be determined. Determining the most important resonant frequencies is not attempted in this study.

Chapter 5

Results and discussion

In this chapter, the outcomes of the experiments and simulations are presented, analysed, and compared. in Section 5.1 the electrical impedance results for the transducer are presented, with Section 5.2 covering the presentation and discussion of the experimental findings of the grout samples. The results for grout samples without defects, cylindrical defects, and spherical defects are presented in Section 5.2.1, Section 5.2.2, and Section 5.2.3 respectively. A comparative analysis of the samples is presented in Section 5.2.4.

Section 5.3 presents, discusses, and compares the outcomes from the simulations. The simulations conducted without end-effects are outlined in Section 5.3.1, while the simulations resembling the experimental setup are presented in Section 5.3.2. Finally, the simulations resembling the experimental conditions are compared with the experimental results in Section 5.4.

5.1 Electrical impedance

The impedance measurement of the transducer is presented in Fig. 5.1, where the dashed green and orange lines denote the upper and lower transducer bandwidth frequencies of 85 and 135 kHz, respectively.

Within the specified bandwidth of the transducer, the impedance remains within a 3 dB range. The datasheet for the transducer can be found in Appendix G. However, beyond

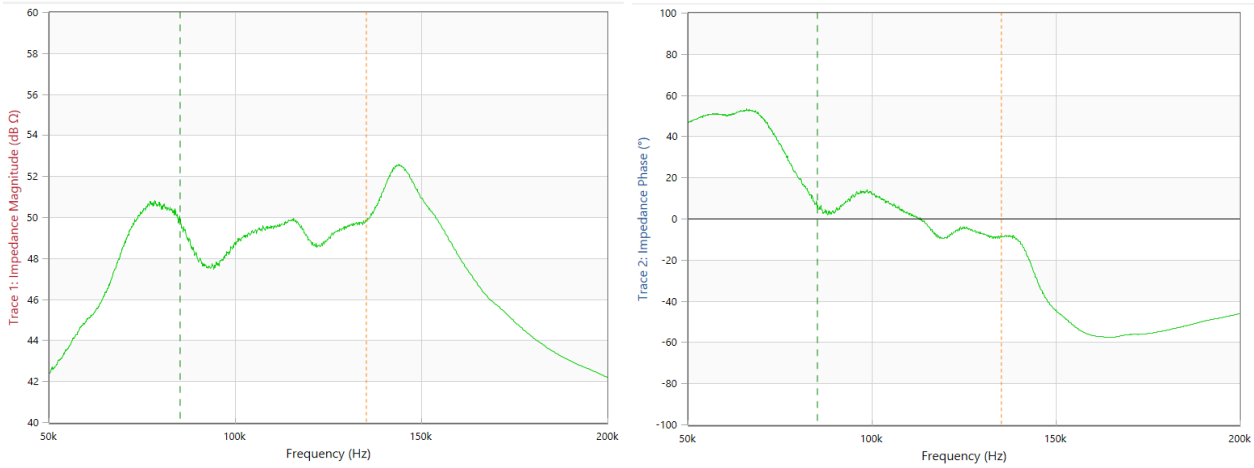

Figure 5.1: Impedance measurement of the AIRMAR B175M transducer with impedance magnitude (left) and impedance phase (right)

this bandwidth, the impedance does not deviate substantially before 25 kHz outside the bandwidth, indicating that operating the transducer outside of its bandwidth is possible to an extent.

The electrical impedance of the transducer can be utilised to determine its Q-factor employing Equation (2.37). The resulting Q-factor is calculated as 1.9, which corresponds with the estimated Q-factor of 2 as provided in the datasheet. While the datasheet does not state how the electrical impedance is measured, the experimentally measured electrical impedance can be influenced by the use of a long cable.

5.2 Experimental

In this section, the results from the experiments conducted in Chapter 3 are presented. The experiments are conducted on a grout sample 30 cm wide, 30 cm long and 15 cm deep. The grout samples are examined in two variations, with spherical or cylindrical defects and without defects. The main objective is to compare these two sets of grout samples and determine whether the presence of defects can be distinguished based on their reverberation, indicating sound penetration of the grout. To avoid aliasing, the signals start and end as close to zero as possible, leading to slight differences in time windows.

5.2.1 Grout without defects

Fig. 5.2 presents the full reflected signal, with the line denoting the start of reverberation. In Fig. 5.2, the initial pulse corresponds to the reflection from the front of the grout, while the subsequent pulse originates from the rear, which precede the reverberation. The signal of interest is the reverberation of the grout. Since the grout is limited in size end-effects from within the grout may still be present in the reverberation. There is also an concern of internal reflections stemming from air bubbles in the grout. In order to mitigate the impact of these end-effects and internal reflections, the utilisation of Hamming and Hanning windows is explored. Moreover, within TSC Subsea, it is customary to investigate different segments of the signal if the reverberation proves inconclusive or there are suspected end-effects. The utilisation of a bandpass filter of 50 to 150 kHz, which is wider than the bandwidth of the pulse, is implemented to not reduce the frequency components from the pulse, and still reduce the frequency components from the electronics.

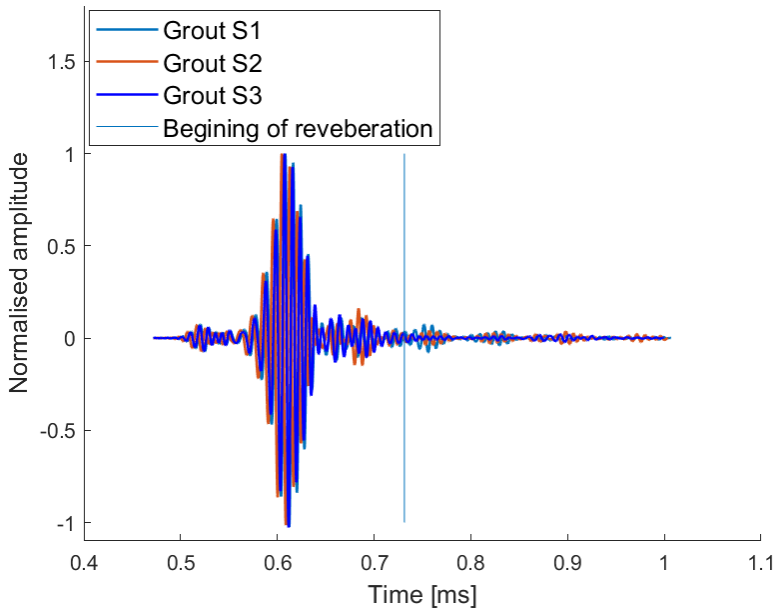

Figure 5.2: Experimental results of the grout without defect, with bandpass filter of 50 to 150 kHz and rectangular window in the time domain.

Fig. 5.3 depicts the reverberation measurements of grout Samples one, two and three using a rectangular window (left) and the corresponding FFTs of these measurements (right).

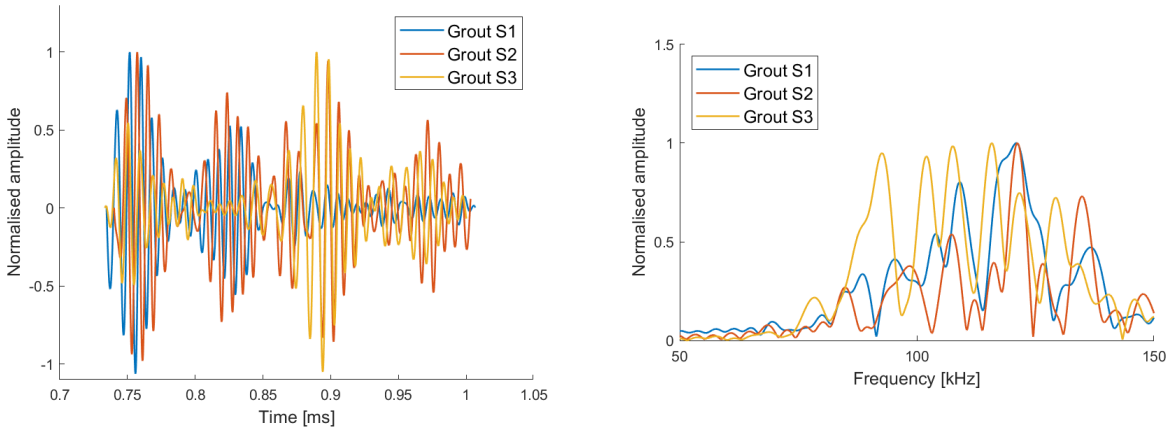

Figure 5.3: Experimental results of the grout without a defect, with a bandpass filter of 50 to 150 kHz and rectangular window in the time (left) and frequency (right) domains, where S1, S2 and S3 are Samples one, two and three, respectively

Similarly, the reverberation measurements of the same grout samples, but using a Hamming window, are presented in Fig. 5.4 (left), with their FFTs displayed on the right. Additionally, the measurements obtained with a Hanning window are illustrated in Fig. 5.5 (left), and their FFTs are showcased to the right.

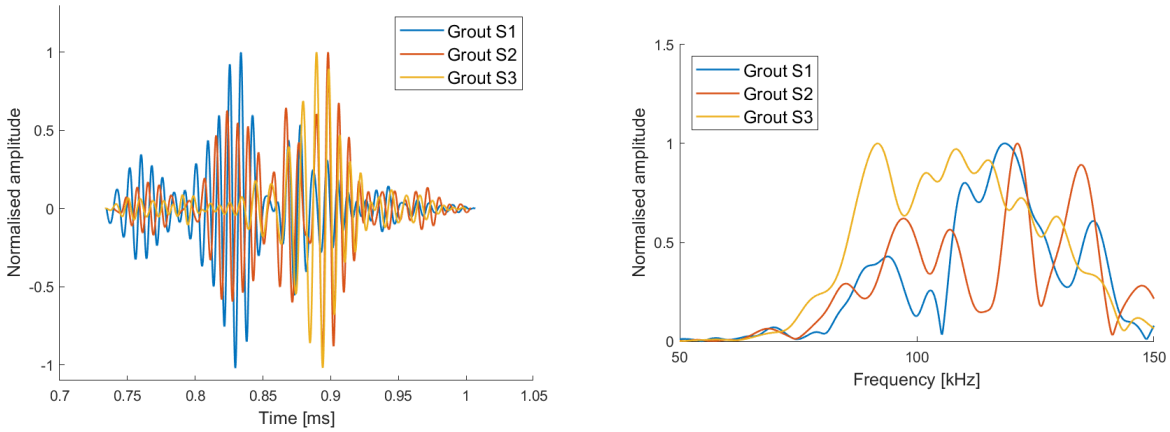

Figure 5.4: Experimental results of the grout without defects with a bandpass filter of 50 to 150 kHz and Hamming window in the time (left) and frequency (right) domains

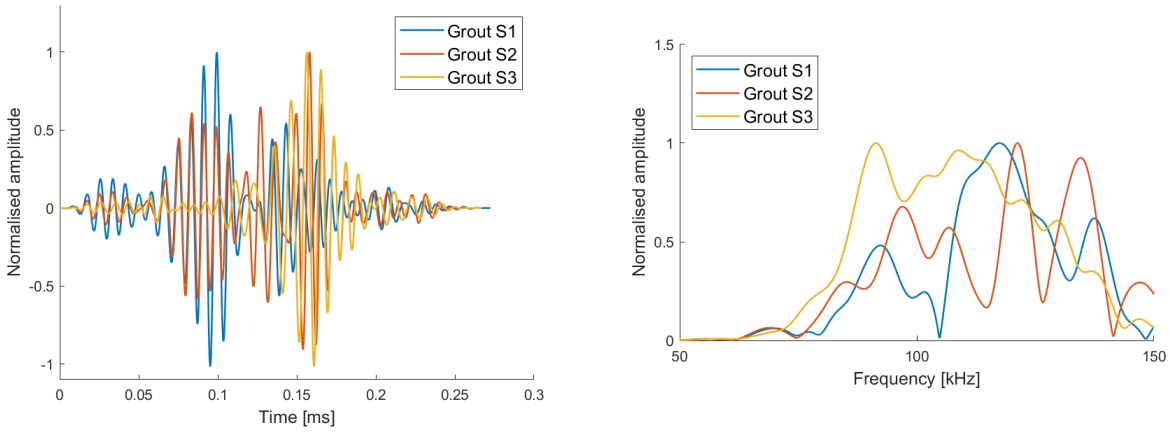

Figure 5.5: Experimental results of the grout without defects with a bandpass filter of 50 to 150 kHz and Hanning window in the time (left) and frequency (right) domains.

Notably, Fig. 5.3 show that Sample three exhibits more pronounced low-frequency components below 110 kHz compared to Samples one and two. However, this distinction is less discernible when using the Hamming and Hanning windows, as demonstrated in Figs. 5.4 and 5.5, respectively. When utilising Hamming or Hanning window Sample two deviates with less frequency components between 110 to 125 kHz.

The implementation of a Hamming or Hanning window reduces the difference among the samples for frequencies under 100kHz, suggesting that certain differences exist at the beginning, end or both of the signal. An initial portion of the signals is removed to investigate the points of deviation in the signals. In Appendix J Fig. J.1, the first 500 samples have been removed, corresponding to a start time of 0.79 ms. The FFT on the right side of the figure reveals that Sample three sill has more frequency components below 110 kHz, with Sample two having less frequency components between 110kHz and 125kHz.

This removal process is extended in Appendix J Fig. J.2, where 700 samples are removed, corresponding to a start time of 0.82 ms. This reduces the difference in the low-frequency components, suggesting that much of the deviation occurs between 0.794 and 0.82 ms, corresponding to the signal arrival of the transition from the second to the third reflection within the concrete. However, the differences in Sample two are increased.

Similarly, investigating the end portions of the signals, the last 500 and 700 samples are removed, equivalent to an end time of 0.95 and 0.92 ms, respectively. These results are displayed in Appendix J Fig. J.3, where the top images correspond to the removal of the

last 500 samples and the bottom images to the removal of the last 700 samples.

In Fig. J.3 (top right), after removing the last 500 samples, the difference in low frequencies is less apparent compared to the full reverberation (Fig. 5.3), although distinctions between sample three and the others remain in frequencies under 110kHz. This difference decreases further with the removal of the last 700 samples, as shown in Fig. J.3 (bottom right). The difference for Sample two in frequencies above 110 kHz shows an improvement, but Sample three now deviates more from Sample one and two in frequencies from 110kHz to 125 kHz.

By removing either the initial or final samples of the reverberation, the differences in frequencies under 110 kHz between the samples become less obvious, but differences in frequencies over 110 kHz improve little. This trend persists in the top-right of Fig. 5.6, where removing the first and last 500 samples show reduced differences in low frequencies compared to the full reverberation, yet differences above 110 kHz remain. This pattern is further highlighted in the bottom-right of Fig. 5.6, where the first and last 700 samples are removed.

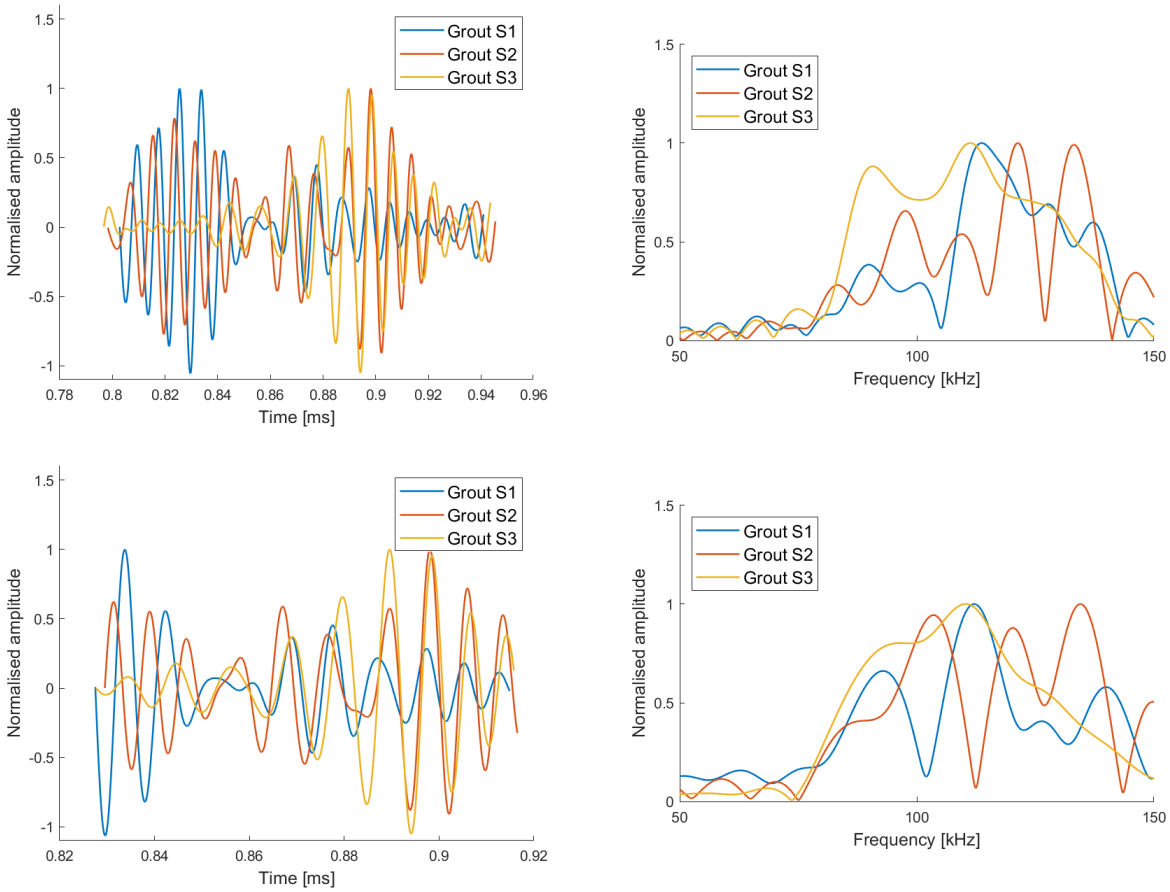

Figure 5.6: Experimental results of the grout without defects, with a bandpass filter of 50 to 150 kHz and a rectangular window for the last and first 500 samples removed in the time (top left) and frequency (top right) domains and last and first 700 samples removed in time (bottom left) and frequency (bottom right) domains

The observed differences between the grout samples may stem from varying characteristics, including size and density, as shown in Appendix F. The presence of bubbles within the samples can also affect the results.

5.2.2 Grout with cylindrical defect

Fig. 5.7 presents the full reflected signal, with the start of reverberation denoted by the line. The signal of interest is the reverberation without end-effects, as the grout without defects. For Cylindrical Sample 1 the secondary pulse from the back of the grout seems to be extended, therefore it will be of particular interest to remove the first samples. Fig. 5.8 (left) show the reverberation measurements of grout Samples one and two with a cylindrical defect, utilising a rectangular window. The corresponding FFTs are displayed on the right side of the figure.

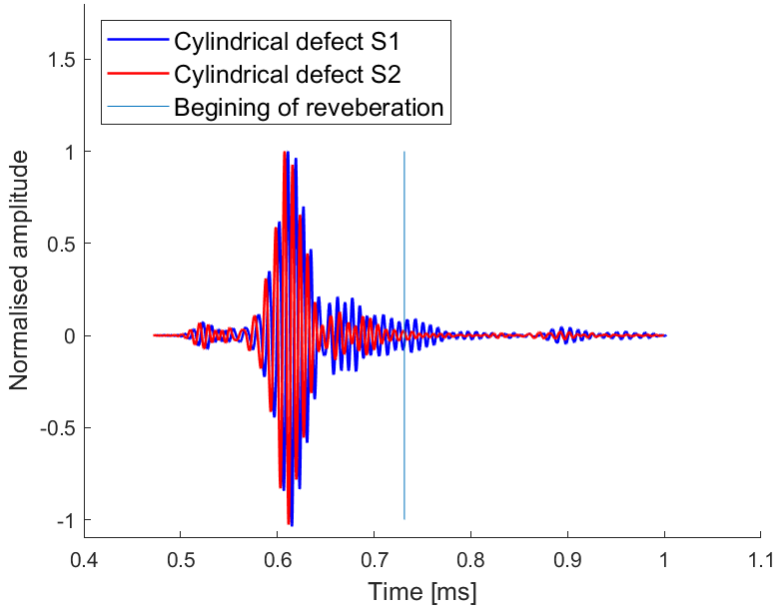

Figure 5.7: Experimental results of the grout with cylindrical defect, with bandpass filter of 50 to 150 kHz and rectangular window in the time domain.

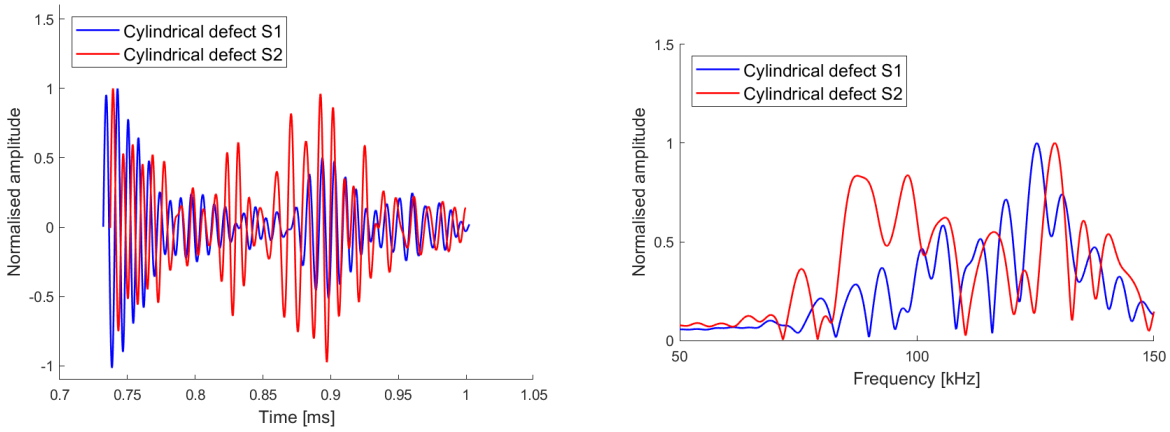

Figure 5.8: Experimental results of the grout with a cylindrical defect, with a bandpass filter of 50 to 150 kHz and a rectangular window in the time (left) and frequency (right) domains, where S1 and S2 are Samples one and two, respectively

In a similar manner, the reverberation measurements of the same grout samples, but employing a Hamming window, are showed in Fig. 5.9 (left), accompanied by their FFTs displayed on the right. Additionally, the measurements obtained using a Hanning window are showed in Fig. 5.10 (left), with their FFTs showcased on the right.

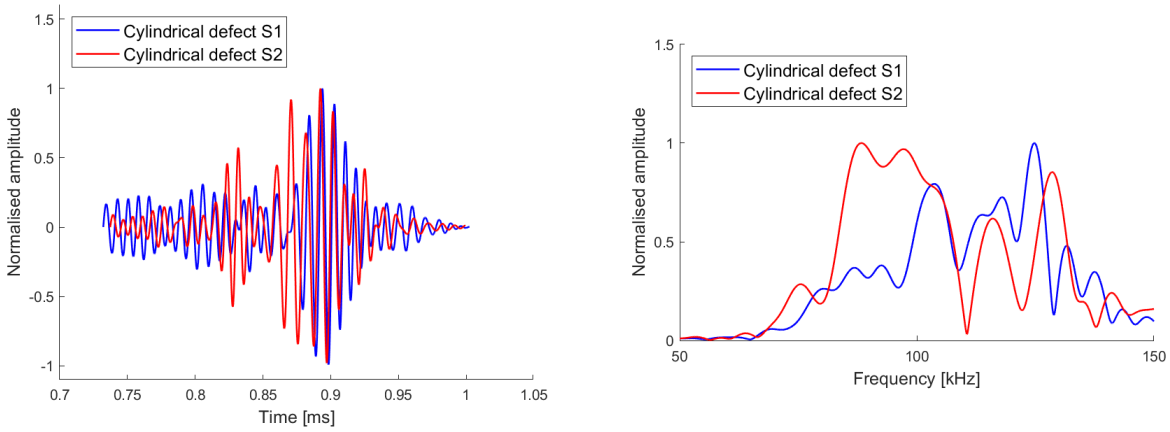

Figure 5.9: Experimental results of the grout with a cylindrical defect, with a bandpass filter of 50 to 150 kHz and Hamming window in the time (left) frequency (right) domains, where S1 and S2 are Samples one and two, respectively

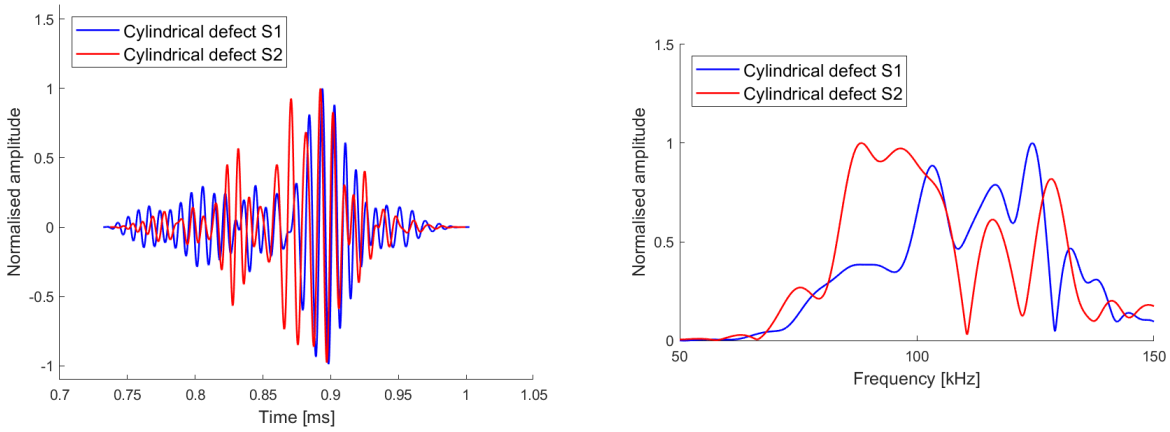

Figure 5.10: Experimental results of the grout with a cylindrical defect, with a bandpass filter of 50 to 150 kHz and Hanning window in the time (left) and frequency (right) domains, where S1 and S2 are Samples one and two, respectively.

Similar to the grout samples without defects, a significant difference exists between the samples in the lower frequencies under 100 kHz. This contrast persists even when the Hamming and Hanning windows are applied. However, the differences in frequencies above 100 kHz improve significantly when a Hamming or Hanning window is applied. The improvement of frequencies above 100kHz indicates that some of the differences are in the start and end of the signal. As previously conducted, certain samples are removed to investigate the points where the signals differs. The results of removing 500 samples at the start (start time 0.79 ms) are presented in Fig. 5.11 (top), while the removal of 700 samples (start time 0.82 ms) is presented in the lower part. With a start time of 0.79 and 0.82 ms the full extended secondary pulse is outside the rectangular window.

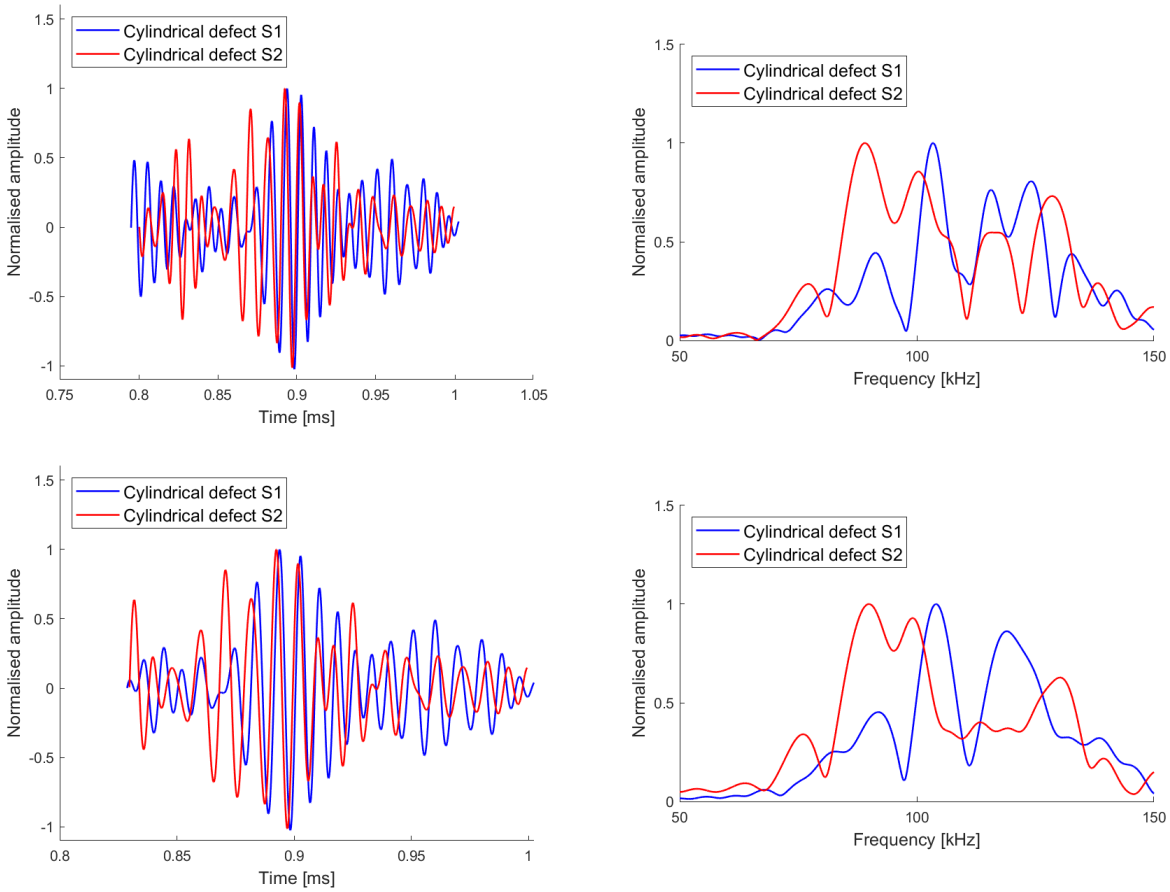

Figure 5.11: Experimental results of the grout with a cylindrical defect, with a bandpass filter of 50 to 150 kHz and a rectangular window for the first 500 samples removed in the time (top left) and frequency (top right) domains and first 700 samples removed in the time (bottom left) and frequency (bottom right) domains

Despite the removal of the initial samples of the signal with the extended secondary pulse, the deviations in the low-frequency components remain evident, as shown in Fig. 5.11. The differences in frequencies above 100 kHz improve substantially when removing the first 500 samples. However, removing 700 samples from the start leads to a noticeable difference in the frequency components above 100 kHz, as displayed in Fig. 5.11 (bottom right).

Similarly, when examining the end portions of the signals, the last 500 and 700 samples are removed (end times of 0.95 and 0.92 ms), as shown in Appendix J Fig. J.4 (left and right, respectively).

In Fig. J.4 (top right), after discarding the last 500 samples, the difference in low frequen-

cies remains as apparent as in the full reverberation in Fig. 5.3. This distinction diminishes slightly with the elimination of the last 700 samples, as shown in Fig. J.4 (bottom right). Regardless, the differences in the frequencies above 100 kHz are slightly worse.

By removing the initial samples of the reverberation, the differences in frequencies under 100 kHz do not appear to be significantly affected, but differences in frequencies over 100 kHz become less pronounced when the initial 500 samples are removed. However, when 700 samples are removed, the difference in frequencies above 100 kHz increase substantially and the differences in frequencies under 100 kHz decrease slightly.

This trend persists in Fig. J.5 (top right), where eliminating both the first and last 500 samples results in reduced differences compared to the full reverberation. Yet, when removing the first and last 700 samples, the differences in frequencies above 100 kHz are substantial, shown in Appendix J Fig. J.5 (bottom right).

To discern whether the differences lie in the middle part of the reverberation, the first and last 500 samples of the reverberation are investigated. The first 500 samples correspond to the time range from 0.735 to 0.79 ms, which contain most of the extended secondary pulse. The first 500 samples are shown in Fig. 5.12 (top). Similarly, the last 500 samples correspond to the time range from 0.95 to 1 ms, showed in Fig. 5.12 (bottom).

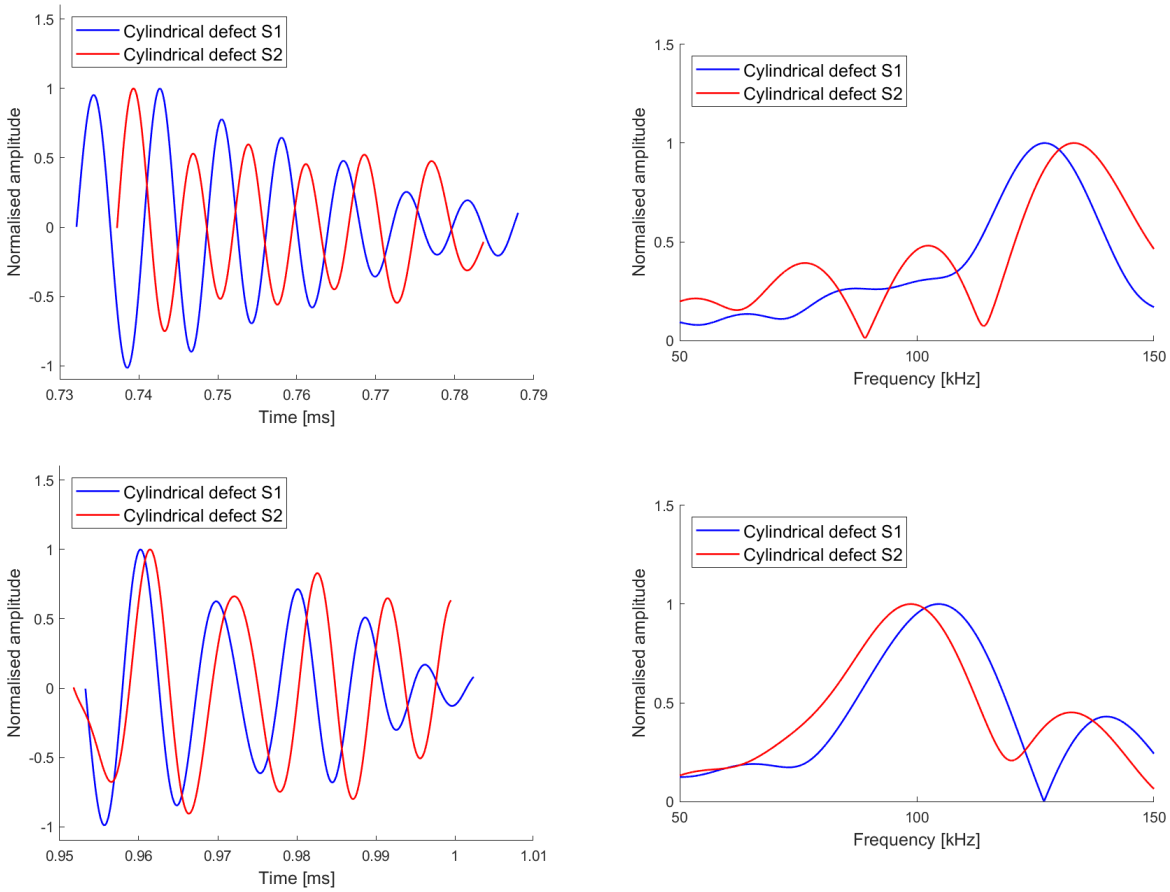

Figure 5.12: Experimental results of the grout with a cylindrical defect, with a bandpass filter of 50 to 150 kHz and a rectangular window for the first 500 samples in the time (top left) and the frequency (top right) domains and last 500 samples in the time (bottom left) and frequency (bottom right) domains

The first and last 500 samples of the reverberation exhibit closer correspondence than the middle portion, resulting in a significant reduction in the differences in the frequency components, especially for the last 500 samples. This suggests that the differences primarily arise from the middle part of the reverberation. Nevertheless, the signals only consist of a few wavelengths.

As with the grout samples without defects, the observed differences between the grout samples may stem from varying characteristics, including size and density, as shown in Appendix F, and the presence of bubbles within the samples.

5.2.3 Grout with spherical defect

The full reflected signal is presented in Fig. 5.13, with the start of the reverberation being denoted by the line. As before the signal of interest is the reverberation without end-effects. There is a notable third reflection, which indicates a reflection. The reflection might be a result of the grout sample two with spherical defect being damaged, showed in Fig. 5.14, as it is the only sample exhibiting this third pulse. As a result it is of interest to look at the signal before, after and under this third pulse, to determine if it impacts the reverberation.

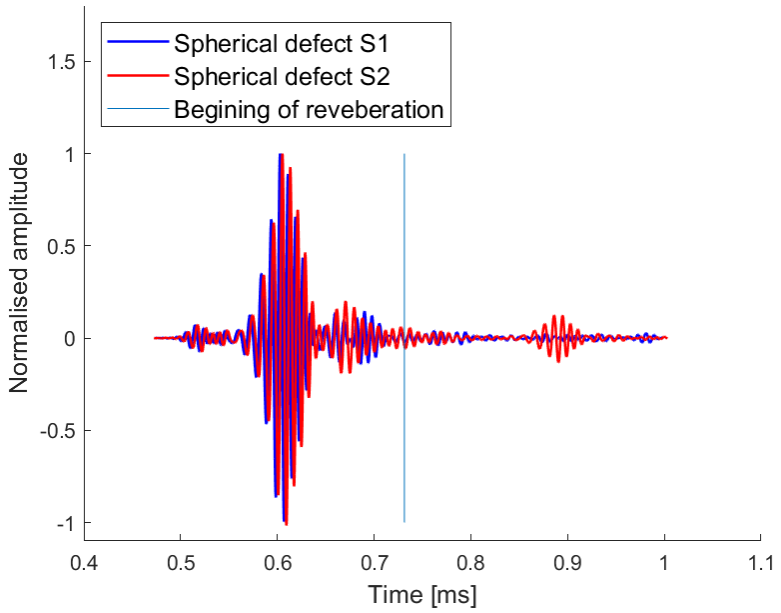

Figure 5.13: Samples one and two with spherical defect full reflection in the time domain

Figure 5.14: Grout Sample two with spherical defect

Fig. 5.15 (left) portrays the reverberation measurements of grout Samples one and two with spherical defects, utilising a rectangular window. The corresponding FFTs of these measurements are displayed on the right side.

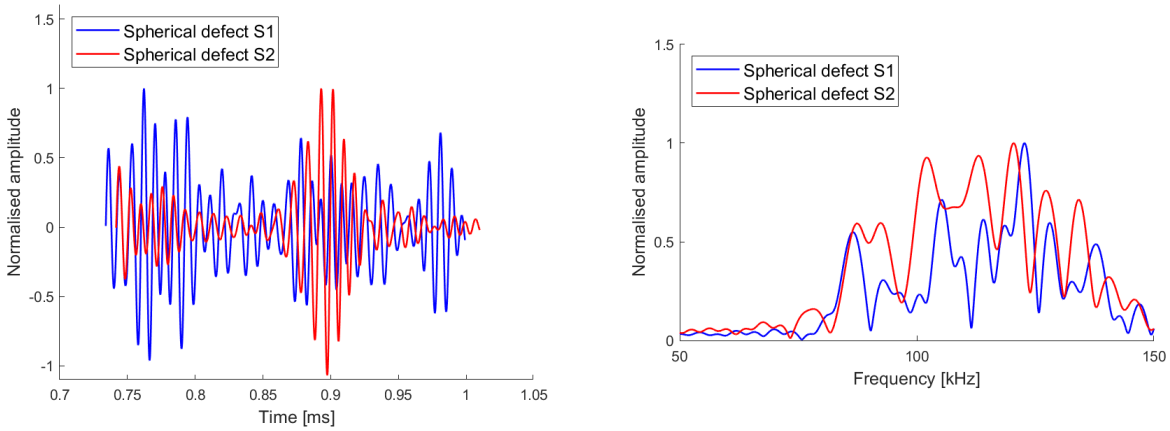

Figure 5.15: Experimental results of the grout with a spherical defect, with a bandpass filter of 50 to 150 kHz and a rectangular window the time (left) and frequency (right) domains, where S1 and S2 are Samples one and two, respectively.

In a similar manner, the reverberation measurements of the same grout samples, but employing a Hamming window, are showed in Appendix J Fig. J.6 (left), accompanied by their FFTs displayed on the right. Additionally, the measurements obtained using a Hanning

window are showed in Appendix J Fig. J.7 (left), with their FFTs on the right.

The reverberations of the grout samples with spherical defects have the largest deviations around 90 to 125 kHz, which is only exacerbated with the Hamming and Hanning filters, indicating that the differences are in the middle of the signal.

As previously conducted, certain samples are removed to investigate the points where the signal deviates. In this part, the study is conducted by assessing the signal before (end time of 0.85ms) and after (start time 0.92ms) the larger pulse, as the size and shape indicate that it might be a reflection, which affects the reverberation. This signal also dominates the frequency spectrum, as the amplitude is much greater than the rest of the reverberation. The reverberation up to the larger pulse is presented in Fig. 5.16 (top left), and the reverberation after the larger pulse is shown in the lower left of the figure, with their corresponding FFTs on the right.

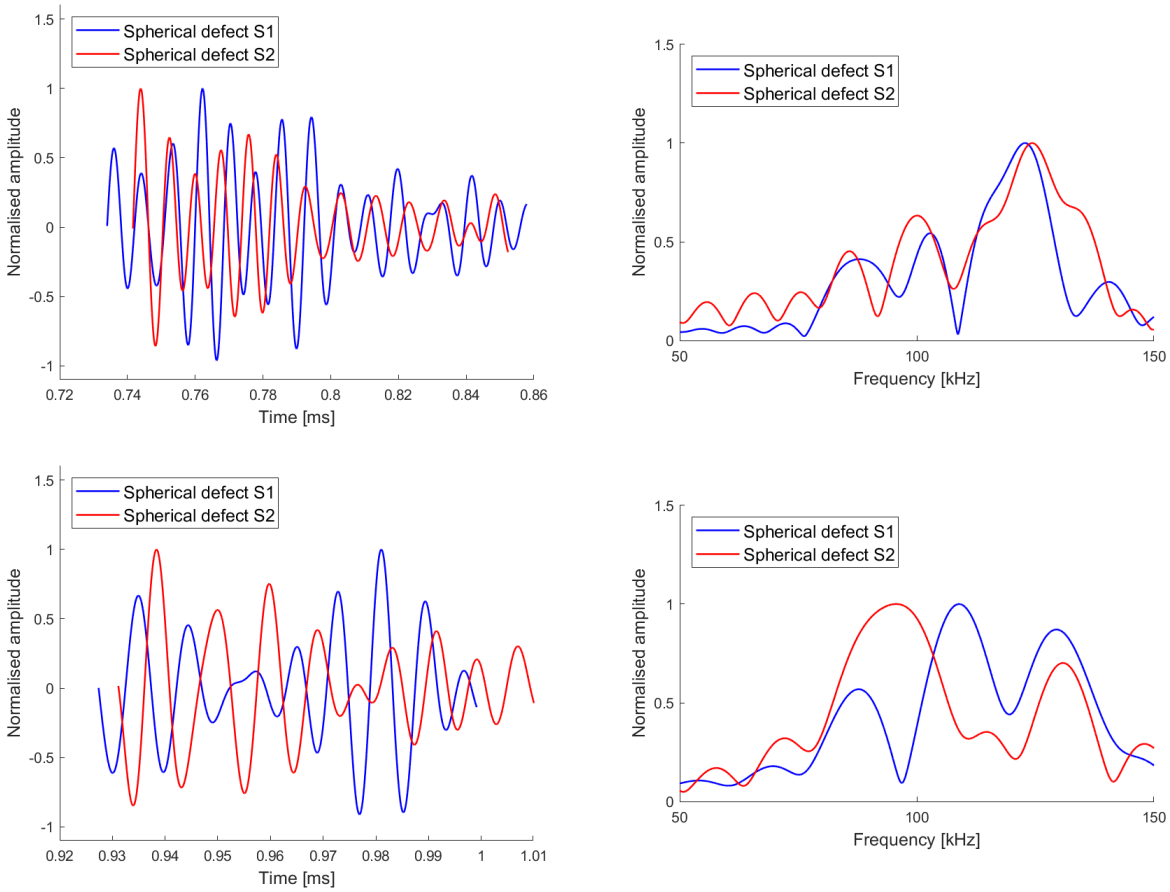

Figure 5.16: Experimental results of the grout with a spherical defect, with a bandpass filter of 50 to 150 kHz and a rectangular window for reverberation before the larger pulse in the time (top left) and frequency (top right) domains and reverberation after the larger pulse in the time (bottom left) and frequency (bottom right) domains

The frequencies in the reverberations before the larger pulse shown in Fig. 5.16 (top right) correspond well. The reverberations after the pulse differs, with the strongest frequency components for Sample two being around 20 kHz lower than Sample one, as shown in Fig. 5.16. The larger pulse in the reverberation is plotted in Appendix J Fig. J.8 to determine if the frequency components differs in this section.

The frequency components within the larger pulse from Sample two differs from those of Sample one with one large lobe encompassing frequencies from 70 to 150 kHz, while Sample one has multiple frequency lobes, as shown in Fig. J.8.

As with the other grout samples, the observed differences between the grout samples may

stem from varying characteristics, including size and density, shown in Appendix F, and the presence of bubbles within the samples. The results may also be affected by grout Sample two with spherical defect being damaged, as shown in Fig. 5.14

5.2.4 Comparison

In this section, comparisons are drawn between different segments of the signal using rectangular filters. The application of Hamming and Hanning filters does not notably enhance the correlation between samples compared to the removal of the initial and final samples.

In Fig. 5.17 (left), the FFT of the full reverberation of grout with cylindrical defects is compared to that of the grout without defects, and the grout with spherical defects is compared to the grout without defects on the right.

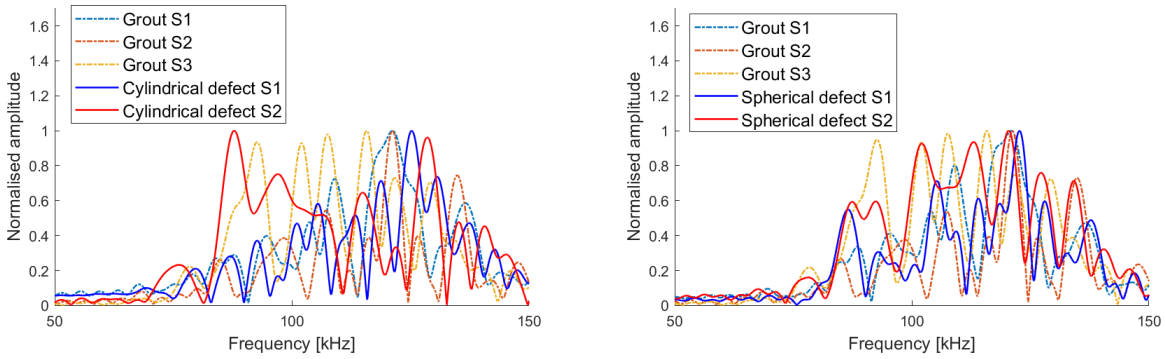

Figure 5.17: Experimental results of the grout with and without defects, with a bandpass filter of 50 to 150 kHz and a rectangular window for the full reverberation for cylindrical (left) and spherical (right) defects

However, the dissimilarities among samples with the same defects or lack thereof are so substantial that meaningful distinctions between the two types are difficult to ascertain. Notably, the grout samples without defects exhibit the highest correspondence in the central portion of the reverberations after removing 700 samples from both the start and end. Fig. J.9 shows the comparison with this specific sample adjustment. The left side of the figure presents the comparison between grout samples with and without cylindrical defects, while the right side shows the comparison between grout samples with and without spherical defects.

Similar to the complete signal, the difference between samples with identical defects or lack thereof is so substantial that identifying a significant difference between samples with and without defects is not feasible. The grout samples with defects have the largest degree of correspondence at the start of the reverberation. Fig. J.10 (top) displays the initial 700 samples of the reverberation, while the final 700 samples are shown in the bottom of the figure. As in the previous figures, cylindrical defects are shown on the left, and spherical defects are presented on the right.

While the variation between samples with identical defects or lack thereof is somewhat reduced when examining the signal's initial segment, no noticeable distinctions persist between samples with and without defects, as illustrated in Fig. J.10 (top). In the final segment of the reverberation, as depicted in Fig. J.10 (bottom), the difference between samples with the same defects or absence thereof remains so significant that determining a substantial difference between samples with and without defects is unattainable.

Given that the samples with spherical and cylindrical defects do not correlate at the same points as samples without defects, conducting a comparison between samples with and without defects is challenging. Additionally, resonance frequencies and scattering patterns have not been examined, as samples with identical defects exhibit different frequency responses, rendering it impossible to determine whether the frequency components originate from the defects or the grout itself.

5.3 Simulation results and discussion

This section presents the simulation results obtained in Chapter 4, focusing on grout samples with and without spherical or cylindrical defects. The chapter is divided into two subsections, one covering simulations resembling the experiments conducted in Section 4.4 and the other addressing simulations of semi-infinite grout with a width of 15 cm conducted in Section 4.3. In both cases, the simulations of the grout with defect or lack thereof are compared to determine the acoustic penetration of the grout.

5.3.1 Semi-infinite

In Fig. 5.18, the complete reflected signal is showed, with the beginning of the reverberation denoted by the line. Similar to the experimental findings, the primary focus is the rever-

beration originating from the grout. Unlike the experimental setup, extracting the grout's reverberation devoid of end-effects or residual reflections is comparatively more straightforward in simulations. This is attributed to the infinitely wide grout sample with uniform material characteristics, which removes the concern of end-effects and internal reflections. Notably, at the initiation of the reverberation, the signal exhibits a higher amplitude than the subsequent portions of the reverberation. Hence, the utilisation of Hamming and Hanning windows becomes interesting to limit the influence from the beginning of the reverberation.

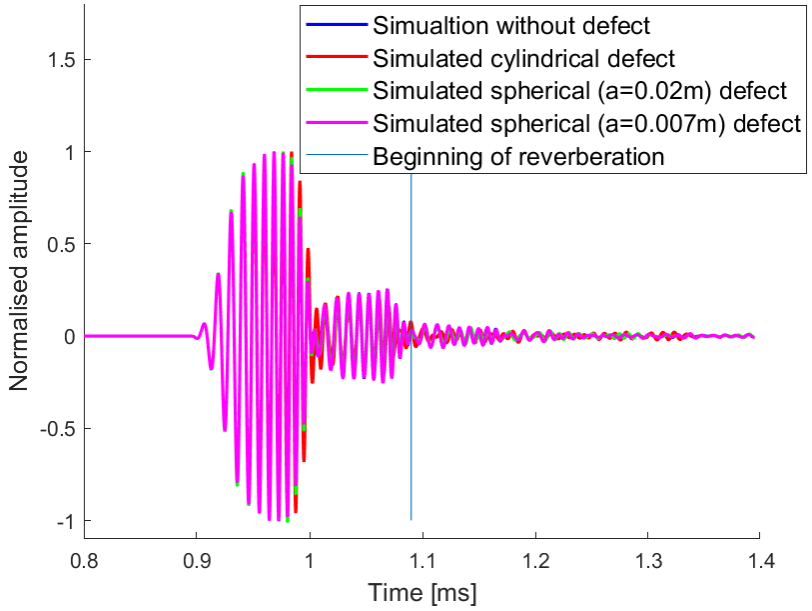

Figure 5.18: Simulations of grout without end-effects full reflection in time domain

The scattering cross-section of the spherical defect is depicted in Appendix K Fig. K.1. The results from the scattering cross-section should be questioned as the formula is for a spherical fluid inside a fluid medium, instead of a solid medium. The dampening coefficient is also for water instead of grout as the damping coefficient for grout cannot be calculated with the fluid medium formula. Nevertheless, the results from the scattering cross section indicates that the size of the bubble has a higher impact on visibility than the resonance frequency. This should be taken with a grain of salt as the dampening coefficient have a large impact on the amplitude at resonance, shown in Appendix K Fig. K.2.

The smaller spherical defect with a diameter of 0.014m is just above half the wavelength for 135kHz, and well below half the wavelength for lower frequencies. Defects with dimensions smaller than half the wavelength are challenging to detect [43].

The results of the simulations from Chapter 4, involving semi-infinite grout with a width of 15 cm and employing a rectangular window, are depicted in Fig. 5.19 (left), with the corresponding FFT presented on the right.

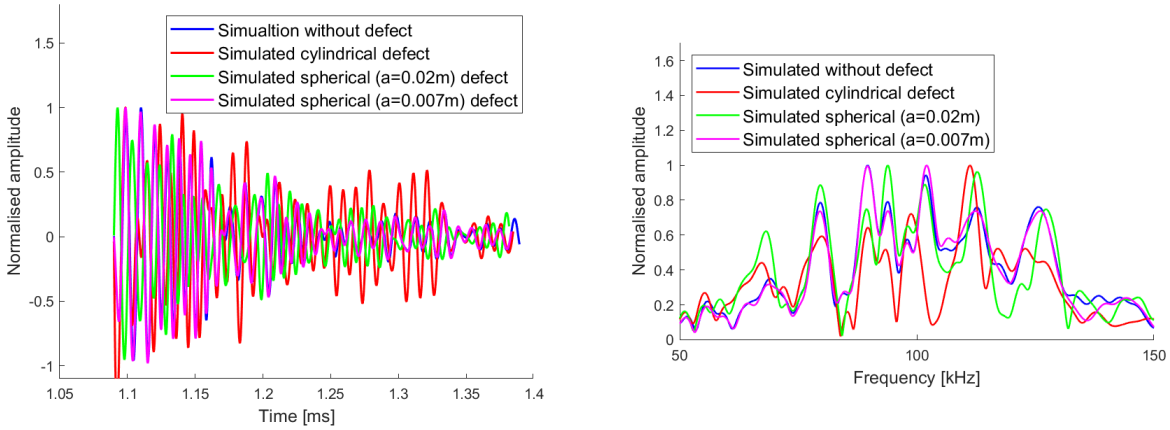

Figure 5.19: Simulated results of semi-infinite grout with and without defects and a rectangular window, showing the reverberation in the time (left) and frequency (right) domains

The resonance frequencies for the thickness resonance in the grout is 12.3 KHz for the compressional wave and 7.8 kHz for the shear wave. The frequency response in Fig. 5.19 is very complex and it is hard to determine if the frequency tops coincide with the higher harmonics of the thickness resonance frequencies of the grout.

The findings depicted in Fig. 5.19 reveal almost identical response from the simulation of the grout without defect and the grout with a spherical defect with a radius of 0.007m. There are slight differences between grout without defect and the simulations with larger defects, with the simulation with cylindrical defect differing the most.

Fig. 5.20 (top and bottom, respectively) displays the result of the simulations carried out using a Hamming window and a Hanning window in place of a rectangular window. The left side shows the reverberation in the time domain, while the corresponding FFT is displayed on the right.

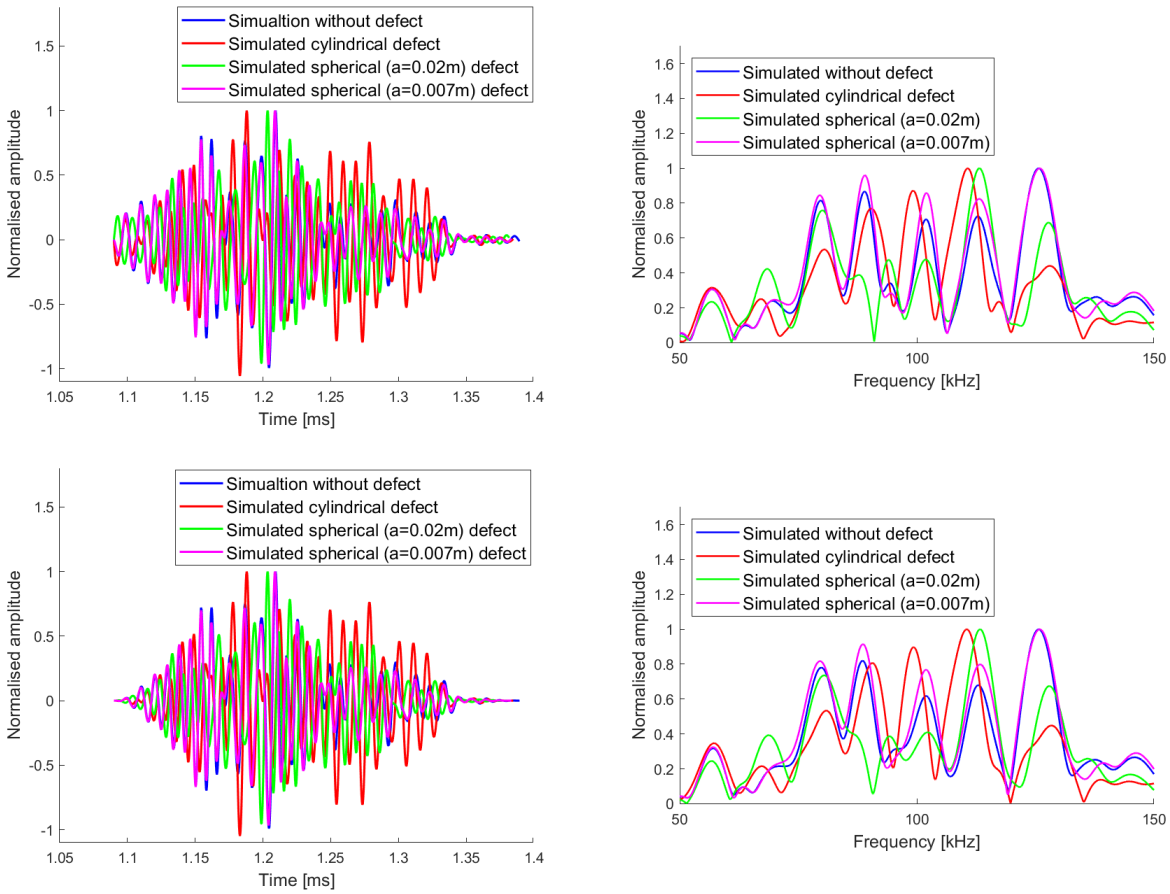

Figure 5.20: Comparing simulated results of semi-infinite grout with and without defects and a Hamming window (top) and a Hanning window (bottom) in the time (left) and frequency domains (right)

Applying a Hamming or Hanning filter to the signal, as depicted in Fig. 5.20, results in fewer prominent frequency peaks, which simplifies the process of discerning differences between the simulations and resonance frequencies from the grout. The frequency tops, except the first one, for the simulated grout without defects have around 12.3 kHz between each top, indicating that the frequency tops are higher harmonics of the resonance frequency. The distance between the first and second frequency top is about 8.5 kHz, which does not coincide with any of the thickness resonance frequencies. The spherical defect of 0.007m seams to be to small to cause a discernible difference with very minor differences between the simulation of grout without a defect and grout with the smaller spherical defect. The differences between the simulated grout without defect and the grout with the larger defects has increased. There is an especially large difference between the simulation with the larger spherical defect, which is interesting considering that the cylindrical defect is larger in size.

Fig. 5.21 show the complete signal from simulations without defects of steel–grout–steel, steel–grout and grout. The secondary pulse, resulting from the reflection at the back of the grout, almost completely dissipates in the steel–grout and steel–grout–steel simulations.

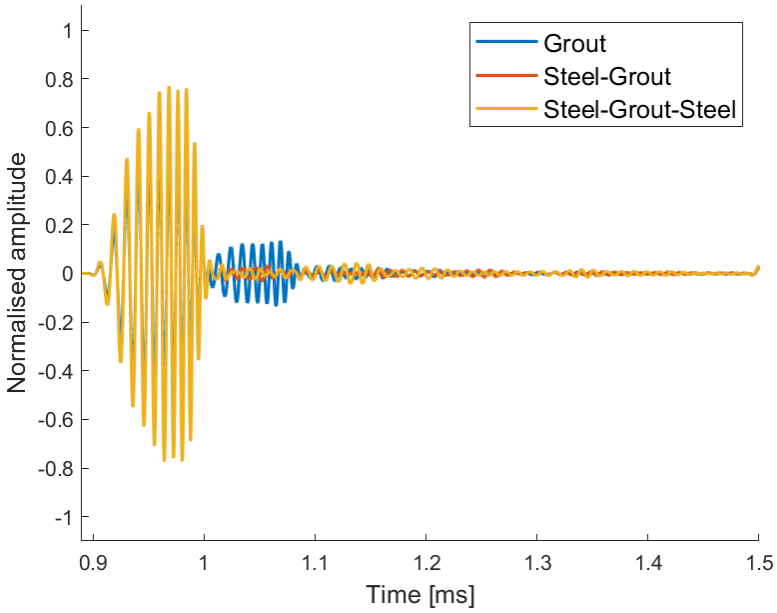

Figure 5.21: Full signal simulation results in time domain for steel–grout–steel, steel–grout and grout.

The simulations with a 0.03 m steel plate in front of the grout is showed in Fig. 5.22, with the corresponding FFT presented on the right.

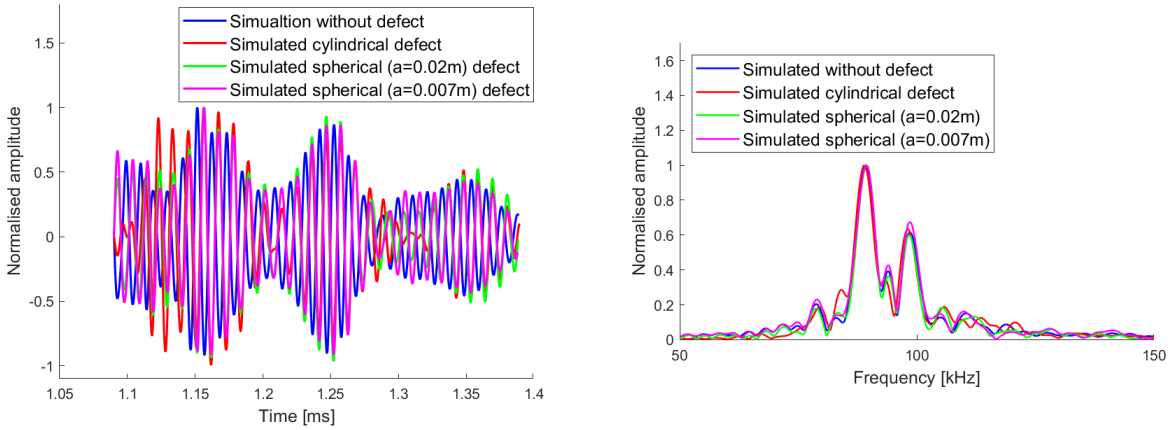

Figure 5.22: Simulated results of semi-infinite steel–grout with and without defects and a rectangular window, showing the reverberation in the time (left) and frequency (right) domains

When a steel plate is positioned in front of the grout, there are only two large frequency

tops around 80kHz and 100kHz. The thickness resonance frequencies for the steel are 98 kHz for the compressional wave and 52 kHz for the shear wave. The frequency top around 100 kHz correspond well with the compressional wave thickness resonance for the steel, but the larger pulse around 80 kHz does not match the resonance frequency for the grout or the steel. The resonance frequency for around 80 kHz might be modal coupling between a higher order thickness resonance in the grout and steel [45], or the resonance for the multi layered system [30]. However, this is outside the scope of this study and will not be discussed further.

With a steel plate positioned in front of the grout there are no observable differences between the simulations with defects or lack thereof. This suggests that the reverberation originating from the steel plate predominantly shapes the signal or that the acoustic signal fails to deeply penetrate the grout.

The results of the steel–grout simulations using a Hamming or Hanning window in place of a rectangular one are displayed in Appendix J Fig. J.11 (top and bottom, respectively). On the left side, the reverberation in the time domain is illustrated, and on the right side, the corresponding FFT is presented. Despite the use of a Hamming or Hanning window, there are only minor differences between the simulation of the grout with defects or lack thereof.

Fig. 4.1 shows the results from the simulations with a 0.03 m wide steel plate positioned in front of and behind the grout sample. These results are depicted in Fig. 5.23 using a rectangular window. The left side portrays the reverberation in the time domain, accompanied by the corresponding FFT on the right.

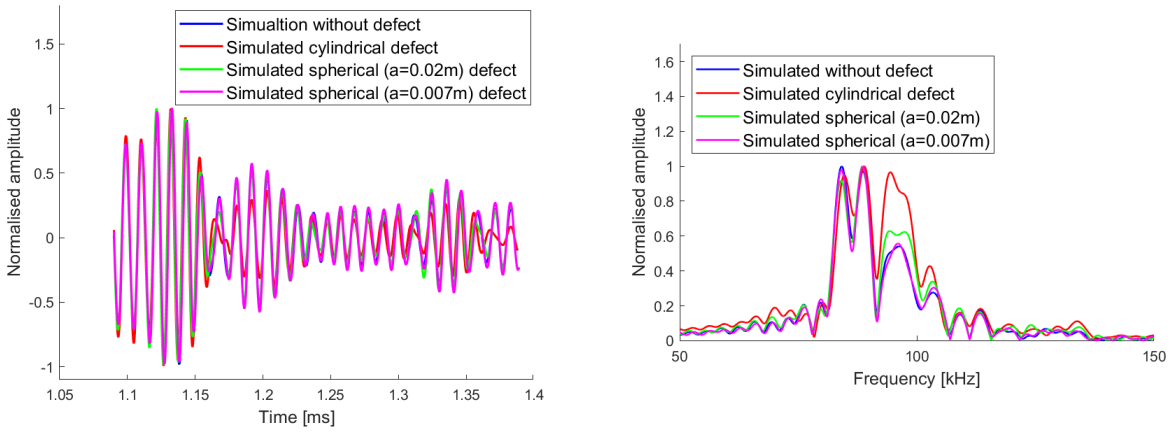

Figure 5.23: Simulated results of semi-infinite steel–grout–steel with and without defects and a rectangular window, showing the reverberation in the time (left) and frequency (right) domains

When a steel plate is placed both in front and behind the grout, there are three large frequency tops and one smaller one. There is one large frequency top from 90 to 100 KHz, and a double frequency top around 80 to 90 kHz. As before, does the frequency top around 90-100 kHz coincide with the compressional wave thickness resonance frequency of the steel plate in front and behind the grout. However, the frequency tops between 80 to 90 kHz does not fit any thickness resonant frequency and the dip in frequency coincides with the seventh order compressional wave thickness resonance frequency for the grout. However, this will not be investigated further in this study.

The difference between the simulation results involving a spherical defect and without any defect is minor. In the case of a cylindrical defect, a more noticeable difference is present, albeit the discrepancy lies primarily in the magnitudes of the frequency peak around 100 kHz.

The outcomes of simulations utilising Hamming and Hanning windows instead of a rectangular window are illustrated in Fig. 5.24 (top and bottom, respectively), with the time-domain reverberation to the left and the corresponding FFT on the right.

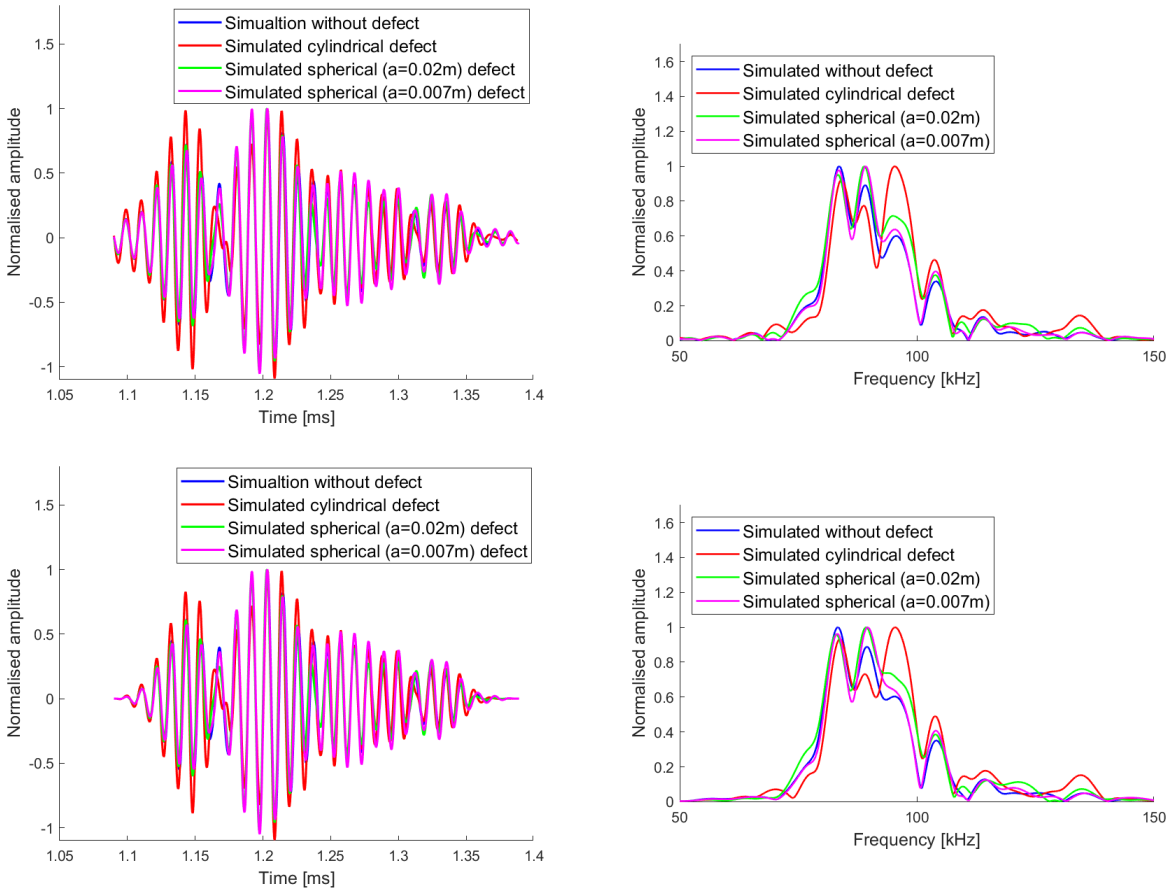

Figure 5.24: Simulated results of semi-infinite steel–grout–steel with and without defects and Hamming (top) or Hanning (bottom) window, showing the reverberation in the time (left) and frequency domains (right)

Interestingly, when a Hamming or Hanning filter is applied the frequency tops are more evenly spaced and broader. The differences between simulations featuring a spherical defect and without remains minimal. Nevertheless, the simulation involving a cylindrical defect still has a noticeably higher magnitude for the frequency top right before 100 kHz.

In the simulation without any steel plates the larger spherical defect and cylindrical defect differs from the one without defect. However, when a steel plate was added in front of the grout there where only minor differences between the simulations with defects or lack thereof. Interestingly, when a steel plate was added to the back of the grout the simulation with cylindrical defect differed from the one without defect, which indicates some level of penetration of the grout. Reducing the influence of the steel plate on the signal with signal processing might make it possible to detect the spherical defect, but is outside the scope of this study.

5.3.2 Simulating of the experiment

Within this section, the simulation results concerning a grout cylinder having a radius of 15 cm and a width of 15 cm are showed. These simulations encompass scenarios with and without defects, as detailed in Section 4.4. Fig. 5.25 (left) portrays the reverberation results when employing a rectangular window, while the corresponding FFT results are depicted on the right side.

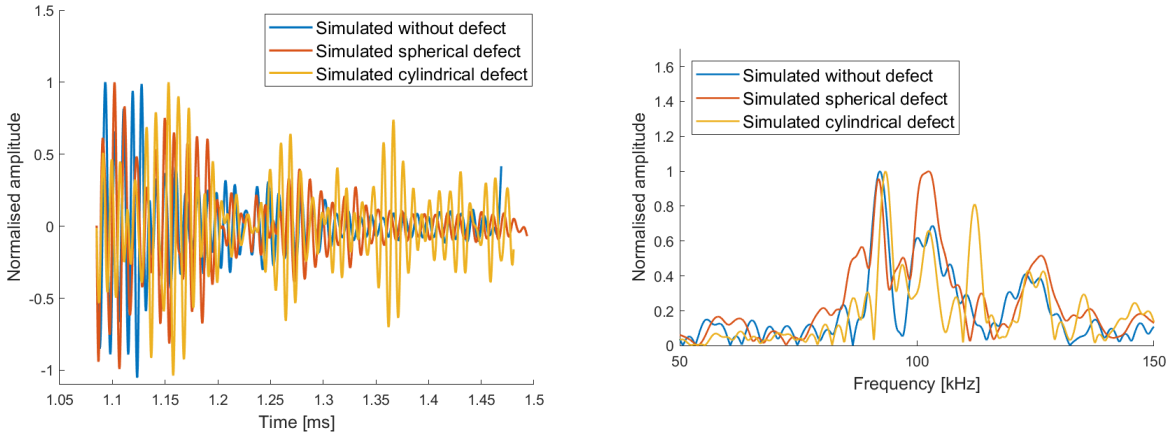

Figure 5.25: Simulated results of a grout cylinder with a radius of 15 cm and width of 15 cm with and without defects and a rectangular window, showing the reverberation in time (left) and frequency (right) domains

The simulation involving the spherical defect differs noticeably from the simulation without defect around 100 kHz, whereas the simulation featuring the cylindrical defect differs around 115 kHz. Apart from these frequencies, no significant difference are present between the simulations.

Fig. 5.26 (top and bottom, respectively) show the outcomes of simulations using Hamming and Hanning windows in place of a rectangular one. On the left side, the time-domain reverberation is presented, while the corresponding FFT is shown on the right side.

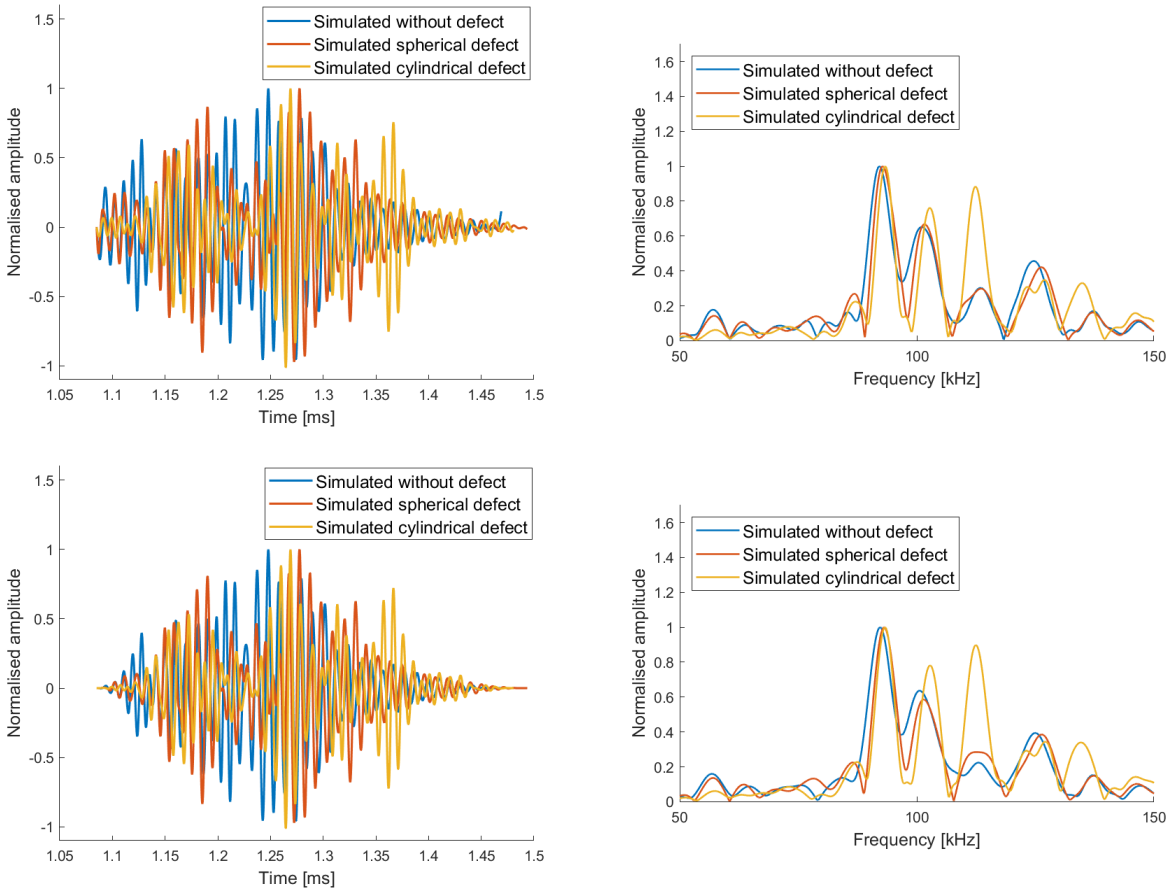

Figure 5.26: Simulated results of a grout cylinder with a radius of 15 cm and width of 15 cm with and without defects and Hamming (top) and Hanning (bottom) windows, showing the reverberation in the time (left) and frequency (right) domains

As with the simulations without end-effects the Hamming and Hanning window makes the frequency spectrum less complex and easier to analyse. The frequency tops for the simulation without defect is around 9-10 kHz which is lower than the thickness resonance frequency. This might be because of modal coupling [45] or stronger resonances, however it will not be investigated further in this study.

The contrast between the simulation without and with a spherical defect diminishes significantly when a Hamming or Hanning window is applied. Meanwhile, the distinction between the simulation without and with a cylindrical defect becomes more noticeable. This observation suggests that the dissimilarity between the simulation with a spherical defect and without a defect primarily emerges at the start and end of the reverberation, whereas the dissimilarity between the simulation with a cylindrical defect and without a defect is

more evident in the middle.

5.4 Comparison of experiment and simulation

This subsection centres on the comparison between the experimental results obtained in Chapter 3 and the simulations of the conducted experiment outlined in Section 4.4. However, several challenges emerge when attempting this comparison. The simulations employ a simple baffled piston model, which does not encompass the effects of electronics and the transducer. Additionally, the electronics utilised in the simulations operate beyond their intended bandwidth, causing distortion in the input pulse. The simulations take place in a 2D-axisymmetric model, as explained in Chapter 4, resulting in a cylindrical-shaped grout rather than a rectangular one. These complexities necessitate careful consideration when evaluating the concurrence between the simulated and experimental data.

Considering that the acoustic wave in the simulation travels 0.4 meters farther than in the experiment, the simulated time axis is adjusted by subtracting $0.4\text{m}/c_{water}$. Moreover, the simulated signal is 0.11 ms longer compared to the experimental signal. Consequently, the simulated signal is shortened by 0.11 ms.

The comparison of reverberations between the simulated and experimental grout without defects is showed in Fig. 5.27 (top left), accompanied by the corresponding FFT to the right. The portion of the experimental signal where the various samples exhibit the closest correspondence lies in the middle, achieved by omitting the initial and final 700 samples. This adjustment corresponds to the removal of the first and last 262 samples in the simulation. In Fig. 5.27 (bottom left), the middle portion of the reverberation is displayed, while the corresponding FFT is presented to the right.

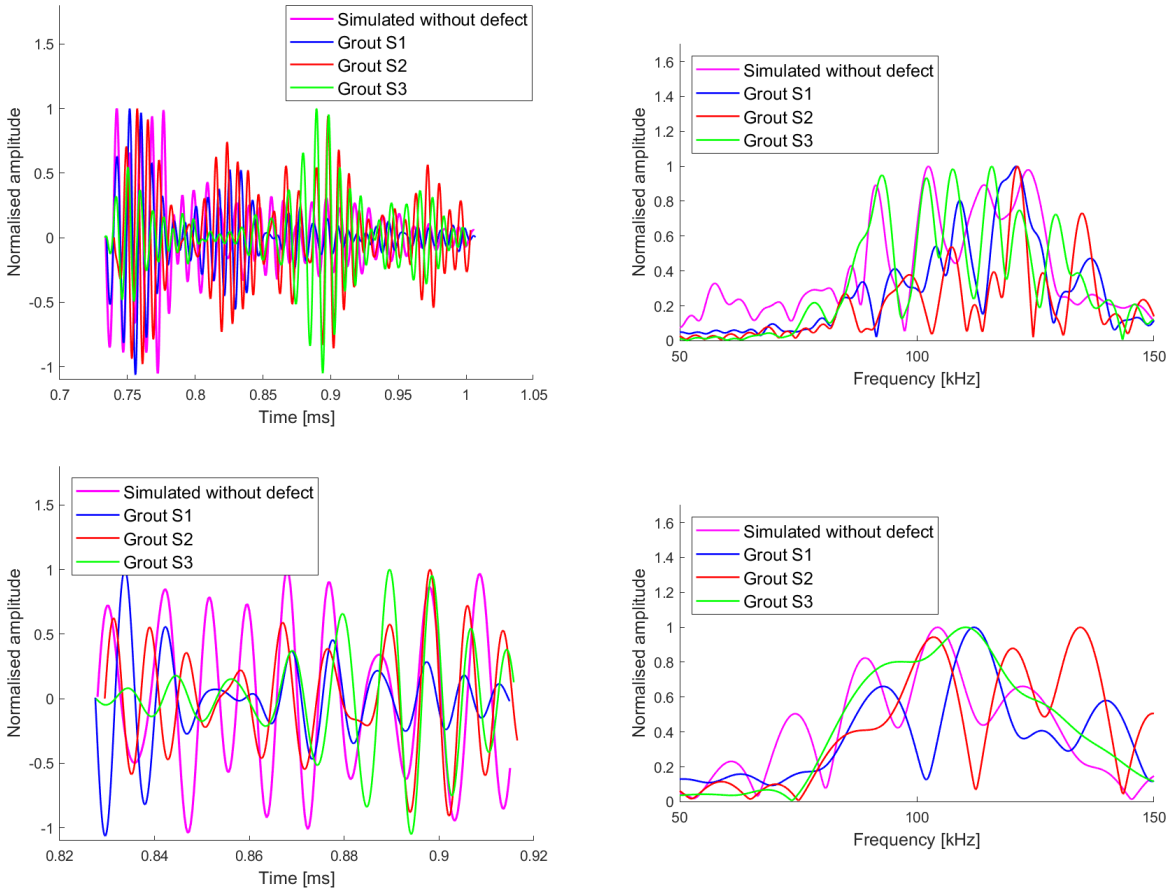

Figure 5.27: Full reverberation of the simulated experiment and experiment without defects with a rectangular window and bandpass filter of 50 to 150 kHz for the experiment in the time (top left) and frequency (top right) domains and the first and last 700 samples removed in the time (bottom left) and frequency (bottom right) domains

For the complete reverberation, a strong correlation exists between the experimental grout Sample three and the simulation within the frequency range of 80–105 kHz, while the correlation diminishes outside of this range. The correlation between the simulation and the other experimental grout samples is minimal. In relation to the middle segment of the reverberation, there is a notable difference between the samples and the simulation.

Turning to the comparison of reverberations involving the simulated and experimental grout samples with cylindrical defects, Fig. 5.28 (top left) show the full reverberation, accompanied by the corresponding FFT on the right. The difference between the experimental grout samples is minimal towards the end of the signal. The final 500 samples of the experimental reverberation, along with 188 samples of the simulation reverberation, are showed in Fig.

5.28 (bottom left), while the corresponding FFT results are shown on the right. This segment represents a relatively small sample size of slightly over six periods, yet it is the only part of the reverberation where the experimental samples exhibit a high degree of correspondence.

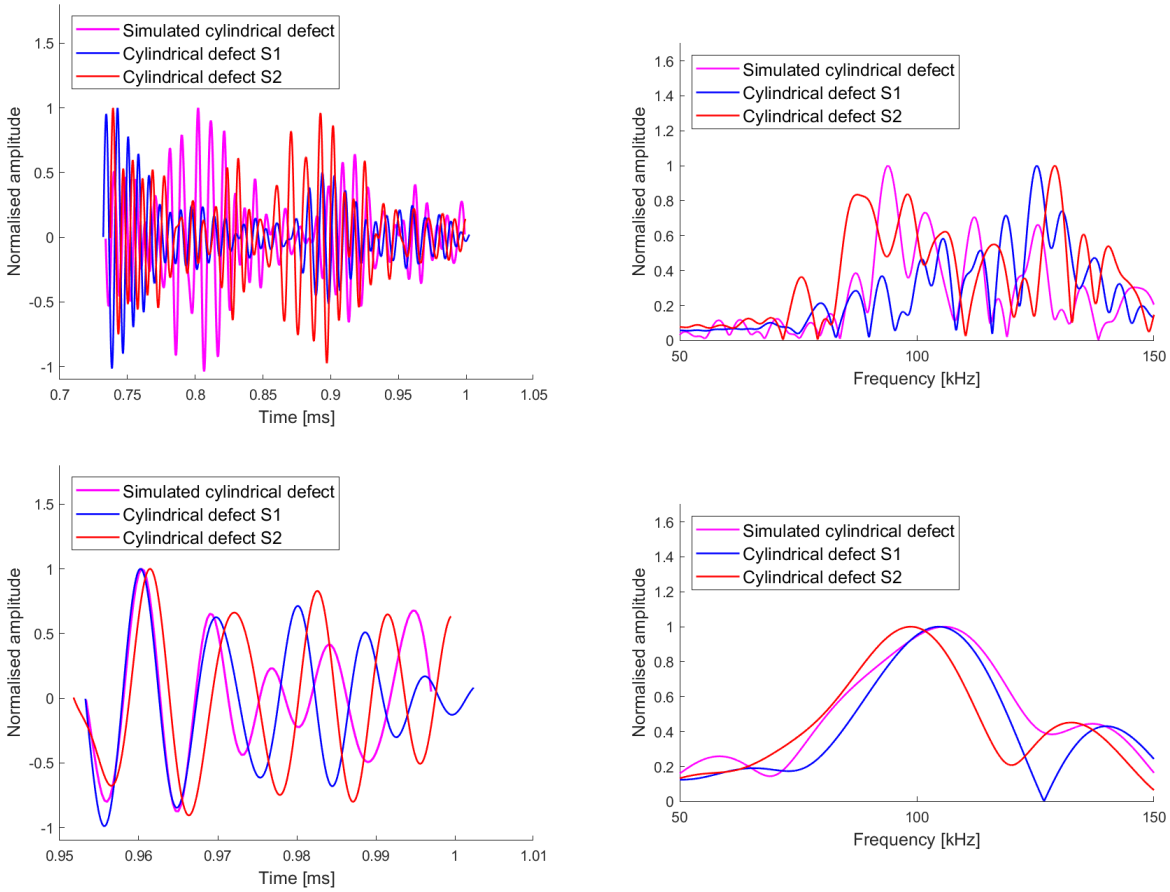

Figure 5.28: Full reverberation of the simulated experiment and experiment with cylindrical defects with a rectangular window and bandpass filter of 50 to 150 kHz for the experiment in the time (top right) and frequency (top right) domains and the last 500 samples in the time (bottom left) and frequency (bottom right) domains

There is an poor correlation between the simulated and experimental samples throughout the entire reverberation. However, within the final 500 samples of the reverberation, a notable correlation emerges, albeit over a span of only six to seven wavelengths.

Fig. 5.29 (top left) show the comparison of reverberations between the simulated and experimental grout samples with a spherical defect, accompanied by the corresponding FFT on the upper right. The experimental grout samples with spherical defects exhibit their highest correspondence before the larger pulse within the reverberation. The pre-pulse reverberation

is displayed in Fig. 5.29 (bottom left), while the corresponding FFT results are shown on the right.

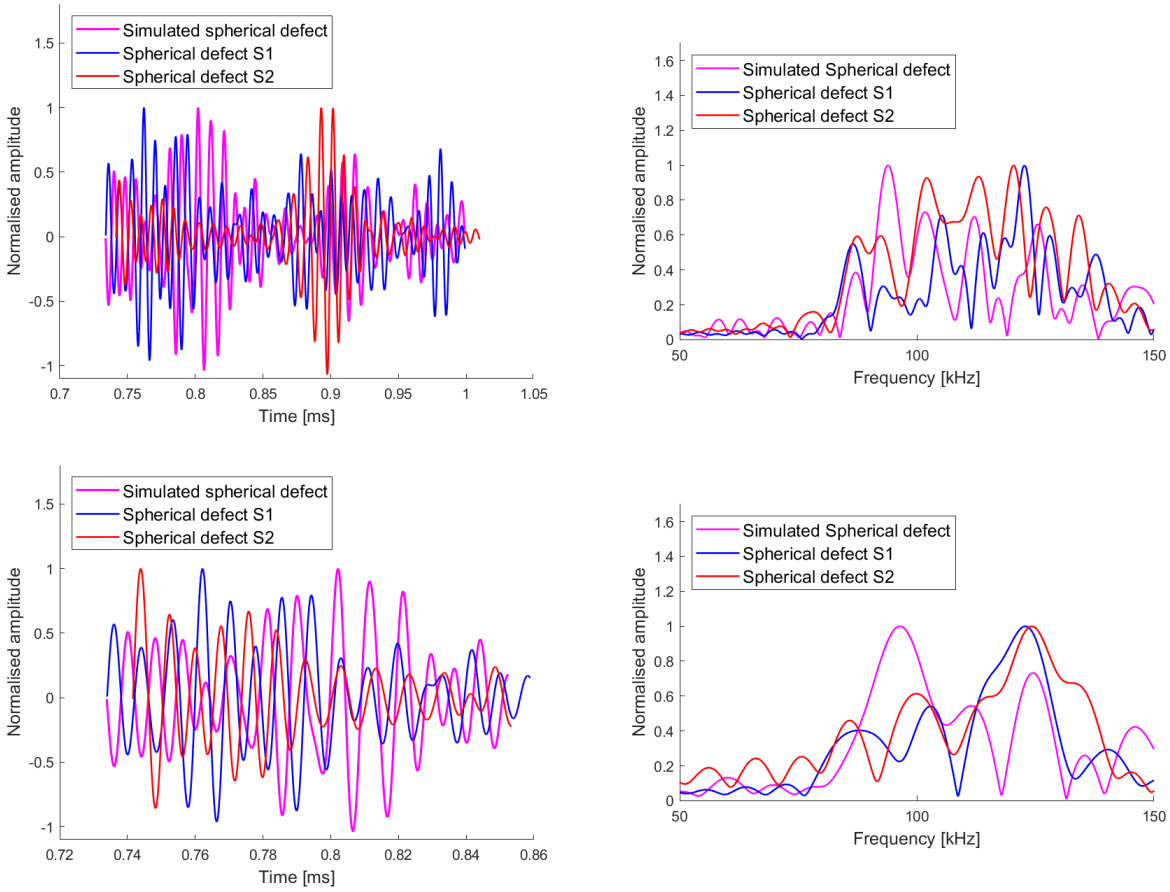

Figure 5.29: Full reverberation of the simulated experiment and experiment with spherical defects with a rectangular window and bandpass filter of 50 to 150 kHz for the experiment in the time (top left) and frequency (top right) domains and the last 500 samples in the time (bottom left) frequency (bottom right) domains

Much like in most other instances of comparing simulated and experimental data, the correlation between the experimental grout samples and the simulated grout samples with a spherical defect remains low. Given the numerous differences between the the measurement setup and simulation, the limited agreement between the simulated and experimental results is not unexpected.

Chapter 6

Conclusion and Further work

Verification of grout penetration is carried out through both simulations and experiments. The secondary pulse, originating from the rear of the grout sample, is distinctly evident in both the experimental and simulated results indicating full penetration of the grout. However, when attempting to ascertain grout penetration by detecting defects, experimental results do not provide definitive confirmation. The differences between samples with the same defect or lack thereof hampers the determination of significant distinctions between samples with defects or lack thereof. The samples with the same defect or lack thereof have large differences in response because of the variation in size and material characteristics of the grout samples.

The simulations of the spherical defect with a radius of 0.007 m have minimal differences from the simulations without a defect. This indicates that even though the spherical defect has a resonance of 102kHz it is to small compared to the wavelength to make a discernible difference. Within the simulations, discernible differences in reverberation arise between simulations with larger defects and without, indicating that under ideal conditions defects can be detected through ultrasonic NDT. The difference between the simulations are easier to ascertain with a Hamming or Hanning window as the frequency spectrum is less complex. The larger spherical defect is the easiest to detect, even though the cylindrical defect is larger in size. The Hamming or Hanning window also makes the frequency tops for the simulation of the grout without defect coincide with the compressional wave thickness resonance for the grout.

Examining simulations where a steel plate covers the front of the grout reveals minimal differences between simulations with defects or lack thereof. The use of a Hamming or Hanning window does increase the differences minimally, however the differences are still minor. The limited difference among different simulations implies the steel plate dominates the reverberation. Additionally, there is a noticeable drop of grout penetration when a steel plate covers it, as evidenced by the absence of discernible backside reflections.

Further investigations into simulations featuring steel plates positioned both in front of and behind the grout unveil greater differences compared to simulations where only a steel plate is positioned in front of the grout. This discrepancy suggests the presence of at least some level of grout penetration. Nevertheless, the differences between the simulations containing spherical defects and without defects are minimal. The simulation with cylindrical defect and without defect have a noticeable difference around 95kHz. However the differences between the simulations are negligible compared to the samples with the same defects or lack thereof in the experimental part.

There exist multiple discrepancies between the execution of the simulation and the experiment. The simulation utilises a basic baffled piston model instead of a transducer with electronics. Notably, the electronics operate beyond their intended bandwidth, resulting in distortion of the input pulse to the transducer. Furthermore, the simulation is carried out within the COMSOL 2D-axisymmetric model, leading to the representation of cylindrical grout instead of rectangular grout. These differences contribute to significant deviations between the simulation and experimental results, making it extremely challenging to establish the validity of the simulations.

6.1 Further work

Exploring whether there are variations in the reverberation of grout samples with identical dimensions and density is a point of interest. This can be accomplished by crafting grout samples using multiple rigid molds, all of which have the exact same dimensions.
Employing multiple identical molds enables the creation of uniform grout in a single batch, thereby ensuring consistent grout characteristics and minimising differences among samples with or without defects. Another aspect of investigation involves ascertaining the detectability of evolving defects on a grout sample. This could involve a gradual and

cautious introduction of defects to initially defect-free grout samples, followed by the measurement of resulting differences. Additionally, the created samples should increase in size to mitigate any potential end-effects stemming from the edges of the sample.

Moreover, there is a need for further exploration in terms of understanding and calculating resonances and scattering phenomena within defects. Another interest is to dive deeper into the reverberation characteristics and resonances of the multilayered steel-grout-steel structure and quantifying the extent of grout penetration when a steel plate is positioned at its front. It is also of interest to determine if the increase in detectability when a steel plate is added to the back of the grout is due to standing waves between the steel plates.

Bibliography

[1] N I Tziavos, H Hemida, S Dirar, M Papaelias, N Metje, and C Baniotopoulos. Structural health monitoring of grouted connections for offshore wind turbines by means of acoustic emission: An experimental study. *Renewable Energy*, 147:130–140, 3 2020.

[2] M Martinez-Luengo, A Kolios, and L Wang. Structural health monitoring of offshore wind turbines: A review through the statistical pattern recognition paradigm. *Renewable and Sustainable Energy Reviews*, 64:91–105, 10 2016.

[3] P Dallyn, A El-Hamalawi, A Palmeri, and R Knight. Experimental testing of grouted connections for offshore substructures: A critical review. *Structures*, 3:90–108, 8 2015.

[4] P Tuset, R Hansson, E Elvheim, and J Ekeborg. Assessment of methods for inspection and instrumentation of grouted connection. *Force tecnology*, 2019. `https://www.ptil.no/contentassets/cc37b1d7c8b14786b23d9b4fd575588c/sluttrapport---assessment-of-methods-for-inspection-and-instrumentation-of-grouted-connection.pdf`, Accessed: 28.08.2023.

[5] I Lotsberg. Structural mechanics for design of grouted connections in monopile wind turbine structures. *Marine Structures*, 32:113–135, 7 2013.

[6] A May. Operational expenditure optimisation utilising condition monitoring for offshore wind parks. *University of Strathclyde*, 1 2016.

[7] NORSOK Standard. Design of steel structures. *Standard Norway*, 2013. `https://handle.standard.no/en/webshop/ProductCatalog/ProductPresentation/?ProductID=629300`, Accessed: 28.08.

[8] DNV. Design of offshore wind turbine structures. *DNV OFFSHORE STANDARD*, (DNV-OS-J101), 5 2013.

https://rules.dnv.com/docs/pdf/dnvpm/codes/docs/2013-02/Os-J101.pdf, Accessed: 28.08.2023.

[9] Marcus Klose, Marc Mittelstaedt, and Amol Mulve. Grouted connections - offshore standards driven by the wind industry. *The Twenty-second International Offshore and Polar Engineering Conference, Rhodes, Greece, June 2012.* https://onepetro.org/ISOPEIOPEC/proceedings/ISOPE12/All-ISOPE12/ISOPE-I-12-141/12470, Accessed: 30.08.2023.

[10] F P G Márquez, A M Tobias, J M P Pérez, and M Papaelias. Condition monitoring of wind turbines: Techniques and methods. *Renewable Energy*, 46:169–178, 10 2012.

[11] M Shafiee and J Dalsgaard Sørensen. Maintenance optimization and inspection planning of wind energy assets: Models, methods and strategies. *Reliability Engineering System Safety*, 192:105993, 12 2019.

[12] A N Iliopoulos, D Van Hemelrijck, J Vlassenbroeck, and D G Aggelis. Assessment of grouted samples from monopile wind turbine foundations using combined non-destructive techniques. *Construction and Building Materials*, 122:855–862, 9 2016.

[13] C R Brett, D A Gunn, B AJ Dashwood, S J Holyoake, and P B Wilkinson. Development of a technique for inspecting the foundations of offshore wind turbines. *Insight: Non-Destructive Testing and Condition Monitoring*, 60:19–27, 1 2018.

[14] Sverre Finstad. Personal communication. August 30, 2023.

[15] A E Weyman, H Feigenbaum, J C Dillon, and S Chang. Cross-sectional echocardiography in assessing the severity of valvular aortic stenosis. *Circulation*, 52:828–834, 1975.

[16] C H Desch, D O Sproule, and W J Dawson. The detection of cracks in steel by means of supersonic waves. *The Journal of the Iron and Steel Institute*, 153:319–352, 1946.

[17] P G Newman and G S Rozycki. The history of ultrasound. *Surgical Clinics of North America*, 78:179–195, 1998.

[18] E. G. Cook and H. E. Van Valkenburg. Thickness measurement by ultrasonic resonance. *Journal of the acoustical society of America*, 27:564–569, 5 1955.

[19] W. S. Erwin. Supersonic measurement. *Steel*, page 181, 3 1945.

[20] P. Cawley and C. C. H. Guyott. The measurement of through thickness plate vibration using a pulsed ultrasonic transducer. *Journal of the acoustical society of America*, 83:623–631, 2 1988.

[21] M. de Billy. "determination of the resonance spectrum of elastic bodies via the use of short pulses and fourier transform theory. *Journal of the acoustical society of America*, 79:219–221, 2 1986.

[22] S. K. Numrich, N. H. Dale, and L. R. Dragonene. Generation and exploitation of plate waves in submerged, air-filled shells. *The American Society of Mechanical Engineers*, 64:59–74, 1984.

[23] S Lukasz. Difference between implicit vs explicit analysis. *Enterfea*, 10 2019. `https://enterfea.com/implicit-vs-explicit/`, Accessed: 24-08-2023.

[24] Per Lunde. Theoretical acoustics notes phys374, chapter 5. *University of Bergen*, 2016.

[25] S Rao D J Ewins and S G. Braun. *Encyclopedia of Vibration*. Academic Press, 1st edition, 2001.

[26] L E Kinsler, A R Frey, A B Coppens, and J V Sanders. *Fundamentals of Acoustics*. John Wiley & Sons, Inc, 4th edition, 2000.

[27] T M Loganathan, M T H Sultan, and M K Gobalakrishnan. *11 - Ultrasonic inspection of natural fiber-reinforced composites*. Woodhead Publishing, 2018.

[28] Britannica. Density chemistry and physics. *The Editors of Encyclopaedia Britannica*, 7 7 2023. `https://www.britannica.com/science/density`, Accessed: 28.08.2023.

[29] T Boonyatee, K-H Chan, and T Mitachi. Determination of shear wave velocity by bender elements using variable-path length method. *Soils and Foundations*, 49:489–494, 2009.

[30] L M Brekhovskikh, Y P Lysanov, and J P Lysanov. *Fundamentals of ocean acoustics*. Springer Science & Business Media, 3rd edition, 2003.

[31] L J Gelius. Introduction to seismic processing and imaging. *University of Oslo*, 2007. `https://docplayer.net/21060040-Inf-geo-3310-introduction-to-seismic-processing-and-imaging-copyright-leiv-j-gelius-geoclass-2007.html`, Accessed: 28.08.2023.

[32] Peter M Shearer. *Introduction to Seismology*. Cambridge: Cambridge University Press, 3rd edition, 2019.

[33] X Lurton. *An Introduction to Underwater Acoustics: Principles and Applications*. Springer-Verlag Berlin and Heidelberg GmbH Co. K, 2nd edition, 2010.

[34] Iowa State University. Reflection and transmission coefficients. *Center for nondestructive evaluation*, 2021. https://www.nde-ed.org/Physics/Waves/reflectiontransmission.xhtml, Accessed: 28.08.2023.

[35] Iowa State University. Wave interaction or interference. *Center for nondestructive evaluation*, 2021. https://www.nde-ed.org/Physics/Waves/WaveInterference.xhtml, Accessed: 28.08.2023.

[36] M Vestrheim. *Akustiske Transdusere (PHYS272) forelesningsnotater*. University of Bergen, 2013.

[37] M Campo-Valera, R Asorey-Cacheda, I Rodríguez-Rodríguez, and I Villó-Pérez. Characterization of a piezoelectric acoustic sensor fabricated for low-frequency applications: A comparative study of three methods. *Sensors (Basel, Switzerland)*, 23, 3 2023.

[38] AIRMAR. Understanding transducer specifications. *AIRMAR Technology Corporation*, 5 2010. https://airmartechnology.com/uploads/brochures/xducer_specifications_pc_rA_lr.pdf, Accessed: 28.08.2023.

[39] H Shekhani. Parameters to measure in ultrasonic transducer impedance analysis. *Ultrasonic Advisors*, 10 2022. https://www.youtube.com/watch?v=4qUYmYwpCBQ, Accessed: 28.08.2023.

[40] COMSOL Multiphysics. The finite element method (FEM), 2 2017. https://www.comsol.com/multiphysics/finite-element-method, Accessed: 28.08.2023.

[41] COMSOL Multiphysics. Comsol multiphysics reference manual, 2019. https://doc.comsol.com/5.5/doc/com.comsol.help.comsol/COMSOL_ReferenceManual.pdf, Accessed: 28.08.2023.

[42] COMSOL Multiphysics. Acoustics module user's guide. *Multiphysics Cyclopedia*, 2021. https://doc.comsol.com/6.0/doc/com.comsol.help.aco/AcousticsModuleUsersGuide.pdf, Accessed: 30.07.2023.

[43] Iowa State University. Wavelength and defect detection. *Center for nondestructive evaluation*, 2021. `https://www.nde-ed.org/Physics/Waves/defectdetect.xhtml`, Accessed: 28.08.2023.

[44] A L Anderson and L D Hampton. Acoustics of gas-bearing sediments 1. background. *The Journal of the Acoustical Society of America*, 67:1865–1889, 6 1980.

[45] Y Zhang, Y Petrov, and Y P Zhao. Mode localization and eigenfrequency curve veerings of two overhanged beams. *Micromachines*, 12, 3 2021.

[46] A L Anderson and L D Hampton. Acoustics of gas-bearing sediments. 2. measurements and models. *The Journal of the Acoustical Society of America*, 67:1890–1903, 6 1980.

[47] R. L. Crane, J. Hart-Smith, and J. Newman. *8 - Nondestructive inspection of adhesive bonded joints*. Woodhead Publishing, 2nd edition, 2021.

[48] Yuning Zhang and Shengcai Li. Acoustical scattering cross section of gas bubbles under dual-frequency acoustic excitation. *Ultrasonics Sonochemistry*, 26:437–444, 2015.

[49] H Medwin and C S Clay. *Fundementals of Acoustical Oceanography, Applications of Modern Acoustics*. Academic Press, 1988.

[50] Michael A. Ainslie and Timothy G. Leighton. Review of scattering and extinction cross-sections, damping factors, and resonance frequencies of a spherical gas bubble. *The Journal of the Acoustical Society of America*, 130(5):3184–3208, 11 2011.

[51] T P Philippidis and D G Aggelis. Experimental study of wave dispersion and attenuation in concrete. *Ultrasonics*, 43:584–595, 2005.

[52] Z Tian, L Huo, W Gao, H Li, and G Song. Modeling of the attenuation of stress waves in concrete based on the rayleigh damping model using time-reversal and pzt transducers. *Smart Materials and Structures*, 26:105030, 9 2017.

[53] W van Drongelen. *Signal processing for neuroscientists: introduction to the analysis of physiological signals*. Academic Press, 2007.

[54] J P Bentley. *Principles of measurement systems*. Pearson/Prentice Hall, 4th edition, 2005.

[55] D Sundararajan. *Digital Signal Processing: An Introduction*. Springer International Publishing AG, 2021.

[56] MATLAB. Matlab mathematics, fast fourier transform. *MathWorks*. https://www.mathworks.com/help/matlab/ref/fft.html, Accessed: 20.07.2023.

[57] National Instruments. Understanding ffts and windowing. *Instrument Fundamentals*. https://download.ni.com/evaluation/pxi/Understanding%20FFTs%20and%20Windowing.pdf, Accessed: 5.08.2023.

[58] MATLAB. Signal processing toolbox, hamming window. *MathWorks*. https://www.mathworks.com/help/signal/ref/hamming.html, Accessed: 28.08.2023.

[59] MATLAB. Signal processing toolbox, hann (hanning) window. *MathWorks*. https://www.mathworks.com/help/signal/ref/hann.html, Accessed: 28.08.2023.

[60] OMICRON Lab. User manual for bode 100 and bas 3.25. *OMICRON Electronics*, 2021. https://www.omicron-lab.com/fileadmin/assets/Bode_100/Manuals/Bode-100-User-Manual-ENU10060508.pdf, Accessed: 28.08.2023.

[61] OMICRON Lab. Bode 100 - vector network analyzer. *OMICRON LAB*, 2023. https://www.omicron-lab.com/products/vector-network-analysis/bode-100#, Accessed: 28.08.2023.

[62] D P Massa. Understanding how frequency, beam patterns of transducers, and reflection characteristics of targets affect the performance of ultrasonic sensors overview of how an ultrasonic sensor functions. *Massa Products Corporation*. https://www.massa.com/wp-content/uploads/2018/06/Massa-Whitepaper-3-DPM-160621.pdf, Accessed: 24-08-2023.

[63] P Pal. Dynamic poisson's ratio and modulus of elasticity of pozzolana portland cement concrete. *International Journal of Engineering and Technology Innovation*, 9:131–144, 2019.

[64] R Yue X Sun D H S Zou, J Cheng. Grout quality and its impact on guided ultrasonic waves in grouted rock bolts. *Journal of Applied Geophysics*, 72:102–106, 10 2010.

[65] Y Zhang, B Cao, H Zhang, X Zhang, and Y He. Study on key mechanical parameters of high-strength grouting material. *Coatings*, 13, 2023.

[66] S Anandan, V M Sounthararajan, and A Sivakumar. Ultrasonic tests on setting properties of cementitious systems. *ARPN Journal of Engineering and Applied Sciences*, 7:1424–1435, 11 2012.

[67] H M Tavossi, F Cohen-Tenoudji, and B R Tittmann. Ultrasonic characterization of cement and concrete. *Iowa State University Digital Repository*, 1 1999. https://core.ac.uk/download/pdf/38895996.pdf, Accessed: 28.08.2023.

[68] R N Swamy. Dynamic poisson's ratio of portland cement paste, mortar and concrete. *Cement and Concrete Research*, 1:559–583, 1971.

[69] S George Kell. Density, thermal expansivity, and compressibility of liquid water from 0" to 150°c: Correlations and tables for atmospheric pressure and saturation reviewed and expressed on 1968 temperature scale. *Journal of Chemical and Engineering Data*, 2:97, 1975.

[70] COMSOL Multiphysics. Comsol multiphysics refrence manual. *Multiphysics Cyclopedia*, pages 457–459, 2019. https://doc.comsol.com/5.5/doc/com.comsol.help.comsol/COMSOL_ReferenceManual.pdf, Accessed: 28.08.2023.

[71] J Burkardt. Department of scientific computing, meshing for the finite element method. *Florida State University*, 7 2012. https://people.sc.fsu.edu/~jburkardt/presentations/mesh_2012_fsu.pdf, Accessed: 28.08.2023.

[72] COMSOL Multiphysics. Comsol multiphysics refrence manual. *Multiphysics Cyclopedia*, pages 616–687, 2019. https://doc.comsol.com/5.5/doc/com.comsol.help.comsol/COMSOL_ReferenceManual.pdf, Accessed: 28.08.2023.

[73] K O Friedrichs and H Lewy R Courant. On the partial difference equations of mathematical physics. *IBM Journal*, 11:215–234, 1956.

[74] M H Jensen. Introduction to the elastic waves, time explicit interface. *COMSOL Blog*, 5 2020. https://www.comsol.com/blogs/introduction-to-the-elastic-waves-time-explicit-interface/, Accessed: 20.08.2023.

[75] C Chisari, C Guarnaccia, and G Rizzano. Numerical simulation of acoustic emission activity in reinforced concrete structures by means of finite element modelling at the macroscale. *Structural Health Monitoring*, 19:147592171985683, 7 2019.

Appendices

Appendix A

Calculations for reflection coefficient for fluid–solid interface

Klassisk

$$R^{PP}_{Tzz} = \frac{A_1^-}{A_1^+} = \frac{\rho_2 c_2 - \rho_1 c_1}{\rho_1 c_1 + \rho_2 c_2} = \frac{7850 \cdot 5100 - 1000 \cdot 1481}{1000 \cdot 1481 + 7850 \cdot 5100} = 0{,}9287 \qquad \theta_{L2} = 0$$

Steel : $\rho_s = 7850$ $c_s = 5100$ $\rho_w = 1000$ $c_w = 1481$

Fluid - fast Refleksjons koeffisient

h_n - bølgetall for P-bølge $= \frac{\omega}{c_{Ln}}$, $c_{Ln} = \sqrt{\frac{\lambda + 2\mu_n}{\rho_n}}$ - lydhastighet for P-bølge

k_n - bølgetall for SV-bølge $= \frac{\omega}{c_{tn}}$, $c_{tn} = \sqrt{\frac{\mu}{\rho_n}}$ - lydhastighet for SV-bølge

$h_n^2 = h_{xn}^2 + h_{zn}^2$ $\quad k_n^2 = k_{xn}^2 + k_{zn}^2$ $\quad x$-horisontal del $\quad z$-vertikal del

μ - skjær viskositet ($=0$ for fluid) $\quad \eta = \frac{\omega}{c_{L1}} \sin\theta_{L1} = \frac{\omega}{c_{t1}} \sin\theta_{t1} = \cdots = h_{x1} = k_{x1} = \cdots$

$$\varphi = \left(A^+ e^{ih_{z}z} + A^- e^{-ih_{z}z}\right) e^{i(\eta x - \omega t)} \qquad \psi_y = \left(B^+ e^{ih_{z}z} + B^- e^{-ih_{z}z}\right) e^{i(\eta x - \omega t)}$$

For fluid $\mu = 0 \rightarrow u_t = 0 \rightarrow \psi = 0 \rightarrow \psi_y = 0 \rightarrow B^+ = B^- = 0$

$$u_x = \left[i\eta\left(A^+ e^{ih_z z} + A^- e^{-ih_z z}\right) - ik_z\left(B^+ e^{ik_z z} - B^- e^{-ik_z z}\right)\right] e^{i(\eta x - \omega t)}$$

$$u_z = \left[ih_z\left(A^+ e^{ih_z z} - A^- e^{-ih_z z}\right) + i\eta\left(B^+ e^{ik_z z} + B^- e^{-ik_z z}\right)\right] e^{i(\eta x - \omega t)}$$

$$T_{zz} = \mu\left[(2\eta^2 - k^2)\left(A^+ e^{ih_z z} + A^- e^{-ih_z z}\right) - 2\eta k_z\left(B^+ e^{ik_z z} - B^- e^{-ik_z z}\right)\right] e^{i(\eta x - \omega t)}$$

$$T_{xz} = -\mu\left[2\eta h_z\left(A^+ e^{ih_z z} - A^- e^{-ih_z z}\right) + \left(2\eta^2 - k^2\right)\left(B^+ e^{ik_z z} + B^- e^{-ih_z z}\right)\right] e^{i(\eta x - \omega t)}$$

Fluid

$$u_x = i\eta\varphi - ik_z\psi \xrightarrow{\psi = 0} u_x = i\eta\varphi = i\eta\left(A^+ e^{ih_z z} + A^- e^{-ih_z z}\right) e^{i(\eta x - \omega t)}$$

$$u_z = ih_z\varphi + i\eta\psi \xrightarrow{\psi = 0} u_z = ih_z\varphi = ih_z\left(A^+ e^{ih_z z} - A^- e^{-ih_z z}\right) e^{i(\eta x - \omega t)}$$

$$T_{zz} = \mu\left[(2\eta^2 - k^2)\varphi - 2\eta k_z(\psi)\right] \xrightarrow{\psi = 0} T_{zz} = \mu\left(2\eta^2 - k^2\right)\varphi = (-\rho\omega^2)\varphi$$

$$T_{xz} = -\mu\left[2\eta h_z(\varphi) + \left(2\eta^2 - k^2\right)\psi\right] \xrightarrow[\psi = 0]{\mu = 0} T_{xz} = 0$$

$U_{x,1} = U_{x,2}$ $\quad U_{z,1} = U_{z,2}$ $\quad T_{zz,1} = T_{zz,2}$ $\quad T_{xz,1} = T_{xz,2}$

$B_1^{+/-} = 0$ - fluid

$\mu_1 = 0$ - fluid

$$i\eta\left(A_1^+ + A_1^-\right) = i\eta A_2^+ - ik_{z2} B_2^+$$

$$ih_{z1}\left(A_1^+ - A_1^-\right) = ih_{z2} A_2^+ + i\eta B_2^+$$

Fluid $\quad -\rho_{0,1}\omega^2$

$$\mu_1\left(2\eta^2 - k_1^2\right)\left(A_1^+ + A_1^-\right) = \mu_2\left(2\eta^2 - k_2^2\right)A_2^+ - \mu_2 2\eta k_{z2} B_2^+$$

Fluid $\quad 0 \quad -\rho\omega^2 \quad 0$

$$\mu_1 2\eta h_{z1}\left(A_1^+ - A_1^-\right) + \mu_1\left(2\eta^2 - k_1^2\right)\left(B_1^+ + B_1^-\right) = \mu_2 2\eta h_{z2} A_2^+ + \mu_2\left(2\eta^2 - k_2^2\right)B_2^+ = 0$$

$$h_{z1}\left(A_1^+ - A_1^-\right) = h_{z2} A_2^+ + \eta B_2^+$$

$$-\rho_{0,1}\omega^2\left(A_1^+ + A_1^-\right) = \mu_2\left(2\eta^2 - k_2^2\right)A_2^+ - \mu_2 2\eta k_{z2} B_2^+$$

$$\mu_2 2\eta h_{z2} A_2^+ + \mu_2\left(2\eta^2 - k_2^2\right)B_2^+ = 0$$

$$\begin{bmatrix} -h_{z1} & -h_{z2} & -\eta \\ -\rho_{0,1}\omega^2 & -\mu_2(2\eta^2-k_2^2) & 2\mu_2\eta k_{z2} \\ 0 & -2\mu_2\eta h_{z2} & -\mu_2(2\eta^2-k_2^2) \end{bmatrix} \begin{bmatrix} A_1^- \\ A_2^+ \\ B_2^+ \end{bmatrix} = \begin{bmatrix} -h_{z1}A_1^+ \\ \rho_{0,1}\omega^2 A_1^+ \\ 0 \end{bmatrix}$$

$A_1^+ = 1$

$$-h_{z1}A_1^- - h_{z2}A_2^+ - \eta B_2^+ = -h_{z1}A_1^+$$

$$-\rho_{0,1}\omega^2 A_1^- - \mu_2(2\eta^2-k_2^2)A_2^+ + 2\mu_2\eta k_{z2}B_2^+ = \rho_{0,1}\omega^2 A_1^+$$

$$-2\mu_2\eta h_{z2}A_2^+ - \mu_2(2\eta^2-k_2^2)B_2^+ = 0$$

$$-h_{21} A_1^- - h_{22} A_2^+ - \eta B_2^+ = -h_{21} A_1^+$$

$$-\rho_{0,1} \omega^2 A_1^- - \mu_2 (2\eta^2 - k_2^2) A_2^+ + 2\mu_2 \eta k_{z2} B_2^+ = \rho_{0,1} \omega^2 A_1^+$$

$$-2\mu_2 \eta h_{22} A_2^+ - \mu_2 (2\eta^2 - k_2^2) B_2^+ = 0$$

$$-2\mu_2 \eta h_{22} A_2^+ - \mu_2 (2\eta^2 - k_2^2) B_2^+ = 0$$

$$B_2^+ = \frac{-2\mu_2 \eta h_{22} A_2^+}{\mu_2 (2\eta^2 - k_2^2)}$$

$$-\rho_{0,1} \omega^2 A_1^- - \mu_2 (2\eta^2 - k_2^2) A_2^+ + 2\mu_2 \eta k_{z2} B_2^+ = \rho_{0,1} \omega^2 A_1^+$$

$$-\rho_{0,1} \omega^2 A_1^- - \mu_2 (2\eta^2 - k_2^2) A_2^+ + 2\mu_2 \eta k_{z2} \frac{-2\mu_2 \eta h_{22} A_2^+}{\mu_2 (2\eta^2 - k_2^2)} = \rho_{0,1} \omega^2$$

$$-\mu_2\left(2\eta^2-k_2^2\right)A_2^+ - \frac{4\mu_2\eta^2 k_{z2}h_{22}}{\left(2\eta^2-k_2^2\right)}A_2^+ = \rho_{o,1}\omega^2 + \rho_{o,1}\omega^2 A_1^-$$

$$A_2^+\left(-\mu_2\left(2\eta^2-k_2^2\right) - \frac{4\mu_2\eta^2 k_{z2}h_{22}}{\left(2\eta^2-k_2^2\right)}\right) = \rho_{o,1}\omega^2 + \rho_{o,1}\omega^2 A_1^-$$

$$A_2^+ = \frac{\rho_{o,1}\omega^2 + \rho_{o,1}\omega^2 A_1^-}{-\mu_2\left(2\eta^2-k_2^2\right) - \frac{4\mu_2\eta^2 k_{z2}h_{22}}{\left(2\eta^2-k_2^2\right)}}$$

$$H = \left(2\eta^2-k_2^2\right) \qquad G = \frac{\rho_{o,1}\omega^2}{-\mu_2\left(2\eta^2-k_2^2\right) - \frac{4\mu_2\eta^2 k_{z2}h_{22}}{\left(2\eta^2-k_2^2\right)}}$$

$$-h_{21}A_1^- - h_{22}\frac{\rho_{o,1}\omega^2 + \rho_{o,1}\omega^2 A_1^-}{-\mu_2\left(2\eta^2-k_2^2\right) - \frac{4\mu_2\eta^2 k_{z2}h_{22}}{\left(2\eta^2-k_2^2\right)}} - \eta\frac{-2\eta h_{22}}{\left(2\eta^2-k_2^2\right)}\frac{\rho_{o,1}\omega^2 + \rho_{o,1}\omega^2 A_1^-}{-\mu_2\left(2\eta^2-k_2^2\right) - \frac{4\mu_2\eta^2 k_{z2}h_{22}}{\left(2\eta^2-k_2^2\right)}} = -h_{21}A_1^+$$

$$-h_{21}A_1^- - h_{22}GA_1^- - h_{22}G + \frac{2\eta^2 h_{22}}{H}GA_1^- + \frac{2\eta^2 h_{22}}{H}G = -h_{21}$$

$$A_1^-\left(-h_{21} - h_{22}G + \frac{2\eta^2 h_{22}}{H}G\right) = -h_{21} + h_{22}G - \frac{2\eta^2 h_{22}}{H}G$$

$$A_1^- = \frac{-h_{21} + h_{22}G - \frac{2\eta^2 h_{22}}{H}G}{-h_{21} - h_{22}G + \frac{2\eta^2 h_{22}}{H}G}$$

Appendix B

MATLAB Beam pattern code

B.1 The code that runes the different functions and plot the beampattern

```
[Tv1,Tv2,Tv3,Tv4]=hentdata_text(); % Reads the data from files in
   ↪ function "hentdata_text"
c0=1481; % Sound velocity in water
f0=50000; % Innput frequency
lamda=c0/f0; % Wavelength
a=0.1; % Transducer radius
S=pi*a^2; % Transducer surface
Ray_length=S/lamda; % Rayleigh length


for iq=1:4 % Prosesses one file at the time
    if iq==1
        data=Tv1; % Prosseses file 1
        [beam,theta,beam_anaf,S,m,z]=Prove_fft_matlab(data); % Runs
           ↪ function Prove_fft_matlab
        Ray=z(1)/Ray_length; % Determine how many Rayleigh lengths the
           ↪ radius corrisponds to
%         figure
        % Plotting of the results
        polarplot(theta,20*log10(beam_anaf),'m','Linewidth',1.2)
        hold on
        polarplot(-theta,20*log10(beam_anaf),'m')
        polarplot(theta,20*log10(beam./beam(1)),'r','Linewidth',1.2)
        polarplot(-theta,20*log10(beam./beam(1)),'r','Linewidth',1.2)

%         Plot data for when file 1 is plotted alone
%         polarplot(theta(1,m),20*log10(beam(1,m)./beam(1)),'*')
%         polarplot(-theta(1,m),20*log10(beam(1,m)./beam(1)),'*')
%         ax = gca()
%         ax.ThetaZeroLocation= 'top';
%         ax.ThetaLim = [-90, 90]
%         rlim([-60,5])
%         rticks(-60:10:2)
%         legend('Analytisk','','Simulert')
        % legend('Analytisk','','1%','','10%','','100%','','1000%')
        % legend('Analytisk','','50Khz 1000%','','max frekvens
           ↪ 1%','','max frekvens 1000%','','')
```

```
%         title('MATLAB FFT + egen kode '+string(z(1))+'m Ray lengder
    ↪ '+string(Ray))
%         hold off
%         m=[];
        c=[z(1)];
        R=[Ray];
    elseif iq==2 % Repeat for file 2
        data=Tv2;
        [beam,theta,beam_anaf,S,m,z]=Prove_fft_matlab(data);
        Ray=z(1)/Ray_length;
%         figure
%         polarplot(theta,20*log10(beam_anaf),'m')
%         hold on
%         polarplot(-theta,20*log10(beam_anaf),'m')
        polarplot(theta,20*log10(beam./beam(2)),'c','Linewidth',1.2)
        polarplot(-theta,20*log10(beam./beam(2)),'c','Linewidth',1.2)
%         polarplot(theta(1,m),20*log10(beam(1,m)./beam(1)),'*')
%         polarplot(-theta(1,m),20*log10(beam(1,m)./beam(1)),'*')
%         ax = gca()
%         ax.ThetaZeroLocation= 'top';
%         ax.ThetaLim = [-90, 90]
%         rlim([-60,5])
%         rticks(-60:10:2)
%         legend('Analytisk','','Simulert')
%         % legend('Analytisk','','1%','','10%','','100%','','1000%')
%         % legend('Analytisk','','50Khz 1000%','','max frekvens
    ↪ 1%','','max frekvens 1000%','','')
%         title('MATLAB FFT + egen kode '+string(z(1))+'m Ray lengder
    ↪ '+string(Ray))
%         hold off
%         m=[];
        c=[c,z(1)];
        R=[R,Ray];
    elseif iq==3 % Repeat for file 3
        data=Tv3;
        [beam,theta,beam_anaf,S,m,z]=Prove_fft_matlab(data);
        Ray=z(1)/Ray_length;
%         figure
%         polarplot(theta,20*log10(beam_anaf),'m')
%         hold on
%         polarplot(-theta,20*log10(beam_anaf),'m')
```

```
72          polarplot(theta,20*log10(beam./beam(1)),'b','Linewidth',1.2)
73          polarplot(-theta,20*log10(beam./beam(1)),'b','Linewidth',1.2)
74  %         polarplot(theta(1,m),20*log10(beam(1,m)./beam(1)),'*')
75  %         polarplot(-theta(1,m),20*log10(beam(1,m)./beam(1)),'*')
76  %         ax = gca()
77  %         ax.ThetaZeroLocation= 'top';
78  %         ax.ThetaLim = [-90, 90]
79  %         rlim([-60,5])
80  %         rticks(-60:10:2)
81  %         legend('Analytisk','','Simulert')
82  %         % legend('Analytisk','','1%','','10%','','100%','','1000%')
83  %         % legend('Analytisk','','50Khz 1000%','','max frekvens
    ↪ 1%','','max frekvens 1000%','','')
84  %         title('MATLAB FFT + egen kode '+string(z(1))+'m Ray lengder
    ↪ '+string(Ray))
85  %         hold off
86  %         m=[];
87          c=[c,z(1)];
88          R=[R,Ray];
89       elseif iq==4 % Repeat for file 4
90          data=Tv4;
91          [beam,theta,beam_anaf,S,m,z]=Prove_fft_matlab(data);
92          Ray=z(1)/Ray_length;
93  %         figure
94  %         polarplot(theta,20*log10(beam_anaf),'m')
95  %         hold on
96  %         polarplot(-theta,20*log10(beam_anaf),'m')
97          polarplot(theta,20*log10(beam./beam(1)),'g','Linewidth',1.2)
98          polarplot(-theta,20*log10(beam./beam(1)),'g','Linewidth',1.2)
99  %         polarplot(theta(1,m),20*log10(beam(1,m)./beam(1)),'*')
100 %         polarplot(-theta(1,m),20*log10(beam(1,m)./beam(1)),'*')
101 %         ax = gca()
102 %         ax.ThetaZeroLocation= 'top';
103 %         ax.ThetaLim = [-90, 90]
104 %         rlim([-60,5])
105 %         rticks(-60:10:2)
106 %         legend('Analytisk','','Simulert')
107 %         % legend('Analytisk','','1%','','10%','','100%','','1000%')
108 %         % legend('Analytisk','','50Khz 1000%','','max frekvens
    ↪ 1%','','max frekvens 1000%','','')
```

```
%          title('MATLAB FFT + egen kode '+string(z(1))+'m Ray lengder
    ↪ '+string(Ray))
%          hold off
%          m=[];
         c=[c,z(1)];
         R=[R,Ray];
     end
end
% Plot innputs for all files plottet toghether
ax = gca()
ax.ThetaZeroLocation= 'top';
ax.ThetaLim = [-90, 90]
rlim([-60,5])
rticks(-60:10:2)
legend('Analytisk','','Simulert '+string(c(1))+'m','','Simulert
    ↪ '+string(c(2))+'m','','Simulert '+string(c(3))+'m','','Simulert
    ↪ '+string(c(4))+'m','FontSize',10','location','southeast')
% legend('Analytisk','','1%','','10%','','100%','','1000%')
% legend('Analytisk','','50Khz 1000%','','max frekvens 1%','','max
    ↪ frekvens 1000%','','')
title('Simulated and analytical beampattern','FontSize',14')
```

B.2 Function that uses FFT on the stationary signal

```
function [beam,theta,beam_anaf,S,m,z]=Prove_fft_matlab(Tv1)
f0=50000; % input frequency
samples_T=200; % samples per period
Fs=1/(1/f0/samples_T); % sampling frequency
startperiode=4; % Starting at period 4
k=0; % defines k for use later
beam=[]; % defines beam for use later
m=[]; % defines m for use later
samplelength=30; % Desired sample length
T=Tv1; % Renames input data
avvikamplitude=10; % Deviation of the maximum amplitude per period in
    ↪ procent (10%)

for i=1:height(T)
    I=samples_T*startperiode+3; %starter periode
    S=[find_stat(T(i,:),samples_T,f0,I,avvikamplitude,samplelength)]; %
        ↪ Run find_stat to find a sample in the stationary part
    Sa=[S,zeros(1,2^17-length(S))];
    if width(S)<samplelength*samples_T %The sample length is shorter then
        ↪ the desired sample (samplelength)
        while width(S)<samplelength*samples_T % continnues as long as the
            ↪ signal is longer then the desired sample
            k=k+1;
            I=I+k*samples_T; % Starting on the next period to get propper
                ↪ length with right deviation
            S=[find_stat(T(i,:),samples_T,f0,I,avvikamplitude,samplelength)];
                ↪ % Run find_stat again
            if I>=width(T)-(startperiode+3)*samples_T
                I=samples_T*startperiode+3;
                k=0;
                break
            end
            I=samples_T*startperiode+3; % Changing start period back to
                ↪ original
        end
        I=samples_T*startperiode+3; % Changing start period back to
            ↪ original
    end
```

```
31      if width(S)<samplelength*samples_T %If the sample length is long
            ↪ enough it continues
32          m=[m,i];
33      end
34      %FFT of the sample
35      Ls = width(Sa);% Signal length
36      F = fft(Sa);% Calling fft() function for signal
37      PS2 = abs(F/Ls);% Double sampling plot
38      PS1 = PS2(:,1:Ls/2+1);% Single sampling plot
39      PS1(2:end-1) = 2*PS1(2:end-1);
40      f = Fs*(0:(Ls/2))/Ls;
41      fI=f-Fs;
42      [v,If]=(min(abs(fI)));
43      PS=PS1(If);
44      beam=[beam,PS];
45  end
46  % Converting from r,z cordinates to angles
47  r=(T(:,1))';
48  z=(T(:,2))';
49  theta=atan(r./z);
50
51  % the analytical beam pattern
52  a=0.1;
53  c0=1481;
54  q=2*pi*f0/c0;
55  omega=2*pi*f0;
56  v=q.*a.*sin(theta);
57  beam_anaf=abs(2*besselj(1,v)./v);
58  end
```

B.3 Function that finds the stationary part of the signal

```
%Finding the stationary part of the signal

function signal=find_stat(data,samples_T,f0,I,
    ↪ avvikamplitude,samplelength)
sample=1/f0/samples_T; % Period devided by samples per period (how long 1
    ↪ sample is)
sampleu=round(samples_T/4); % Start in the beggining of a period
sampleo=round(3*samples_T/4); % End in the end of a period
T0=1/f0; % Period
Tn=T0/sample; % Period devided by samples per period (how long 1 sample
    ↪ is)
Ip=I; % Start period
[a,Ia]=max(data(1,round(Ip-samples_T/2):round(Ip+samples_T/2))); %find
    ↪ the max value in the period
Ij=Ia+Ip; % End of period
Iz=Ij-Ip; % Start of period
start=(data(1,Ij)); % Start amplitude
S=(data(1,Ij-sampleu:Ij+sampleo)); %f rste periode

% Adding periods to the S as long as it amplitude is within the desired
    ↪ deviation
    for o=1:round((length(data(1,Ij:end-3))-Iz)/Tn)
        if width(S)>samples_T*samplelength
            break
        elseif (data(1,Ij+o*Tn)) < start-start*avvikamplitude
            S=[S,data(1,Ij+Tn*o-sampleu:Ij+sampleo+o*Tn)];
        elseif (data(1,Ij+o*Tn)) < start+start*avvikamplitude
            S=[S,data(1,Ij+Tn*o-sampleu:Ij+sampleo+o*Tn)];
        else
            break
        end
    end
signal=S;
end
```

B.4 Function that reads the data from the COMSOL files

```
function [Tv1,Tv2,Tv3,Tv4]=hentdata_text() % Reads the data from the
    ↪ input filenames

filname1='fj rnfelt_1m.txt'; %filename
opts = detectImportOptions(filname1); % Determines what format the text
    ↪ file has
T1=readtable(filname1,opts,'ReadVariableNames', false); % Reads the data
T1=table2array(T1); % Transforms data from a table to a array
Tv1=[T1]; % Changes name to Tv1

filname1='fj rnfelt_2m.txt';
T1=readtable(filname1,opts,'ReadVariableNames', false);
T1=table2array(T1);
Tv2=[T1];


filname1='fj rnfelt_3m.txt';
T1=readtable(filname1,opts,'ReadVariableNames', false);
T1=table2array(T1);
Tv3=[T1];


filname1='fj rnfelt_4m.txt';
T1=readtable(filname1,opts,'ReadVariableNames', false);
T1=table2array(T1);
Tv4=[T1];

end
```

Appendix C

MATLAB code for Section 4.2

```
%read data
close all
clear all
filname1='aksetrykk_vann_lengremodel1_120kHz.txt';
opts = detectImportOptions(filname1);
T1=readtable(filname1,opts,'ReadVariableNames', false);
Tv1=table2array(T1);
%%
f0=120e3;
c=1481;
k=(2*pi.*f0)./c;
lam=c/f0;

sampT=60; %time samples per period
T0=1/f0;  %period

%%
Is1=1800; %sample to get distance P1
p0=Tv1(Is1,round(Tv1(Is1,2)/(lam/60)+60*5):end);
% p0=Tv1(Is1,round((Tv1(end,2)+Tv1(end,2)-Tv1(Is1,2))/(lam/60)+60*5):end);
%Gather the local maximum points
a=1:length(p0);
Im=islocalmax(p0);
Im=a(Im);
%Get complete waves
I=Im(1)-sampT/4:Im(1)+10*sampT+sampT/4;
```

```
27
28 p0_I1=p0(I); %Pressure at P1
29
30 Is2=1900; % Sample to get distance P2
31 p1=Tv1(Is2,round(Tv1(Is2,2)/(lam/60)+60*5):end); % Pressure at P2
32 % p1=Tv1(Is2,round((Tv1(end,2)+Tv1(end,2)-Tv1(Is2,2))/(lam/60)+60*5):end);
33
34 d0=Tv1(Is1,2)/Tv1(Is2,2); %Distance correction
35 % d0=(2*Tv1(end,2)-Tv1(Is1,2))/(2*Tv1(end,2)-Tv1(Is2,2));
36 %Find the index of the maximum points
37 a=1:length(p1);
38 Im1=islocalmax(p1);
39 Im1=a(Im1);
40 %Get complete waves
41 I1=Im1-sampT/4:Im1+10*sampT+sampT/4;
42
43
44 %making the time vector
45 % t=Is2:1:Is2+10*sampT;
46 t=(I+round(Tv1(Is2,2)/(lam/60)+60*5))*T0/60;
47 %Finding the pressure
48 p1_I1=p1(I1);
49 %Finding the corrected pressure
50 p1_I=p1_I1./d0.*exp(1i*(-k.*d0));
51
52 figure
53 plot(t,abs(p1_I1)./1e3,'g','linewidth',2)
54 hold on
55 plot(t,abs(p0_I1)./1e3,'b','linewidth',2)
56 plot(t,abs(p1_I)./1e3,'-.r','linewidth',2)
57 legend('P2: p at '+string(Tv1(Is2,2))+'m','P1: p at
    ↪ '+string(Tv1(Is1,2))+'m','P2 corrected to P1','Fontsize',10,
    ↪ 'location','southeast')
58 title('Geometric spreading correction of incident wave','FontSize',12)
59 % title('Gemoetric spreading correction of reflected wave', 'FontSize',12)
60
61 xlabel('time','FontSize',12)
62 ylabel('Magnitude [kPa]','FontSize',12)
63 xlim([1.92*1e-3,1.95*1e-3])
64 pbaspect([1.6,1,1])
65 saveas(gcf,'Geometric spreading correction after reflection.png')
```

Appendix D

Fluid-solid Reflection coefficient test

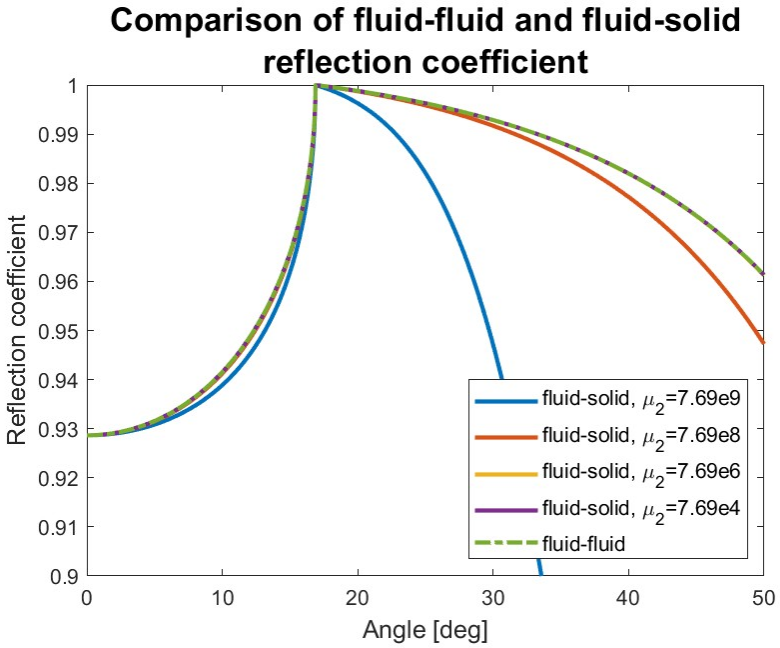

Figure D.1: Comparing the fluid-solid and fluid-fluid reflection coefficient with gradually decreasing shear viscosity in the solid medium.

Appendix E

Transit time at different angles

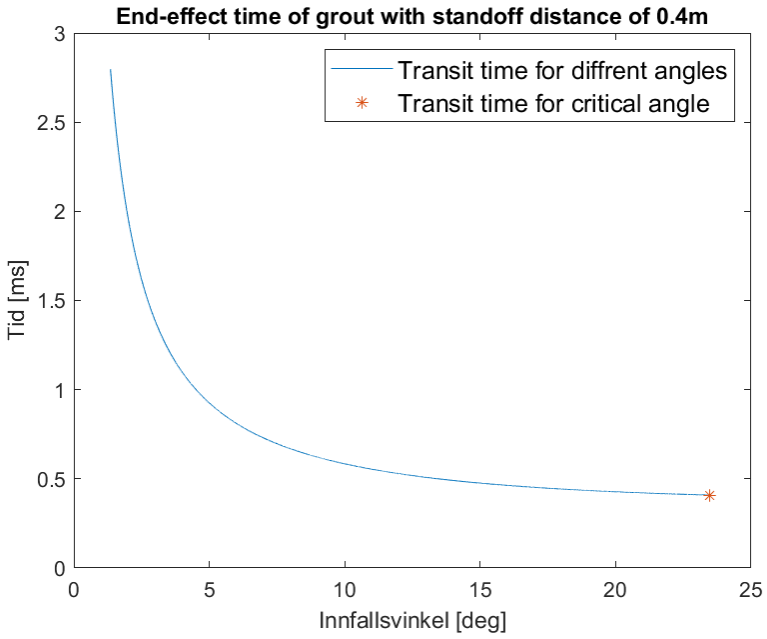

Figure E.1: Transit time at different angles

Appendix F

Material density

Snus S1	L	B	D	M	V	rho
	3.01	3.00	1.55			
	3.03	2.99	1.55			
	3.05	3.00	1.54			
	3.05	3.00	1.54			
	3.03	3.00	1.55			
	3.00	3.00	1.55			
	3.00	3.00	1.55			
	3.05	2.99	1.55			
	3.03	3.01	1.53			
	3.02	3.01	1.53			
gjennomsnitt [dm]	3.03	3.00	1.54	28.35	14.021064	2.02195782

Snus S2	L	B	D	M	V	rho
	3.01	3.00	1.56			
	3.03	3.00	1.57			
	3.03	3.01	1.55			
	3.03	3.04	1.55			
	3.02	3.04	1.55			
	3.00	3.03	1.52			
	3.00	3.05	1.52			
	3.01	3.05	1.50			
	3.02	3.03	1.51			
	3.03	3.05	1.51			
gjennomsnitt [dm]	3.02	3.03	1.53	28.10	14.0277244	2.00317594

S	T	U	V	W	X	Y
Pingpong P1	L	B	D	M	V	rho
	3.05	2.97	1.60			
	3.04	2.98	1.59			
	3.00	3.00	1.57			
	3.00	3.01	1.55			
	3.02	3.02	1.53			
	3.00	3.02	1.60			
	3.00	3.01	1.60			
	3.01	3.00	1.59			
	3.02	2.99	1.57			
	3.02	2.97	1.60			
gjennomsnitt [dm]	3.02	3.00	1.58	28.35	14.2815442	1.98507946

Pingpong P2	L	B	D	M	V	rho
	3.00	3.00	1.50			
	3.00	2.95	1.51			
	3.00	2.96	1.51			
	3.00	2.97	1.52			
	3.00	2.99	1.54			
	3.01	3.00	1.50			
	3.01	2.99	1.50			
	3.00	2.99	1.52			
	3.00	2.99	1.53			
	3.00	2.98	1.53			
gjennomsnitt [dm]	3.00	3.00	1.52	27.10	13.653096	1.98489778

Figure F.1: Measurements of size and weight of grout with Top: cylindrical defects sample 1 and 2 Bottom: spherical defects sample 1 and 2

	Betong 1	L	B	D	M	V	rho
2		3.00	2.80	1.43			
3		3.00	2.75	1.46			
4		3.01	2.75	1.50			
5		3.02	2.74	1.53			
6		3.00	2.80	1.56			
7		3.00	2.78	1.40			
8		3.00	2.75	1.42			
9		3.00	2.74	1.45			
10		3.01	2.80	1.50			
11		3.00	2.74	1.55			
12	gjennomsnitt [dm]	3.00	2.77	1.48	24.85	12.2929688	2.02148077
13							
14							
15	Betong 2	L	B	D	M	V	rho
16		3.01	2.95	1.60			
17		3.03	2.93	1.56			
18		3.03	2.92	1.55			
19		3.01	2.95	1.52			
20		3.00	2.95	1.51			
21		3.02	2.94	1.55			
22		3.03	2.93	1.52			
23		3.03	2.90	1.50			
24		3.00	2.92	1.49			
25		3.00	2.95	1.45			
26	gjennomsnitt [dm]	3.02	2.93	1.53	28.10	13.4946396	2.0823083
27							
28							
29	Betong 3	L	B	D	M	V	rho
30		3.01	3.00	1.50			
31		3.03	3.03	1.50			
32		3.04	3.05	1.51			
33		3.02	3.02	1.52			
34		3.00	3.00	1.51			
35		3.00	3.00	1.53			
36		3.05	3.00	1.54			
37		3.04	3.01	1.53			
38		3.02	3.30	1.55			
39		3.00	3.05	1.55			
40	gjennomsnitt [dm]	3.02	3.05	1.52	27.55	14.0237962	1.964518
41							
42							
43							
44	All Betong						
45	rho	2.00905972					
46							
47							
48							
49							

Figure F.2: Measurements of size and weight of grout Top: samples 1 and 2: sample 3 with total average

Appendix G

AIRMAR B175M datasheet

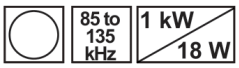

85 to 135 kHz-B (Broadband)

Transformed to 100 ohms minimum (B1)

Power Rating:
- 1 kW @ 1% duty cycle
- CW(4): 18W in B175, B265, B285, PM265
  12W in M265, TM185, TM265

65 mm (2.56 in) PZT
Active Area: 33 cm^2 (5.1 in^2)

Radiating Surface: Urethane
Q ≈ 2
Cable Type: C335
Cable Length: 10 m (33 ft)

Notes:
(1) dB re 1 µPa per volt at 1 meter
(2) dB re 1 volt per µPa
(3) Sum of transmitting voltage response and receiving voltage response
(4) CW Power ratings is for 20°C seawater temperature. Consult Airmar for different housing CW ratings.

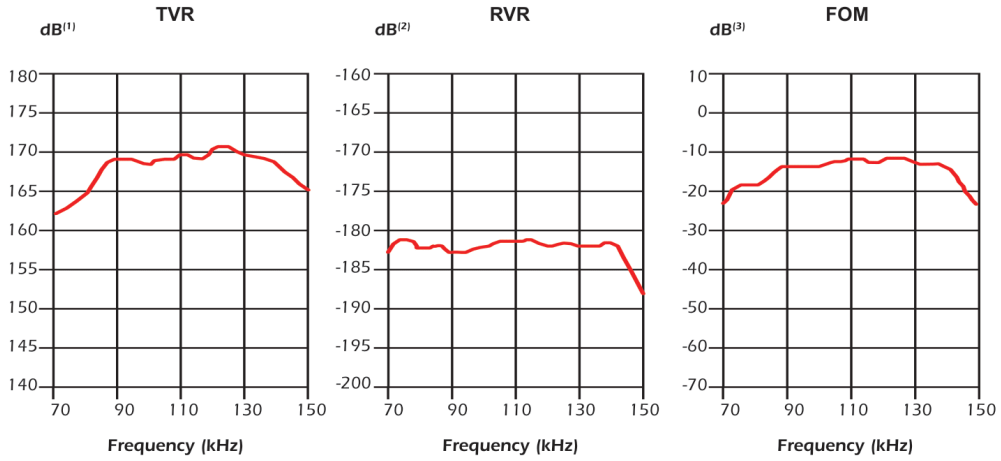

Transmit Radiation Pattern

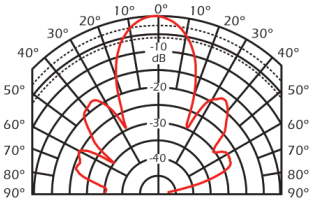

Beamwidth	@ 85 kHz
-3 dB	16°
-6 dB	22°
-10 dB	29°

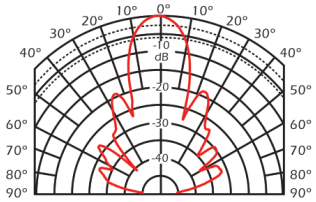

Beamwidth	@ 105 kHz
-3 dB	13°
-6 dB	18°
-10 dB	22°

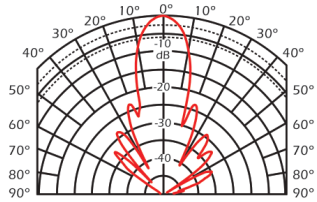

Beamwidth	@ 135 kHz
-3 dB	11°
-6 dB	15°
-10 dB	19°

AIRMAR®
TECHNOLOGY CORPORATION
Sensing Technology

Tel: 603.673.9570 • Fax: 603.673.4624 • www.airmar.com

85 to 135 kHz-B (Broadband)

Note: Impedance data includes cable

Balanced Impedance Table (Nominal Value) in 20°C Water

Test Frequency (kHz)	Impedance Magnitude (Ω)	Phase Angle (°)	Series Resistance (Ω)	Series Reactance (Ω)	Parallel Conductance (mS)	Parallel Susceptance (mS)	Parallel Resistance (Ω)	Parallel Capacitance (pF)
75.00	240.21	29.30	209.48	117.57	3.63	-2.04	275.46	-4323.59
77.00	231.70	16.69	221.94	66.54	4.13	-1.24	241.89	-2561.81
79.00	204.27	7.58	202.48	26.95	4.85	-0.65	206.07	-1301.08
81.00	183.32	3.40	182.99	10.87	5.45	-0.32	183.64	-635.29
83.00	170.03	-1.06	170.00	-3.14	5.88	0.11	170.06	208.32
85.00	150.91	-5.20	150.29	-13.67	6.60	0.60	151.54	1123.61
87.00	130.38	-5.70	129.74	-12.96	7.63	0.76	131.03	1394.63
89.00	117.20	-2.52	117.09	-5.15	8.52	0.38	117.31	670.63
91.00	111.64	3.07	111.48	5.97	8.94	-0.48	111.79	-837.83
93.00	114.06	8.14	112.91	16.15	8.68	-1.24	115.22	-2124.79
95.00	120.70	10.90	118.52	22.83	8.14	-1.57	122.92	-2625.71
97.00	130.07	12.03	127.22	27.11	7.52	-1.60	133.00	-2629.03
99.00	142.17	10.29	139.88	25.39	6.92	-1.26	144.49	-2019.20
101.00	148.32	6.09	147.49	15.73	6.70	-0.71	149.16	-1126.55
103.00	149.11	3.53	148.82	9.19	6.69	-0.41	149.39	-638.51
105.00	152.85	1.70	152.78	4.52	6.54	-0.19	152.92	-293.52
107.00	156.36	-1.39	156.31	-3.80	6.39	0.16	156.40	230.91
109.00	155.91	-3.97	155.54	-10.80	6.40	0.44	156.29	648.58
111.00	156.14	-4.98	155.55	-13.55	6.38	0.56	156.73	797.02
113.00	164.32	-5.79	163.48	-16.59	6.05	0.61	165.16	865.42
115.00	174.54	-11.92	170.77	-36.06	5.61	1.18	178.39	1638.25
117.00	164.75	-19.34	155.45	-54.57	5.73	2.01	174.60	2734.69
119.00	148.66	-20.46	139.28	-51.96	6.30	2.35	158.67	3144.64
121.00	142.19	-17.38	135.70	-42.47	6.71	2.10	148.99	2762.55
123.00	147.06	-14.66	142.28	-37.23	6.58	1.72	152.02	2227.19
125.00	157.33	-15.05	151.93	-40.86	6.14	1.65	162.92	2101.98
127.00	165.42	-17.43	157.83	-49.55	5.77	1.81	173.39	2269.18
129.00	170.32	-20.27	159.77	-59.00	5.51	2.03	181.56	2509.22
131.00	173.62	-22.89	159.96	-67.53	5.31	2.24	188.46	2721.46
133.00	177.00	-24.58	160.96	-73.63	5.14	2.35	194.64	2812.33
135.00	185.77	-25.74	167.34	-80.67	4.85	2.34	206.23	2755.77
137.00	201.62	-28.69	176.86	-96.81	4.35	2.38	229.85	2766.43
139.00	219.05	-34.90	179.66	-125.31	3.74	2.61	267.06	2990.37
141.00	229.49	-43.85	165.50	-158.98	3.14	3.02	318.22	3407.39
143.00	224.57	-54.12	131.63	-181.95	2.61	3.61	383.13	4015.33
145.00	206.22	-62.51	95.20	-182.93	2.24	4.30	446.71	4721.54

Tel: 603.673.9570 • Fax: 603.673.4624 • www.airmar.com

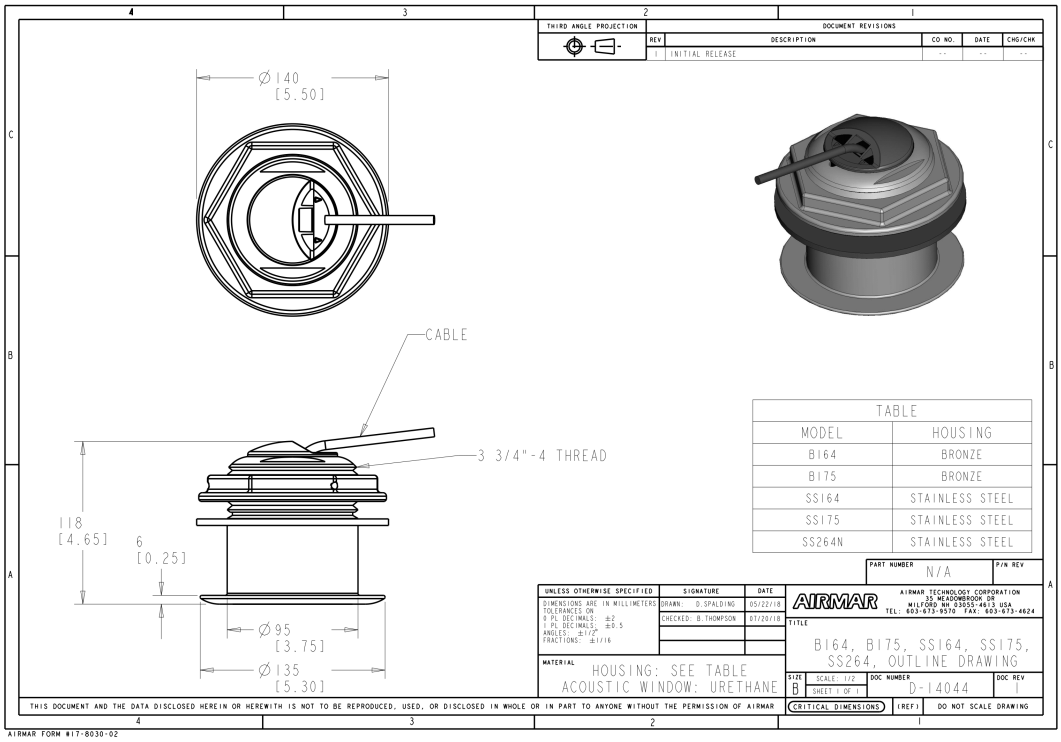

Transmitting Voltage Response

Transmitting Voltage Response (TVR) is computed using Receiving Voltage Response and Impedance. The unit of measure for TVR is dB relative to 1 micropascal per volt at a distance of 1 meter (3').

Receiving Voltage Response

Receiving Voltage Response (RVR) is measured typically by applying 200 V peak-to-peak to the transducer under test, pointing it at a nearly perfect reflector, and measuring the echo amplitude as a function of frequency. The unit of measure is dB relative to 1 Volt per micropascal.

Figure of Merit

This graph is a summation of TVR and RVR and provides a measure of two-way performance. A transducer whose figure of merit response has a wide bandwidth is generally preferred over a transducer with a narrow bandwidth. The former usually rings less and offers most consistent performance over the transducer's range of frequency tolerance.

Figure G.1: How TVR, RVR and FOM are determined

Appendix H

MATLAB code for processing the signals

```
%% Data from experiment
Tv1=0;
Tv2=0;
Tv3=0;
Tv4=0;
Tv5=0;

for i=1:20 % ShotViewer is a confedential TSC function to read the data


[delta_t,T1]=ShotViewer_Single_Shot('1_10V_betong'+string(i)+'.adm16');
% T1=T1(4040:7000)';
% T1=T1(6300:end)';
T1=double(T1)';
Tv1=Tv1+T1;

[delta_t,T2]=ShotViewer_Single_Shot('1_10V_betong'+string(i)+'.adm16');
% T2=T2(4060:7000)';
% T2=T2(6300:end)';
T2=double(T2)';
Tv2=Tv2+T2;


```

```
%
    ↪ [delta_t,T3]=ShotViewer_Single_Shot('1_10V_pingpong_tredjedel'+string(i)+'.adm16
[delta_t,T3]=ShotViewer_Single_Shot('1_10V_betong'+string(i)+'.adm16');
%
    ↪ [delta_t,T3]=ShotViewer_Single_Shot('2_10V_snus_tredjedel'+string(i)+'.adm16');
% T3=T3(4060:7000)';
% T3=T3(6300:end)';
T3=double(T3)';
Tv3=Tv3+T3;

% [delta_t,T4]=ShotViewer_Single_Shot('2_10V_betong'+string(i)+'.adm16');
[delta_t,T4]=ShotViewer_Single_Shot('1_10V_snus_tredjedel'+string(i)+'.adm16');
% T4=T4(120:end);
T4=double(T4)';
Tv4=Tv4+T4;

% [delta_t,T5]=ShotViewer_Single_Shot('3_10V_betong'+string(i)+'.adm16');
[delta_t,T5]=ShotViewer_Single_Shot('2_10V_snus_tredjedel'+string(i)+'.adm16');
% T5=T5(120:end);
T5=double(T5)';
Tv5=Tv5+T5;

end

Tv1=Tv1/20;
Tv2=Tv2/20;
Tv3=Tv3/20;
Tv4=Tv4/20;
Tv5=Tv5/20;

%% Data from Simulation
k=0;
filname1='implicit_10_riktig.txt'; % filename
opts = detectImportOptions(filname1); % detecting what format the file is
    ↪ in
T1=readtable(filname1,opts,'ReadVariableNames', false); % reading the data
Tv1=sum(table2array(T1)); % converting the data from an table to an array
    ↪ and suming
Tv1b=Tv1(:,3255+k:end-320-k); % extracting the reveberation of the signal

% repeat for the other filenames
```

```
filname2='spherical_implicit_10_riktig.txt';
opts = detectImportOptions(filname2);
T2=readtable(filname2,opts,'ReadVariableNames', false);
Tv2=sum(table2array(T2));
Tv2b=Tv2(:,3255+k:end-320);

filname3='cylinder_implicit_riktig.txt';
opts = detectImportOptions(filname3);
T3=readtable(filname3,opts,'ReadVariableNames', false);
Tv3=sum(table2array(T3));
Tv3b=Tv3(:,3255+k+653:end-320);


% filname4='implicit_uten_endeeffekt_demping_100dB_0.4_punkt.txt';
% opts = detectImportOptions(filname4);
% T4=readtable(filname4,opts,'ReadVariableNames', false);
% Tv4=table2array(T4);
% Tv4=Tv4(:,70*30:130*30);
% Tv4=sum(Tv4);
%
% filname5='implicit_uten_endeeffekt_demping_100dB_0.4_punkt.txt';
% opts = detectImportOptions(filname5);
% T5=readtable(filname5,opts,'ReadVariableNames', false);
% Tv5=table2array(T5);
% Tv5=Tv5(:,70*30:130*30);
% Tv5=sum(Tv5);


% Timevector
% Experiment
t=(1:length(Tv4)+1000)*delta_t;
t=t(1:length(Tv4));

f=100e3; % Avrerage frequency in chirp
T=1/f; % Average period in chirp

% Simulation
S_T=30; % samples per period
t1=(1:1:150*S_T+3);
t1=t1*T/S_T;

```

```
t2=3255+k:1:150*S_T+3;
t2=t2*T/S_T;

% Bandpass filter for experiment

% Tv1b=bandpass([t,Tv1],[50e3, 150e3],1/delta_t);
% Tv1b=Tv1b(length(Tv1)+1:end);
% Tv2b=bandpass([t,Tv2],[50e3, 150e3],1/delta_t);
% Tv2b=Tv2b(length(Tv2)+1:end);
% Tv3b=bandpass([t,Tv3],[50e3, 150e3],1/delta_t);
% Tv3b=Tv3b(length(Tv3)+1:end);
Tv4b=bandpass([t,Tv4],[50e3, 150e3],1/delta_t);
Tv4b=Tv4b(length(Tv4)+1:end);
Tv5b=bandpass([t,Tv5],[50e3, 150e3],1/delta_t);
Tv5b=Tv5b(length(Tv5)+1:end);

% Extracting the reverberation for experiment
valstart=5850+1742;
a=0;
% Tv1b=Tv1b(valstart:end);
% Tv2b=Tv2b(valstart:end);
% Tv3b=Tv3b(valstart:end-a);
Tv4b=Tv4b(valstart:end-a);
Tv5b=Tv5b(valstart:end-a);


% Rectangular filter (finding start and end point at zero)
[val1,start1]=min(abs(Tv1b(1:100)));
[val2,start2]=min(abs(Tv2b(1:100)));
[val3,start3]=min(abs(Tv3b(1:100)));
[val4,start4]=min(abs(Tv4b(1:100)));
[val5,start5]=min(abs(Tv5b(1:100)));

[val1,end1]=min(abs(Tv1b(length(Tv1b)-100:end)));
[val2,end2]=min(abs(Tv2b(length(Tv2b)-100:end)));
[val3,end3]=min(abs(Tv3b(length(Tv3b)-100:end)));
[val4,end4]=min(abs(Tv4b(length(Tv4b)-100:end)));
[val5,end5]=min(abs(Tv5b(length(Tv5b)-100:end)));

Tv1b=Tv1b(start1:length(Tv1b)-end1);
Tv2b=Tv2b(start2:length(Tv2b)-end2);
```

```
Tv3b=Tv3b(start3:length(Tv3b)-end3);
Tv4b=Tv4b(start4:length(Tv4b)-end4);
Tv5b=Tv5b(start5:length(Tv5b)-end5);

%% Hamming window

Tv1b=transpose(hamming(length(Tv1b))).*Tv1b;
Tv2b=transpose(hamming(length(Tv2b))).*Tv2b;
Tv3b=transpose(hamming(length(Tv3b))).*Tv3b;
Tv4b=transpose(hamming(length(Tv4b))).*Tv4b;
Tv5b=transpose(hamming(length(Tv5b))).*Tv5b;


%% Hanning window

Tv1b=transpose(hann(length(Tv1b))).*Tv1b;
Tv2b=transpose(hann(length(Tv2b))).*Tv2b;
Tv3b=transpose(hann(length(Tv3b))).*Tv3b;
Tv4b=transpose(hann(length(Tv4b))).*Tv4b;
Tv5b=transpose(hann(length(Tv5b))).*Tv5b;

%% FFT

Fs=1/(T/30); % sampling frequency for simulation
% Fs=1/delta_t; % Sampling frequency for experiment
Sa=[Tv1b,zeros(1,2^20-length(Tv1b))]; % Zero padding
Ls = width(Sa);% Signal length
F = fft(Sa);% Calling fft() function for signal dfa
PS2 = abs(F/length(Tv1b));% Double sampling plot
PS1 = PS2(:,1:Ls/2+1);%Single sampling plot
PS1(2:end-1) = 2*PS1(2:end-1); % Dobble amplitude (just positive values)
f = Fs*(0:(Ls/2))/Ls; % Frequency vector

% Repeat for other signals
Fs2=1/(T/30);
% Fs2=1/delta_t; % Sampling frequency
Sa2=[Tv2b,zeros(1,2^20-length(Tv2b))]; % Zero padding
Ls2 = width(Sa2);% Signal length
F2 = fft(Sa2);% Calling fft() function for signal dfa
PS2_2 = abs(F2/length(Tv2b));% Double sampling plot
PS1_2 = PS2_2(:,1:Ls2/2+1);% Single sampling plot
```

```
PS1_2(2:end-1) = 2*PS1_2(2:end-1);
f2 = Fs2*(0:(Ls2/2))/Ls2;

Fs3=1/(T/30);
% Fs3=1/delta_t;
Sa3=[Tv3b,zeros(1,2^20-length(Tv3b))];
Ls3 = width(Sa3);% Signal length
F3 = fft(Sa3);% Calling fft() function for signal dfa
PS2_3 = abs(F3/length(Tv3b));% Double sampling plot
PS1_3 = PS2_3(:,1:Ls3/2+1);% Single sampling plot
PS1_3(2:end-1) = 2*PS1_3(2:end-1);
f3 = Fs3*(0:(Ls3/2))/Ls3;

% Fs4=1/(T/30);
Fs4=1/delta_t;
Sa4=[Tv4b,zeros(1,2^20-length(Tv4b))];
Ls4 = width(Sa4);% Signal length
F4 = fft(Sa4);% Calling fft() function for signal dfa
PS2_4 = abs(F4/length(Tv4b));% Double sampling plot
PS1_4 = PS2_4(:,1:Ls4/2+1);% Single sampling plot
PS1_4(2:end-1) = 2*PS1_4(2:end-1);
f4 = Fs4*(0:(Ls4/2))/Ls4;
%
% Fs5=1/(T/30);
Fs5=1/delta_t;
Sa5=[Tv5b,zeros(1,2^20-length(Tv5b))];
Ls5 = width(Sa5);% Signal length
F5 = fft(Sa5);% Calling fft() function for signal dfa
PS2_5 = abs(F5/length(Tv5b));% Double sampling plot
PS1_5 = PS2_5(:,1:Ls5/2+1);% Single sampling plot
PS1_5(2:end-1) = 2*PS1_5(2:end-1);
f5 = Fs5*(0:(Ls5/2))/Ls5;

%% Plotting frequency

hold on
% plot(f./1e3,20*log10(PS1./max(PS1(1:27000))),'linewidth',1.2)
% plot(f2./1e3,20*log10(PS1_2./max(PS1(1:27000))),'linewidth',1.2)
% plot(f3./1e3,20*log10(PS1_3./max(PS1(1:27000))),'linewidth',1.2)

% plot(f./1e3,PS1./max(PS1(1:end)),'m-','linewidth',1.2)
```

```
% plot(f2./1e3,PS1_2./max(PS1_2(1:end)),'m-','linewidth',1.2)
plot(f3./1e3,PS1_3./max(PS1_3(1:end)),'m-','linewidth',1.2)
plot(f4./1e3,PS1_4./max(PS1_4(1:27000)),'b-','linewidth',1.2)
plot(f5./1e3,PS1_5./max(PS1_5(1:27000)),'r-','linewidth',1.2)
xlim([50,150])
ylim([0,1.7])

% legend('Simulated without defect','Simulated spherical
    ↪ defect','Simulated cylindrical
    ↪ defect','FontSize',12,'location','northwest')
legend('Simulated Spherical defect','Spherical defect S1','Spherical
    ↪ defect S2','Grout S3','FontSize',12,'location','northwest')
% legend('Without defect','Spherical defect','Cylindrical
    ↪ defect','FontSize',12,'location','northeast')

xlabel('Frequency [kHz]','FontSize',12)
ylabel('Normalised amplitude','FontSize',12)

pbaspect([1.6,1,1])
saveas(gcf,'Compare spherical simulated experiment rectangular before
    ↪ pulse FFT.png')
% saveas(gcf,'Sammenligne_ekspriment_betong_samples_reproduserbarhet.png')


%% plotting time
% figure
hold on
% plot(t(1:length(Tv1))*1e3,Tv1(1,:)./max(Tv1(1,:)),'linewidth',1.2)
% plot(t(1:length(Tv2))*1e3,Tv2(1,:)./max(Tv2(1,:)),'-.','linewidth',1.2)
% plot(t(1:length(Tv3))*1e3,Tv3(1,:)./max(Tv3(1,:)),'linewidth',1.2)
% plot(t(length(Tv4))*1e3,Tv4(1,:)./max(Tv4(1,:)),'linewidth',1.2)

% t1=(valstart+start1+1:1:valstart+start1+length(Tv1b)).*delta_t;
% t2=(valstart+start2+1:1:valstart+start2+length(Tv2b)).*delta_t;
% t3=(valstart+start3+1:1:valstart+start3+length(Tv3b)).*delta_t;
t4=(valstart+start4+1:1:valstart+start4+length(Tv4b)).*delta_t;
t5=(valstart+start5+1:1:valstart+start5+length(Tv5b)).*delta_t;

t2a=t2-0.195/1481;


```

```
% plot(t2a(1:length(Tv1b))*1e3,Tv1b./max(Tv1b),'m-','linewidth',1.5)
% plot(t2a(1:length(Tv2b))*1e3,Tv2b./max(Tv2b),'m-','linewidth',1.5)
plot(t2a(1:length(Tv3b))*1e3,Tv3b./max(Tv3b),'m-','linewidth',1.5)

% plot(t1*1e3,Tv1b(1,:)./max(Tv1b(1,1:end)),'-','linewidth',1.2)
% plot(t2*1e3,Tv2b(1,:)./max(Tv2b(1,1:end)),'-','linewidth',1.2)
% plot(t3*1e3,Tv3b(1,:)./max(Tv3b(1,1:end)),'b-','linewidth',1.2)
plot(t4*1e3,Tv4b(1,:)./max(Tv4b(1,1:end)),'b-','linewidth',1.2)
plot(t5*1e3,Tv5b(1,:)./max(Tv5b(1,1:end)),'r-','linewidth',1.2)


% plot(t1(1:length(Tv1))*1e3,Tv1./max(Tv1),'linewidth',1.5)
% plot(t1(1:length(Tv2))*1e3,Tv2./max(Tv2),'-','linewidth',1.5)
% plot(t1(1:length(Tv3))*1e3,Tv3./max(Tv3),'-','linewidth',1.5)
% xlim([0.89,1.5])

% legend('Grout','Steel-Grout','Steel-Grout-Steel','FontSize',12,'location','north
% legend('Simulated without defect','Simulated spherical
    ↪ defect','Simulated cylindrical
    ↪ defect','FontSize',12,'location','northwest')
% legend('Simulated spherical defect','Spherical defect S1','Spherical
    ↪ defect S2','FontSize',12,'location','northwest')
legend('Simulated cylindrical defect','Cylindrical defect
    ↪ S1','Cylindrical defect S2','Spherical defect
    ↪ S3','FontSize',12,'location','northwest')


ylim([-1.1 1.8])
xlabel('Time [ms]','FontSize',12)
ylabel('Normalised amplitude','FontSize',12)
saveas(gcf,'Compare cylindrical simulated experiment rectangular last 500
    ↪ time.png')
% saveas(gcf,'Full different steelplates.png')
```

Appendix I

COMSOL Support

Linus Andersson

Hi Mats Johan,

I see. Yes, this difference is initiated at the start and will remain at the wavefront for the duration of the simulation. The reason it occurs is that the equations solved are slightly different.

In the time explicit model, both the pressure and the velocity are solved for. The velocity condition specifies the velocity, meaning the normal velocity at the excitation boundary will be exactly what you are applying. Meanwhile, there is no excitation condition on the pressure - it will start out from zero everywhere in the model, and then take on non-zero values in reaction to the velocity.

In the transient model, in contrast, only the pressure is solved for. The velocity condition does not explicitly apply a velocity, but rather sets the value of the normal component of the pressure gradient.

Either way, starting with all zero initial values together with a non-zero velocity at t = 0 will get you an inconsistent solution. One way to avoid this and reconcile the solutions would be to multiply your velocity excitation with a ramp function, going from 0 to 1 over for example the first cycle. In the attached versions of your models I solved for only two cycles, but at least so far the solution is now looking very similar.

Best regards, Linus

Linus Andersson
COMSOL Support

To update your email preferences, visit: www.comsol.com/preferences/

Figure I.1: COMSOL support on why the transient part of the signal is importaint

Linus Andersson

Hi Mats Johan,

I tried a run with damping included, but unfortunately this brought the instabilities back. A bit of tweaking of the filter parameters could conceivably help, but it would likely take a long time to get them right.

Luckily, for this problem size, standard implicit acoustic-structure interaction will be both faster and more stable. See the attached version of your model!

Best regards, Linus

Linus Andersson
COMSOL Support

To update your email preferences, visit: www.comsol.com/preferences/

Figure I.2: COMSOL support's answer to why the model becomes unstable using damping

Appendix J

Results and Discussion

J.1 Experimental results of grout without defects

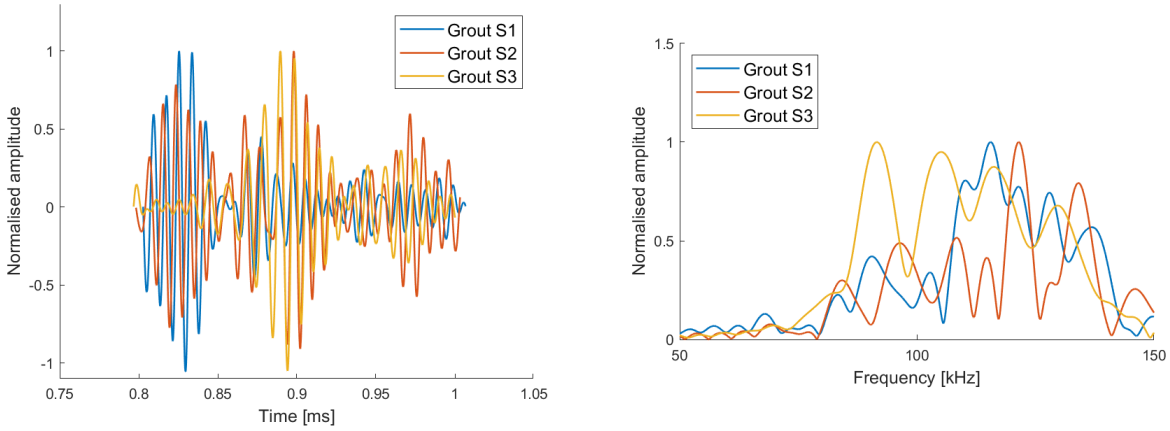

Figure J.1: Experimental results of the grout without defects with a bandpass filter of 50 to 150 kHz, the first 500 samples removed and a rectangular window in the time (left) and frequency (right) domains

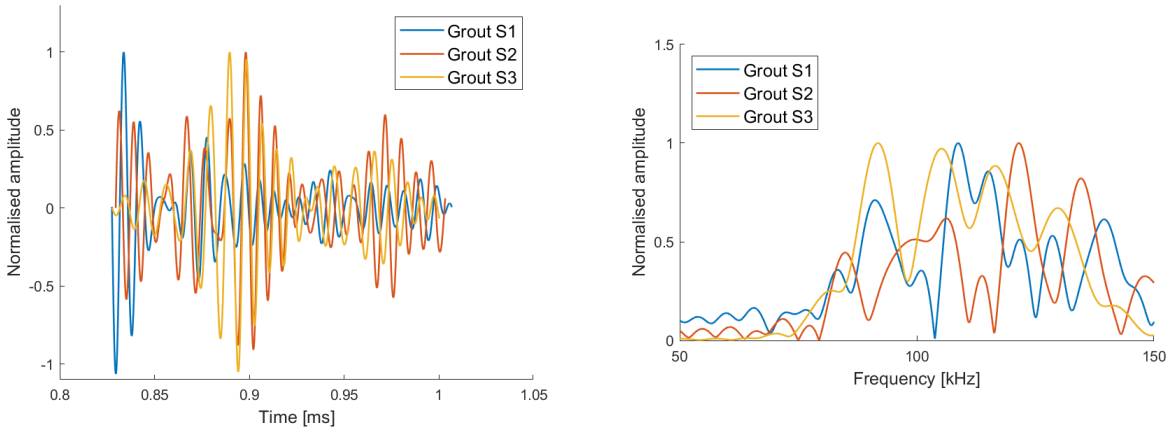

Figure J.2: Experimental results of the grout without defects, with a bandpass filter of 50 to 150 kHz, the first 700 samples removed and a rectangular window in the time (left) and frequency (right) domains.

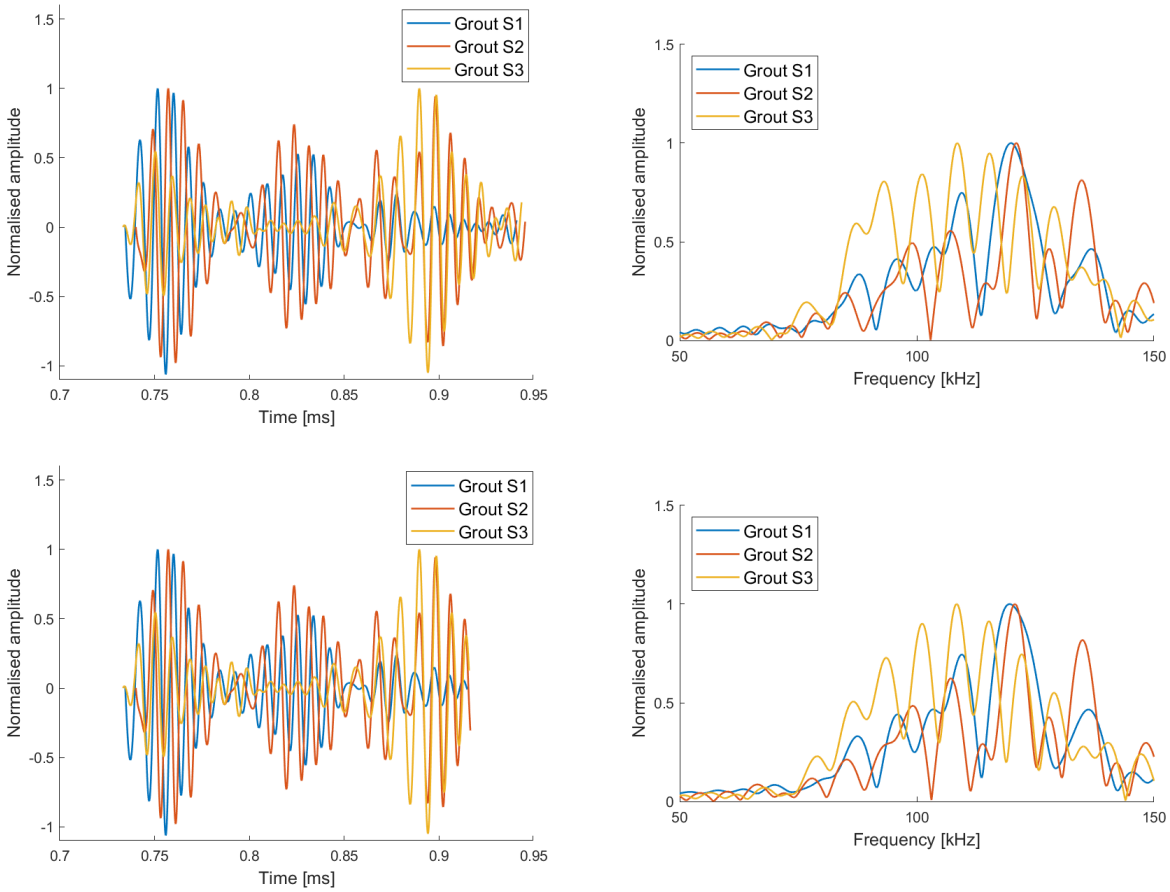

Figure J.3: Experimental results of the grout without defects, with a bandpass filter of 50 to 150 kHz and a rectangular window for the last 500 samples removed in time domain (top left) and frequency (top right) domains and last 700 samples removed in time (bottom left) and frequency (bottom right) domains

J.2 Experimental results of grout with cylindrical defects

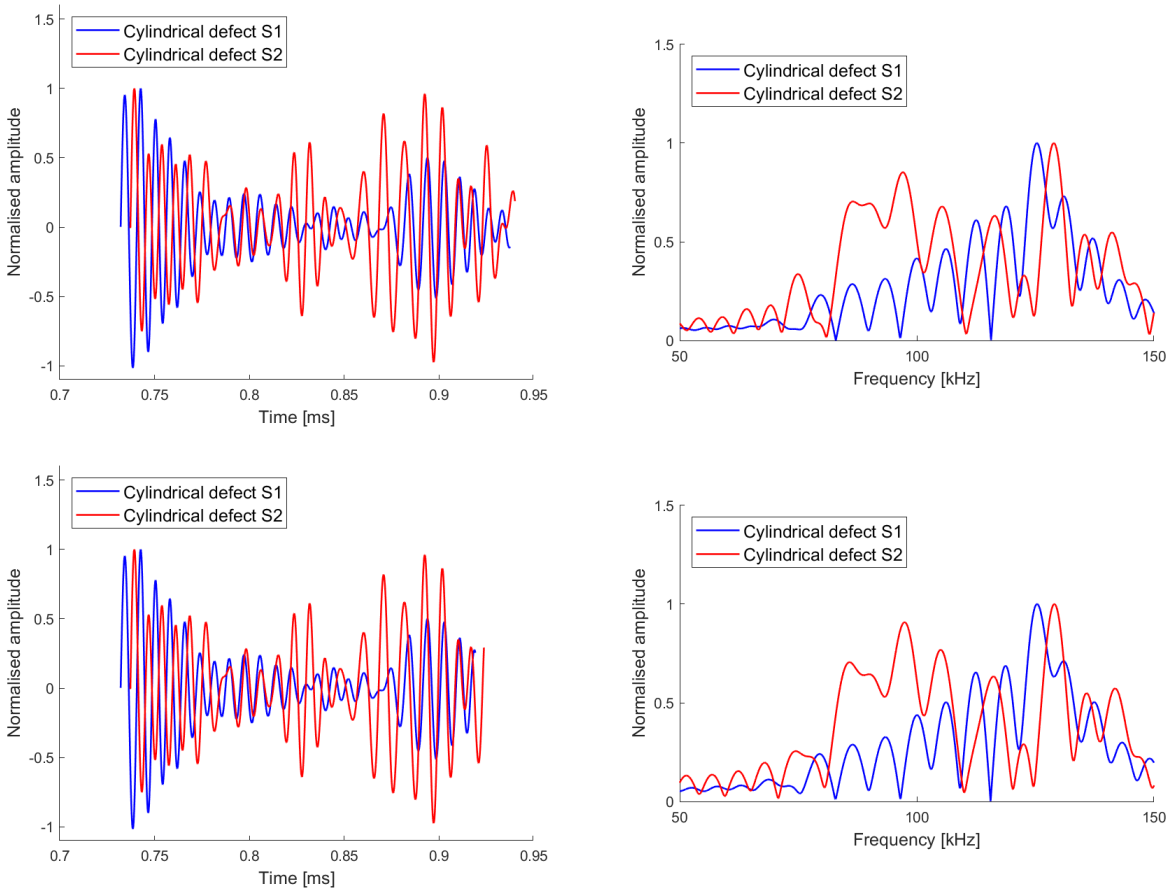

Figure J.4: Experimental results of the grout with a cylindrical defect, with a bandpass filter of 50 to 150 kHz and a rectangular window for the last 500 samples removed in time (top left) and frequency (top right) domains and last 700 samples removed in time (bottom left) and frequency (bottom right) domains

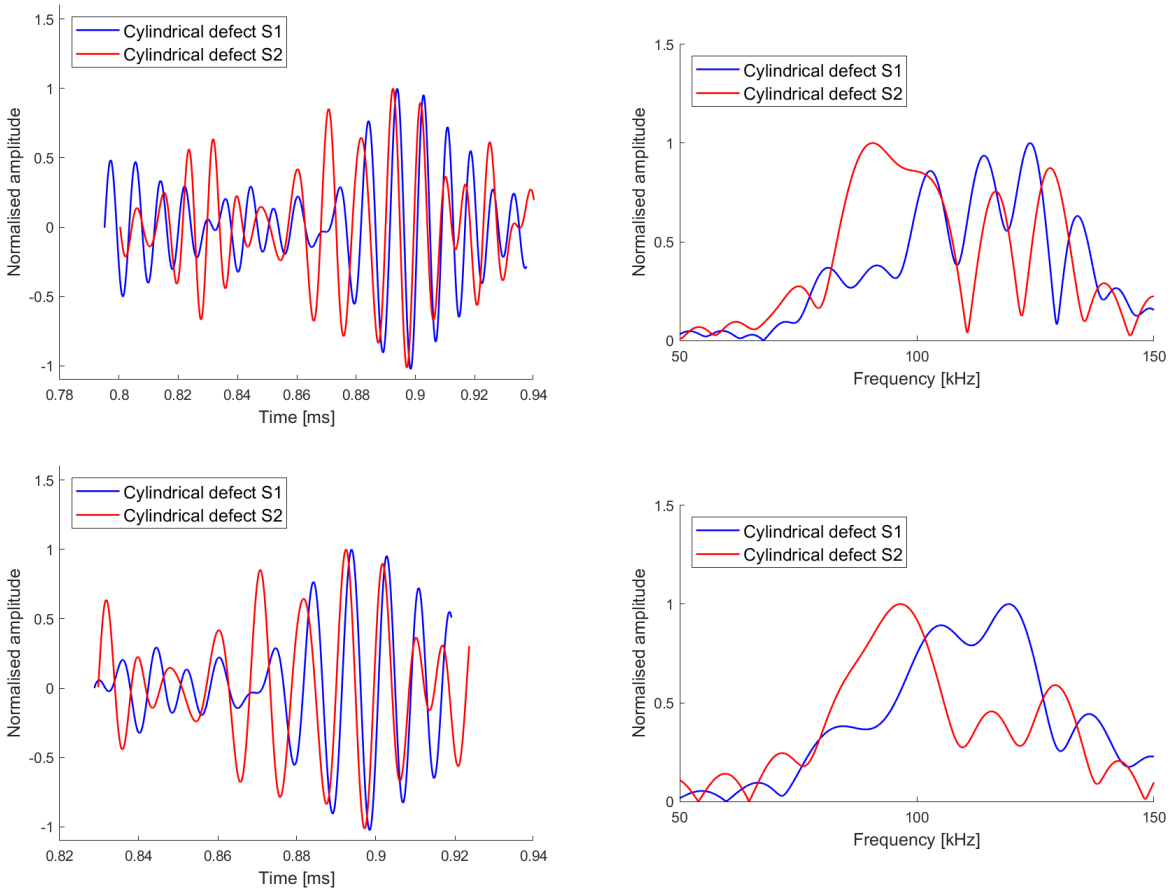

Figure J.5: Experimental results of the grout with a cylindrical defect, with a bandpass filter of 50 to 150 kHz and a rectangular window for the last and first 500 samples removed in the time (top left) and frequency (top right) domains and last and first 700 samples removed in the time (bottom left) and frequency (bottom right) domains

J.3 Experimental results of grout with spherical defects

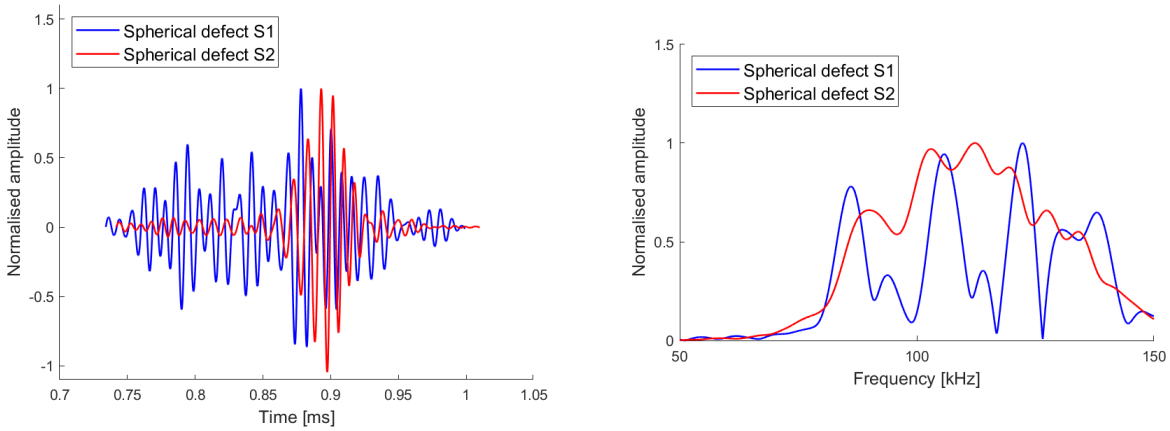

Figure J.6: Experimental results of the grout with a spherical defect, with a bandpass filter of 50 to 150 kHz and Hamming window in the time (left) and frequency (right) domains, where S1 and S2 are Samples one and two, respectively.

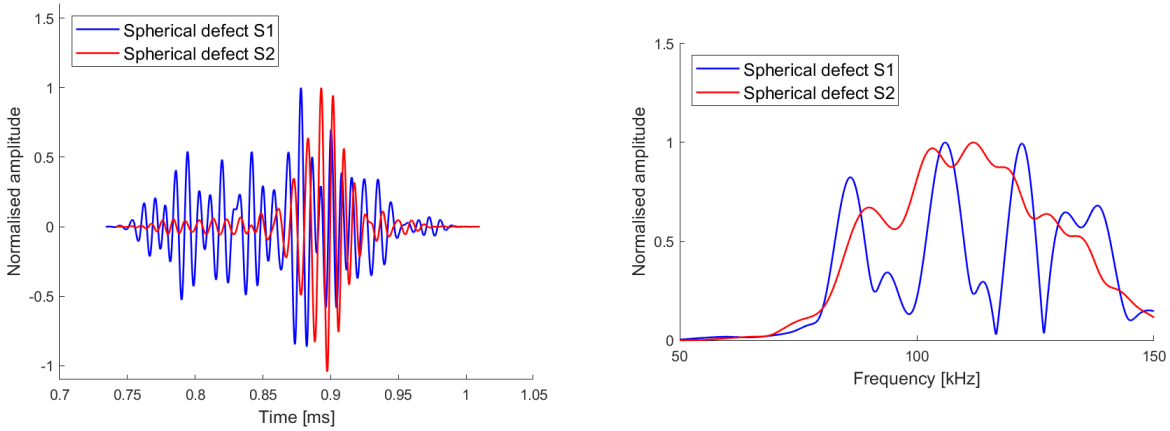

Figure J.7: Experimental results of the grout with a spherical defect, with a bandpass filter of 50 to 150 kHz and Hanning window the time (left) and frequency (right) domains, where S1 and S2 are Samples one and two, respectively.

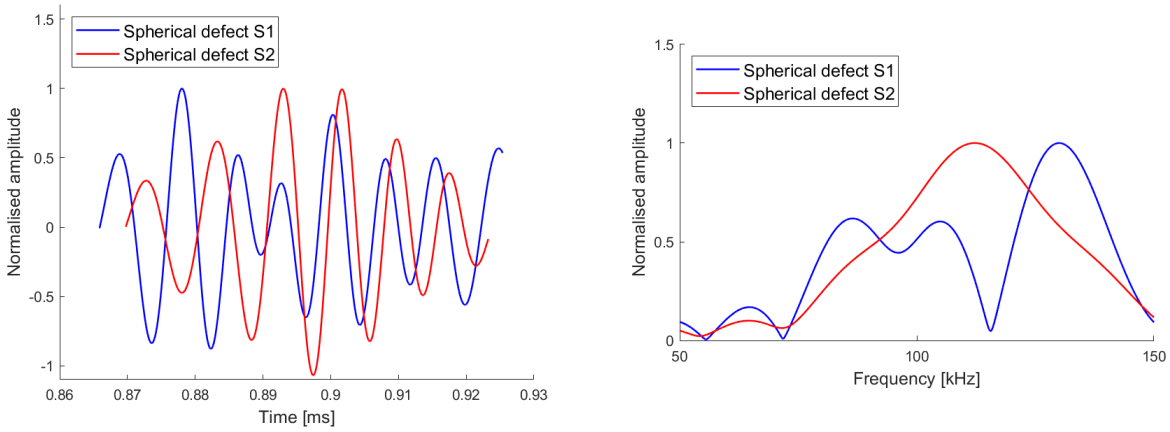

Figure J.8: Experimental results of the grout with a spherical defect, with a bandpass filter of 50 to 150 kHz and a rectangular window for the larger pulse in the reverberation in the time (left) and frequency (right) domains

J.4 Experimental part comparison

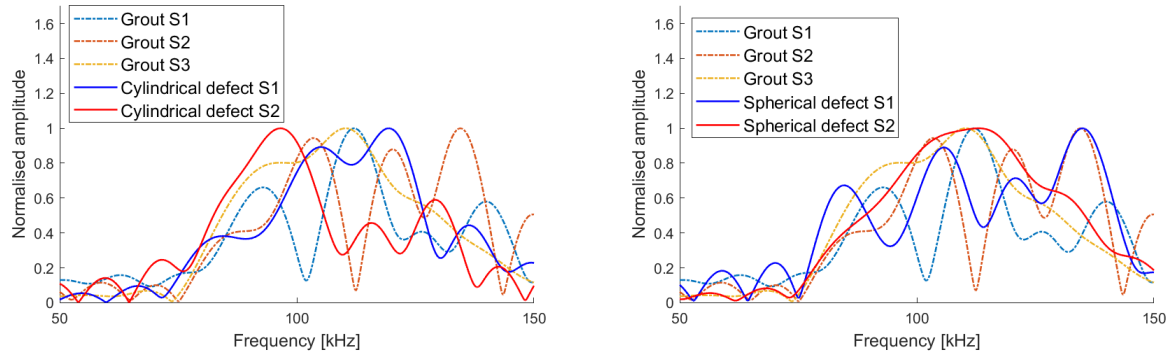

Figure J.9: Experimental results of the grout with and without defects, with a bandpass filter of 50 to 150 kHz and a rectangular window for the middle of the reverberation with cylindrical (left) and spherical (right) defects

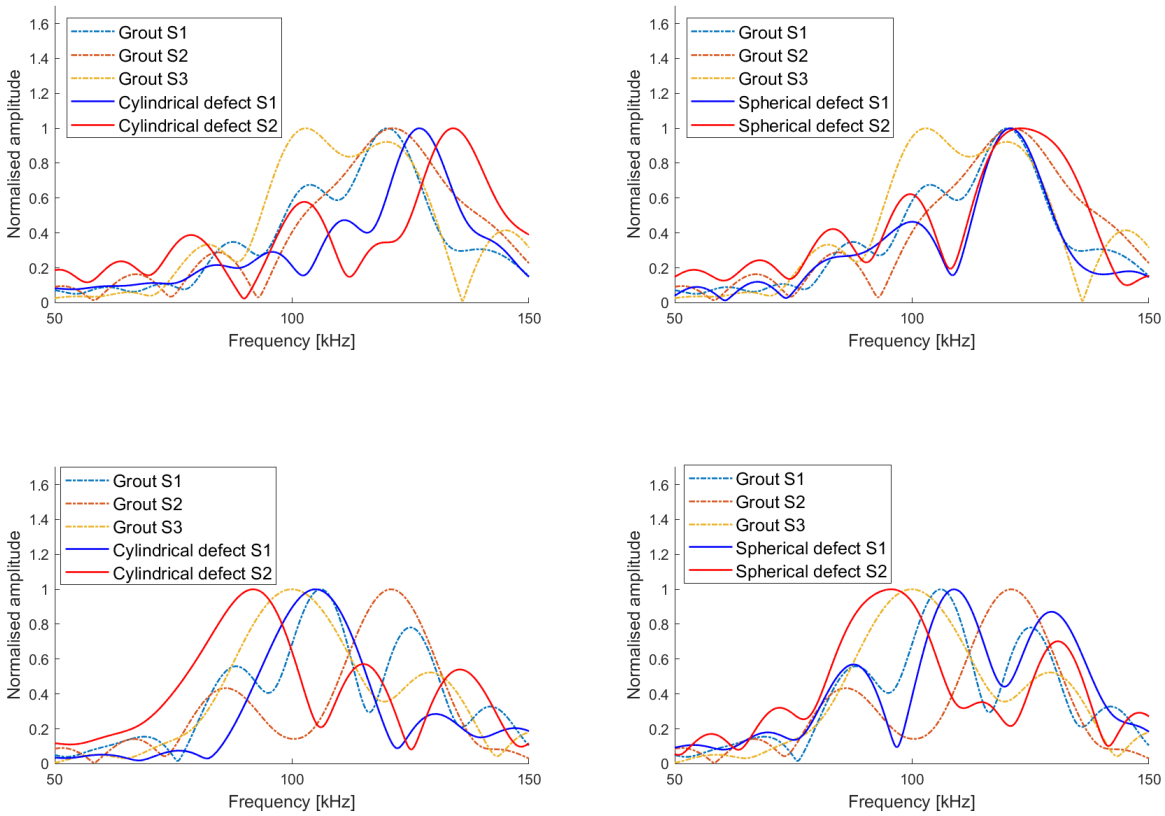

Figure J.10: Comparing experimental results of the grout with defects and grout without defects, with a bandpass filter of 50 to 150 kHz and a rectangular window for the start of reverberation (700 samples) with cylindrical defect (top left), start of reverberation (700 samples) spherical defect (top right), end of reverberation (700 samples) cylindrical defect (lower left) and end of reverberation (700 samples) spherical defect (lower right)

J.5 Simulation results

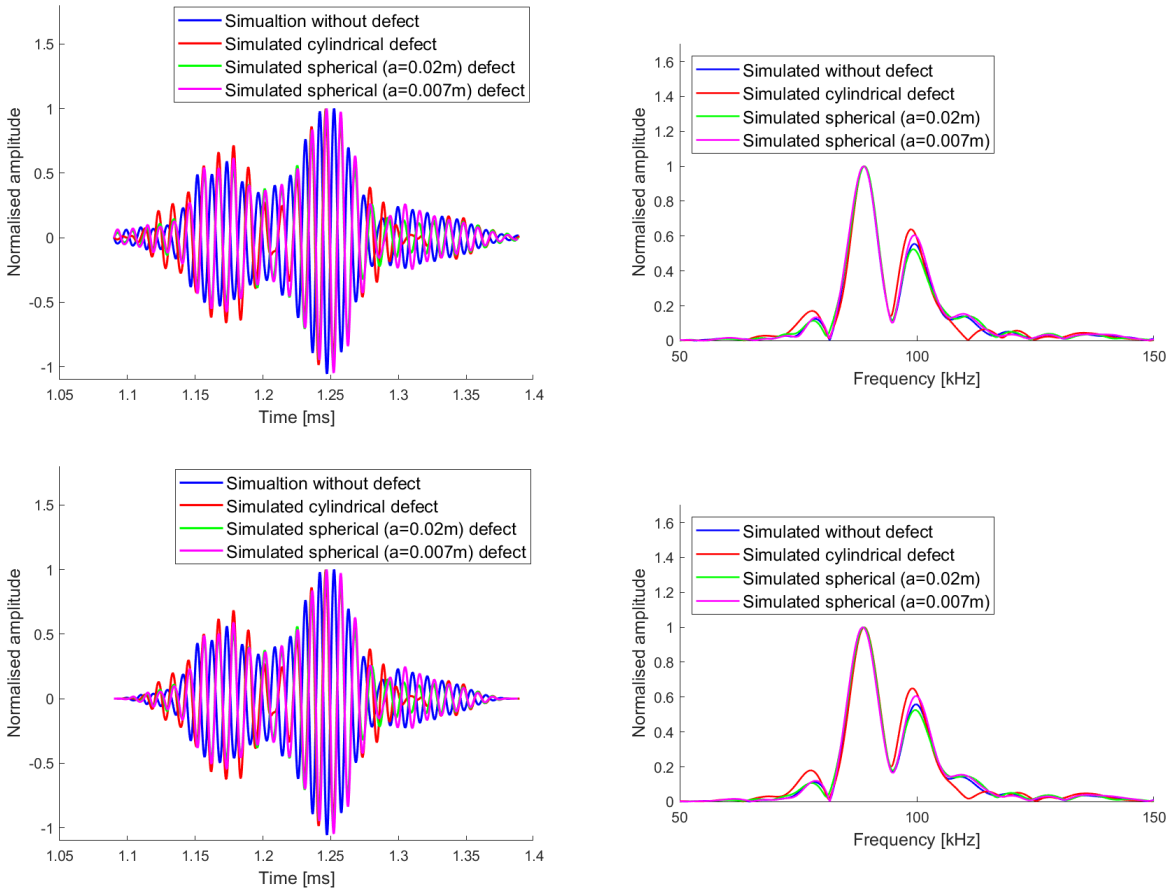

Figure J.11: Simulated results of semi-infinite steel–grout with and without defects and a Hamming (top) and Hanning (bottom) windows, showing the reverberation in the time (left) and frequency (right) domains

Appendix K

Scattering cross section for a fluid

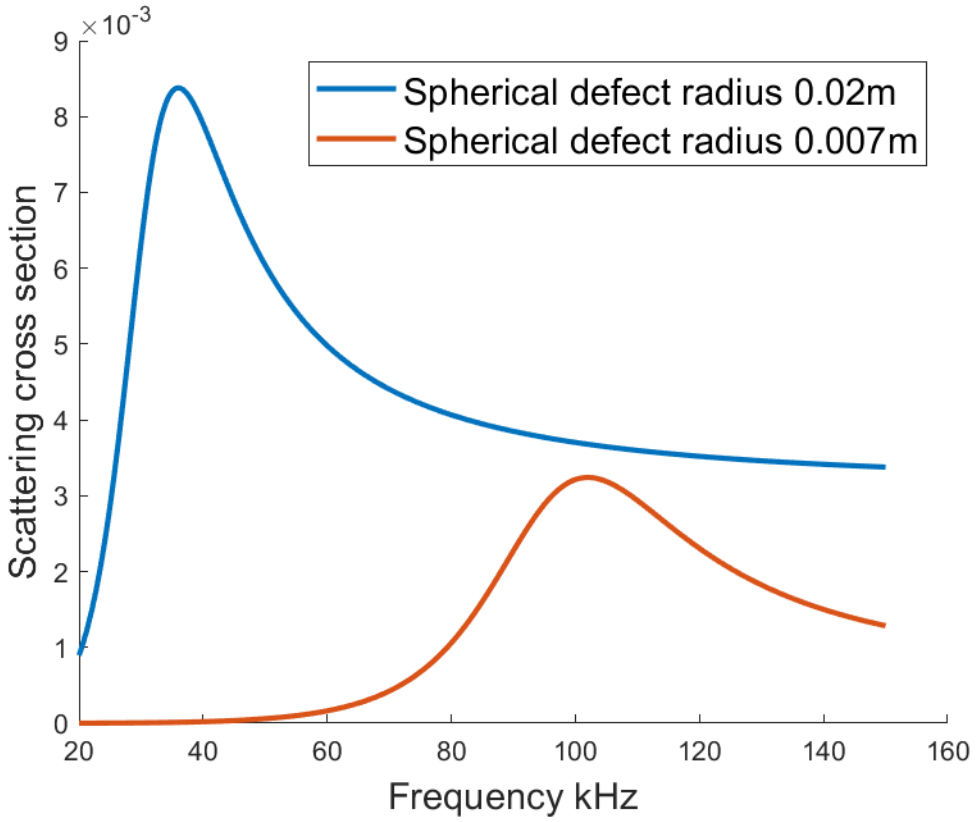

Figure K.1: Scattering cross section for gas filled spheres with different radii. The dampening coefficients are from Medwin [49]. The dampening coefficient is 0.6 for the spherical defect with 0.02m in radius, and 0.19 for the spherical defect with 0.007m in radius.

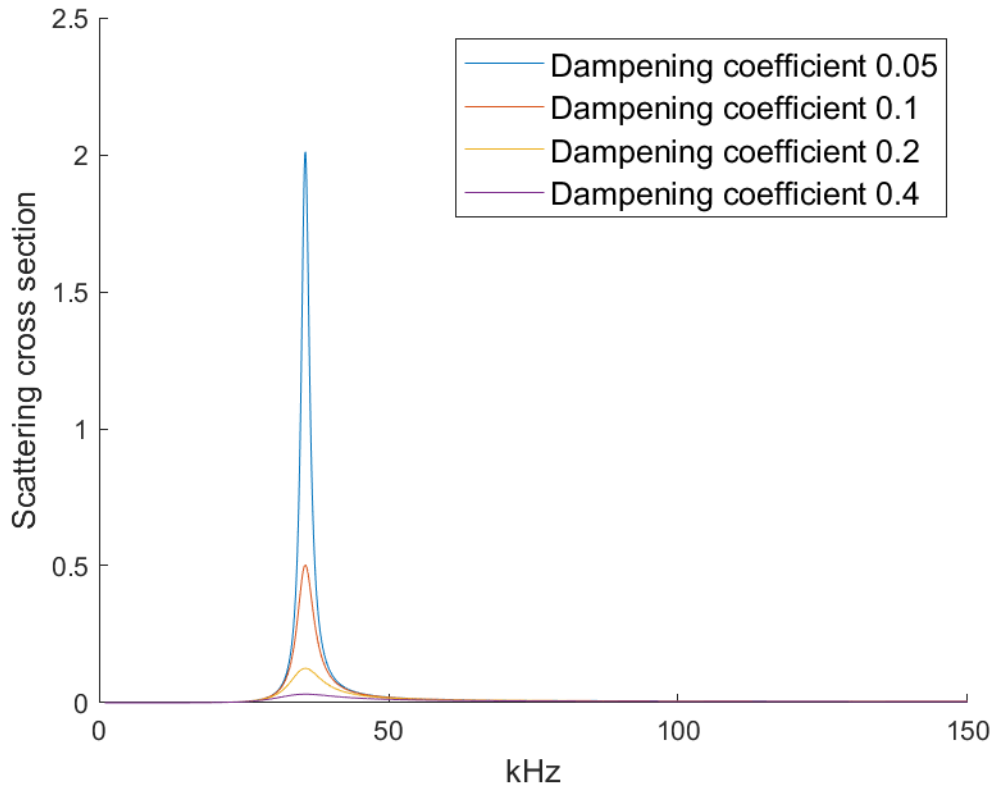

Figure K.2: Scattering cross section for gas filled spheres different dampening coefficients